2017

Compressor Performance Scaling in the Presence of Non-Uniform Flow

David Jarrod Hill
University of Windsor

Compressor Performance Scaling in the Presence of Non-Uniform Flow

by

David Jarrod Hill

A Thesis
Submitted to the Faculty of Graduate Studies
through the Department of Mechanical, Automotive & Materials Engineering
in Partial Fulfillment of the Requirements for
the Degree of Master of Applied Science at the
University of Windsor

Windsor, Ontario, Canada

2017

Compressor Performance Scaling in the Presence of Non-Uniform Flow

by

David Jarrod Hill

APPROVED BY:

_____

E. Tam
Civil & Environmental Engineering

_____

A. Sobiesiak
Mechanical, Automotive & Materials Engineering

_____

J. Defoe, Advisor
Mechanical, Automotive & Materials Engineering

May 23, 2017

Declaration of Originality

I hereby certify that I am the sole author of this thesis and that no part of this thesis has been published or submitted for publication.

I certify that, to the best of my knowledge, my thesis does not infringe upon anyone's copyright nor violate any proprietary rights and that any ideas, techniques, quotations, or any other material from the work of other people included in my thesis, published or otherwise, are fully acknowledged in accordance with the standard referencing practices. Furthermore, to the extent that I have included copyrighted material that surpasses the bounds of fair dealing within the meaning of the Canada Copyright Act, I certify that I have obtained a written permission from the copyright owner(s) to include such material(s) in my thesis and have included copies of such copyright clearances to my appendix.

I declare that this is a true copy of my thesis, including any final revisions, as approved by my thesis committee and the Graduate Studies office, and that this thesis has not been submitted for a higher degree to any other University or Institution.

Abstract

Fuselage-embedded engines in future aircraft will see increased flow distortions due to the ingestion of airframe boundary layers. This reduces the required propulsive power compared to podded engines. Inlet flow distortions mean that localized regions of flow within the fan and first stage compressor are operating at off-design conditions. It is important to weigh the benefit of increased vehicle propulsive efficiency against the resultant reduction in engine efficiency. High computational cost has limited most past research to single distortion studies. The objective of this thesis is to extract scaling laws for transonic compressor performance in the presence of various distortion patterns and intensities. The machine studied is the NASA R67 transonic compressor. Volumetric source terms are used to model rotor and stator blade rows. The modelling approach is an innovative combination of existing flow turning and loss models, combined with a compressible flow correction. This approach allows for a steady calculation to capture distortion transfer; as a result, the computational cost is reduced by two orders of magnitude. At peak efficiency, the rotor work coefficient and isentropic efficiency are matched within 1.4% of previously published experimental results. A key finding of this thesis is that, in non-uniform flow, the state-of-the-art loss model employed is unable to capture the impact of variations in local flow coefficient, limiting the analysis of local entropy generation. New insight explains the mechanism governing the interaction between a total temperature distortion and a compressor rotor. A parametric study comprising 16 inlet distortions reveals that for total temperature distortions, upstream flow redistribution and rotor diffusion factor changes are shown to scale linearly with distortion severity. Linear diffusion factor scaling does not hold true for total pressure distortions. For combined total temperature and total pressure distortions, the changes in rotor diffusion factor are predicted by the summation of the individual distortions, within 3.65%.

Acknowledgments

The work presented in this thesis is a culmination of the effort and support of those close to me. Firstly, I am grateful for the support and guidance of my supervisor, Dr. Jeff Defoe. His expertise in the field of turbomachinery, dedication to each of his students, and passion towards his craft has helped to develop me into the technical professional I am today. For that, I am thankful. Additionally, I would like to thank my committee members Dr. Andrzej Sobiesiak and Dr. Edwin Tam for both their time in reviewing my thesis and thoughtful insight on improvements.

To the past and current members of the Computational Fluid Dynamics Laboratory group, I would like to thank you for your camaraderie and assistance in helping me achieve this goal. In particular, I would like to extend my gratitude to Krishna Patel, Ravinder Gill, Kharuna Ramrukheea, Matheson West, Quentin Minaker, and Kohei Fukuda.

A final thank you is extended to my family: my parents, Dave and Sherry, and sisters Lindsay, Courtney, and Chelsea for their unconditional support and encouragement. I would not be at this point in my academic career without each and every one of you.

Contents

List of Figures

List of Tables

Nomenclature

Symbols

a speed of sound

A area

AR aspect ratio

B number of blades

c blade chord

c_p specific heat capacity of air at constant pressure

d boundary layer thickness

D diffusion factor

DC_{120} distortion characteristic

DM_Σ diffusion metric

f volumetric source term per unit mass

F volumetric source term per unit volume

FPR fan/compressor pressure ratio

g_{red} reduced rotor frequency

h enthalpy, staggered spacing in blade row

K_n Peters volumetric source term coefficient

L length

$\dot{m}$ mass flow rate

M Mach number

n_θ circumferential projection of the local blade normal vector

p pressure

P power

q dynamic pressure

r radial coordinate

R radius

s entropy

T temperature

U blade speed

v velocity

V volume

W relative velocity

$\dot{W}$ energy source per unit volume

x, y, z Cartesian coordinates

α absolute swirl angle

β relative swirl angle

γ ratio of specific heats

δ flow deviation angle

ϵ compressibility correction factor

ζ entropy-based loss coefficient

η efficiency

θ circumferential coordinate

κ local blade camber angle

λ radial flow angle

Λ re-cambering constant

μ dynamic viscosity

ν' coordinate in blade passage direction

ξ blade stagger angle

ρ density

σ blade solidity

τ' coordinate normal to blade passage direction

υ relative grid density

ϕ axial flow coefficient

ψ rotor work coefficient

ω total pressure loss coefficient

Ω fan rotational speed

Subscripts

0 domain inlet

1 rotor inlet

2 rotor outlet, stator inlet

3 stator outlet

in inlet

is isentropic

j jet

LE leading edge

max maximum

min minimum

n direction normal to streamline

p direction perpendicular to streamline

ref reference

t total/stagnation quantity

TE trailing edge

w wake

∞ freestream

Superscripts

M mass-averaged quantity

Abbreviations

BLI Boundary Layer Ingestion/Ingesting

CAD Computer-Aided Design

CFD Computational Fluid Dynamics

GGI General Grid Interface

RANS Reynolds-Averaged Navier-Stokes

SST Shear-Stress Transport

TSFC Thrust Specific Fuel Consumption

VSTM Volumetric Source Term Model

Chapter 1

Introduction

In an effort to reduce the fuel consumption and carbon emission of commercial aviation, future generation aircraft are moving towards fuselage embedded engines. These configurations, known as Boundary Layer Ingestion (BLI), require reduced propulsive power to generate the equivalent thrust of a conventional podded engine. An improvement in overall vehicle efficiency of 3-4% is expected for BLI [1], a significant improvement for the commercial aviation industry. A consequence of BLI, however, is the fan/compressor isentropic efficiency penalty associated with non-uniform inlet conditions. Of importance is to assess the benefit of overall vehicle efficiency with BLI against the reduction in engine efficiency. In particular, the way efficiency penalties scale for different distortions is not well-understood.

Fuel burn reduction was also the driving force behind the development of turbo-props in the 1960's [2]. A large propeller radius draws in a large mass flow rate of air, leading to improved propulsive efficiency. The propeller radius requires it to operate at a reduced angular velocity compared to the high pressure compressor system, meaning a gearbox is required. This gearbox shifts the propeller axis off centre from the compressor axis.

In both configurations the fan or first compressor stage must operate in non-

uniform inlet flow. It is important to quantify the impact of these distortions on isentropic efficiency. While flow redistribution mechanisms in the presence of BLI have been previously discussed, a quantitative relationship between various inlet distortions and compressor performance has not been identified for the transonic regime - this thesis serves to fill that research gap. By making use of an improved volumetric source term model (VSTM), a parametric study of varying distortion patterns and intensities is carried out.

1.1   Objective and High-Level Approach

The objective of this thesis is to identify the compressor performance scaling trends resulting from a matrix of inlet distortions. The distortions will represent those found in practical applications: BLI and turboprop engines. To study a large array of cases, computational costs are reduced by making use of a volumetric source term representation of the machine of interest. This approach allows for the use of steady computational fluid dynamics (CFD) calculations, as opposed to unsteady, as the rotor and stator domains are pitchwise-averaged representations of the actual blades. Additionally, the removal of physical blades in favour of volumetric source terms allows for a computational grid reduction of approximately two orders of magnitude.

1.2   Major Findings and Conclusions

In this thesis, key observations are made on two fronts: development of the VSTM and the transonic compressor response to non-uniform inflow.

Within the revised VSTM, a compressibility correction factor to a low-speed blade loading model is able to accurately capture the overall compressor work input. Also, a double-sided loss model successfully produces a more robust blade row efficiency characteristic. Spanwise profiles of rotor work input and isentropic effi-

ciency, and of stator loss coefficient are shown to be well-matched to bladed, single passage Reynolds-Averaged Navier-Stokes (RANS) results and previously published data for both uniform and non-uniform inflow. The loss model, however, is shown to be deficient in capturing the effect of spatial deviations from design flow coefficient for non-uniform inflow. Though the blade domain viscous losses are inaccurately modeled, the VSTM is still useful in studying upstream flow redistribution and rotor diffusion factor changes; a parameter expected to be correlated with changes in isentropic efficiency.

By employing the VSTM for a series of distortions, similarities and differences arise from a previously-studied low-speed fan case. In both BLI and turboprop total pressure distortions, the upstream mass flux and relative flow angle changes exhibit similar behaviour for both low-speed and transonic cases. However, the rotor diffusion factor changes in a transonic compressor exhibit a non-linear scaling trend which differs from the results for a low-speed fan. For a total temperature distortion, the governing mechanisms for upstream flow redistribution are identified - an observation which has not been made in any previous literature, to the author's knowledge. The impact of the distortion exhibits a linear scaling trend for all pertinent flow characteristics. However, the total temperature distortion is shown to have a reduced impact on flow redistribution compared to total pressure distortion. In a combined turboprop distortion of total temperature and total pressure, the resultant flow redistribution and diffusion factor changes are shown to be consistent with the summation of the individual distortions. Finally, a method for producing a revised parallel force model is proposed. This approach would allow more a more comprehensive analysis of flow characteristics within the blade domain in the presence of non-uniform inflow.

1.3   Thesis Outline

Relevant past literature is reviewed in Chapter 2, relating to both distorted flow/rotor interaction mechanisms and the development of volumetric source term models. Next, the development of the volumetric source term used in this work is presented in Chapter 3. Following this, the resultant volumetric source term model and its assessment in uniform and non-uniform inflow is given in Chapter 4. In Chapter 5the key results from the parametric study of distortions are presented. Lastly, conclusions drawn from this work and future plans are detailed in Chapter 6.

Chapter 2

Literature Review

This chapter establishes the state of the art with regard to the phenomena of interest, pertinent modeling methodology, and identifies the research gaps this work seeks to fill.

2.1 Non-Uniform Inlet Flow Patterns

In this work, two distinct cases of non-uniform inflow are studied: boundary layer ingestion and turboprop compressor ingestion of propeller outflow.

2.1.1 Boundary Layer Ingestion

To reduce the propulsive power required in commercial aircraft, boundary layer ingestion (BLI) configurations can be utilized. The potential benefit of boundary layer ingestion has been known since the early work by Smith and Roberts [3]. By placing the engine in such a configuration that the engine ingests the boundary layer flow over the fuselage of the aircraft, the aircraft wake momentum deficit can be reduced, thus minimizing vehicle drag. This configuration and benefit is shown in Figure 2-1 [1]. In the podded engine configuration, the uniform flow into the engine inlet is at

freestream velocity, v_∞ and exits the engine at a velocity, v_j. In the simplified BLI configuration, air enters the engine with a reduced average wake velocity, v_w and exits at freestream velocity, v_∞. In both configurations, the momentum balance is equal, however the engine in the BLI case is tasked with adding momentum to a slower moving fluid. The power required to accelerate this slower moving flow is less than the for the uniform, freestream flow. This can also be shown through a comparison of the propulsive power [1],

$$P_{podded} = \frac{\dot{m}}{2} \left(v_j^2 - v_\infty^2 \right), \tag{2.1}$$

$$P_{BLI} = \frac{\dot{m}}{2} \left(v_\infty^2 - v_w^2 \right), \tag{2.2}$$

where the power, P, is a function of the difference between engine exit velocity and engine inlet velocity. While $(v_j - v_\infty)$ is equal to $(v_\infty - v_w)$, the higher velocity of v_j yields the following inequality,

$$\left(v_j^2 - v_\infty^2 \right) > \left(v_\infty^2 - v_w^2 \right). \tag{2.3}$$

Thus, the BLI configuration is able to produce the same thrust as the podded engine, at a reduced propulsive power. Using BLI, Plas et al. were able to to computationally achieve an overall aircraft efficiency benefit of 3-4% [1]. However, this is specific to the machine of interest in that work. The benefit of BLI must be weighed against the drawback, reduced engine isentropic efficiency as it operates in distorted inflow. One aim of this thesis is to study various BLI distortions with varying intensity and boundary layer thickness. Of interest, is the scaling of isentropic compressor efficiency between the various distortions studied.
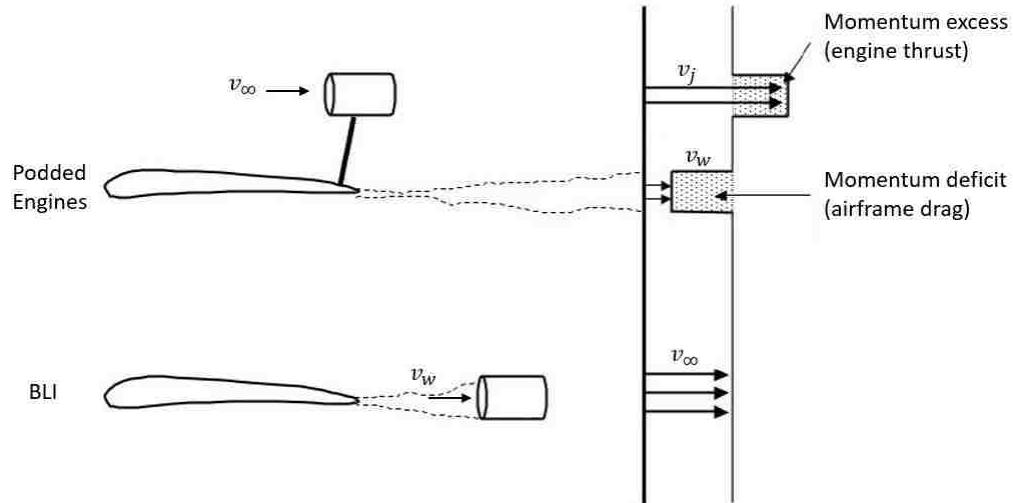
Figure 2-1: BLI and traditional podded engine configurations, the benefit of BLI stems from the reduced propulsive power required to balance the momentum deficit created by the airframe wake. Adapted from Plas et al. [1].

2.1.2 Turboprop Engine, Propeller Work Profile

Since the Vickers Viscount made history as the first commercial turboprop airliner [2], turboprop engines have been widely used as an efficient engine for powering short range, low airspeed commercial aviation. The appeal in the turboprop engine stems from the cruise thrust specific fuel consumption (TSFC), the rate of fuel burn per unit thrust, of which the turboprop engine is the most efficient style of engine available today [4]. Turboprops make use of a propeller, which is an unducted fan with an ultra high bypass ratio. The large propeller radius allows the engine to produce thrust at a larger mass flow rate and smaller velocity change compared to turbojet or even turbofan engines, leading to its reduced cruise fuel consumption. Due to this large propeller radius, the propeller must operate at a reduced rotational speed than the high pressure compressor shaft. This is done to avoid supersonic tip relative flows which lead to severe flow separation and drastic reductions in propeller isentropic efficiency. To achieve this reduced propeller speed, a gearbox is employed. A typical turboprop configuration is shown in Figure 2-2 [5]. The physical presence of the

gearbox results in offset rotational axes for the propeller and compressor. Due to this offset, and in combination with the propeller outlet radial work profile, there is a non-uniform flow profile ingested in to the compressor. This thesis serves to study various propeller offsets as well as various propeller work intensities, with the intent of observing the first stage compressor isentropic efficiency scaling between distortions.
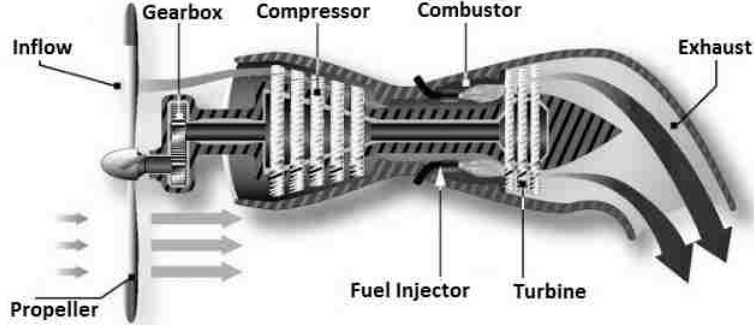
Figure 2-2: Turboprop engine configuration, showing the propeller and compressor shaft offset [5].

2.2   Distortion Mechanisms in Non-Uniform Flow

Several studies observing the flow mechanisms present in BLI distortions have been carried out [6, 7, 8, 9]. In particular, a study performed by Gunn and Hall [10] was able to capture key distortion flow characteristics shared by both low-speed and transonic fans. For both, they tested a total pressure distortion representative of a BLI case, shown in Figure 2-3. The total pressure distortion is manifested through a non-uniform velocity profile. The axial velocity itself can be expressed as a normalized flow coefficient

$$\phi = \frac{v_x}{U_{mid}}, \tag{2.4}$$

where U_{mid} is the blade speed at midspan. As the flow moves within one casing diameter upstream of the rotor, the flow is no longer decoupled from the fan. A

8

typical fan or compressor work characteristic is shown in Figure 2-4. This compressor map demonstrates how the rotor imparts more work to slower moving fluid (lower ϕ). The rotor work is represented by the work coefficient

$$\psi = \frac{\Delta h_t}{U^2},\tag{2.5}$$

where Δh_t is the rise in total enthalpy across a blade row and U is the blade speed at some specified radius. For this reason, regions of lower axial velocity flow are sucked harder in to the compressor. The result is an axial velocity increase and static pressure reduction in upstream regions of slower-moving fluid. This flow feature is illustrated in Figure 2-5, where both circumferential and radial flow redistribution arises from the static pressure distortion. The non-uniform work profile of the compressor works to attenuate the upstream axial velocity distortion, and thus the leading edge incidence angle distortion as well.
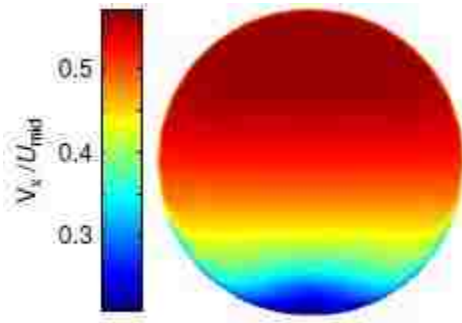
Figure 2-3: CFD fan inlet profile tested by Gunn and Hall, representative of a BLI engine. [10]
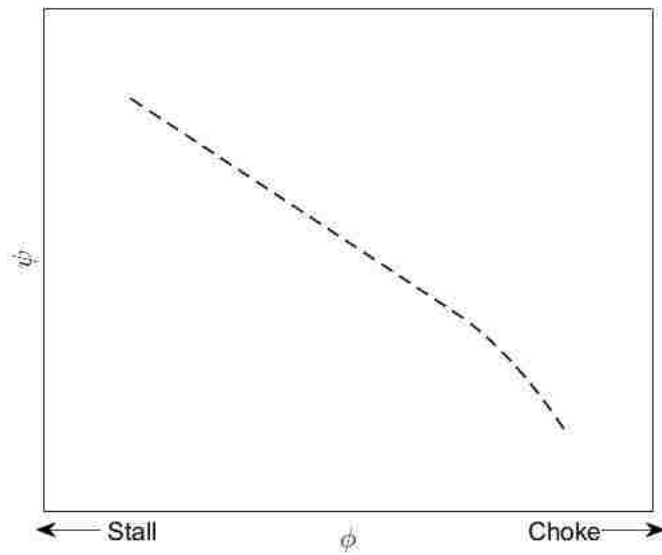
Figure 2-4: Typical compressor work characteristic, work coefficient vs flow coefficient.
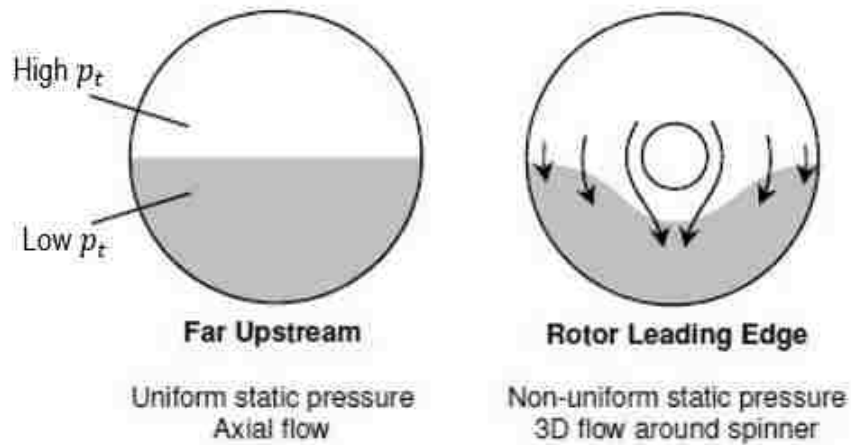
Figure 2-5: Flow redistribution upstream of the rotor, due to a non-axisymmetric rotor work profile. Adapted from Gunn and Hall [10].

Within the rotor blade passage, the flow redistribution behaviour is limited, as the physical blades block circumferential flow redistribution over length-scales greater than a single blade pitch [10]. Redistribution in this region is purely radial, again moving from regions of high flow coefficient to low coefficient. Following the rotor blade, the further attenuated distortion is transferred to the stator. The flow in the

10

stator is consistent with that of the rotor: flow redistribution is primarily observed in the radial direction due to the presence of blades. In both the rotor and stator blades, the main source of losses, compared to the uniform inflow case, stem from the change in local incidence angle and mass flux redistribution. Finally, qualitative similarities between the low-speed and transonic cases were observed in the fan response to distorted flow [10].

A study performed by Fidalgo, Hall, and Colin [11] observed a transonic-compressor response to a 120° total pressure distortion, with a DC_{120} of 83%. The distortion descriptor, DC_{120}, is [12]

$$DC_{120} = \frac{(\overline{p_t}^M - p_{t,min})}{\overline{q}^M},$$

(2.6)

where $\overline{p_t}^M$ and $\overline{q}^M$ are the mass-weighted average total pressure and dynamic pressure across the entire inlet face, and $p_{t,min}$ is the lowest total pressure averaged over any 120° sector. The case setup is illustrated in Figure 2-6, where the distortion is imposed 10 midspan rotor axial chords upstream of the rotor inlet.
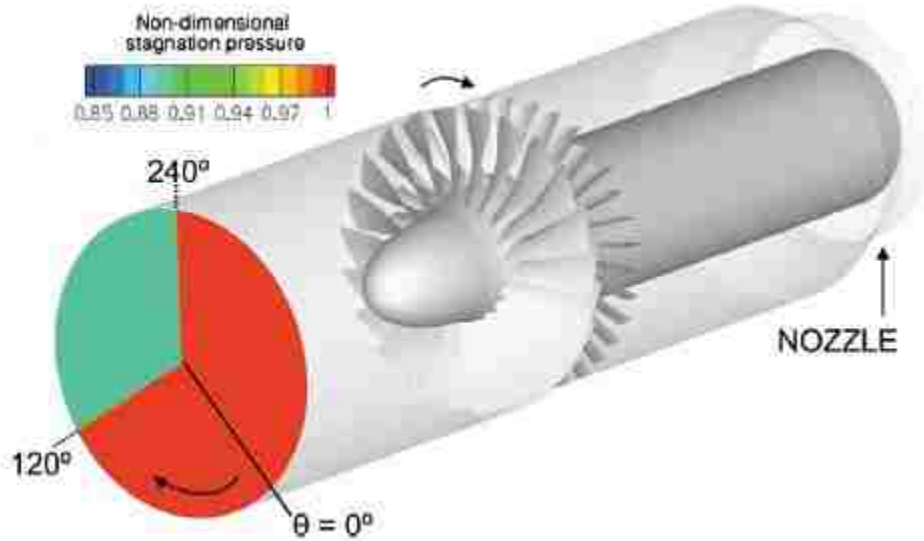
Figure 2-6: Test case setup performed by Fidalgo et al.: a 120° total pressure deficit far upstream. From [11].

Consistent with previous literature, the upstream flow redistribution, due to non-uniform circumferential rotor work, is the mechanism that attenuates the incidence angle distortion entering the compressor. Figure 2-7 shows the time-averaged absolute whirl and radial angles just upstream of the rotor. As a result of non-axisymmetric rotor work, flow has migrated towards the low static pressure region, creating regions of co-swirl (circumferential flow in the direction of blade rotation) and counter-swirl (circumferential flow swirl in the opposite direction of blade rotation). As well, in this low hub-to-tip radius ratio machine, the flow traverses across the spinner, creating a region of positive radial angle change. The result for this distortion, compared to a clean flow case, is a rotor isentropic efficiency penalty of 1.5%.
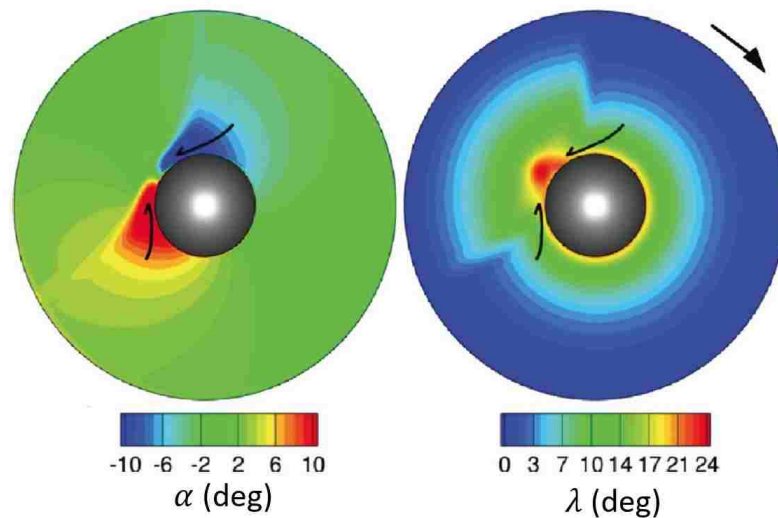
Figure 2-7: Absolute swirl angle (left) and radial flow angle (right), upstream of the rotor. Adapted from Fidalgo et al. [11].

2.3 Scaling of Diffusion Changes in a Low-Speed Fan

Each of the studies previously discussed identified the flow mechanics present in non-uniform inflow to a fan or compressor, but each considered a single inlet distortion.

A study performed by Defoe and Hall [13] observed the behaviour of a low-speed fan across an array of distortion patterns. Part of the work in this thesis serves to complement that work as a comparison between low-speed and transonic fans in distorted flow. Through the use of a volumetric source term model, the authors were able to test a matrix of rectilinearly stratified (BLI) and radially stratified (turboprop) distortions. The study was done on an inviscid fan model, meaning diffusion factor changes were used to assess the performance of the rotor. Diffusion factor is a metric developed from two-dimensional boundary-layer theory, such that an increase in flow deceleration is proportional to an increase in flow losses [14]. The changes in diffusion factor were proven to be highly dependent on the rotor leading edge incidence angle changes relative to uniform inflow.

For both vertically stratified (BLI) and radially stratified (turboprop) cases, it was shown that varying the distortion intensity of a stagnation quantity results in a change in diffusion metric that is nearly linear. The diffusion metric is an overall metric for a blade row based on the diffusion factor. This means that a more severe distortion can be represented by a combination of less-severe distortions. An example of this is shown in Figure 2-8, where the results from a vertically stratified total pressure distortion is shown on the left, and total temperature on the right. The linear scaling for these cases were found to be accurate within 3% to 16% [13]. Additionally, the combination of a total temperature and total pressure distortion was shown to be closely equivalent to the summation of the individual distortions. In the other distortions studied (boundary layer thickness and propeller offset distance), the effects of diffusion factor were shown to be highly non-linear.
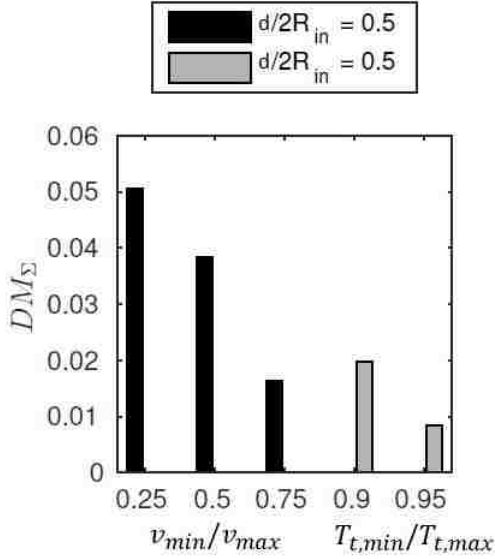
Figure 2-8: Near-linear diffusion metric scaling for vertically stratified, varying-intensity distortions - total pressure left, total temperature right [13].

The work in this thesis is studied on a transonic compressor including viscous effects. The overall flow mechanisms in the transonic compressor are expected to qualitatively match the low-speed fan results, based on the work by Gunn and Hall [10]. Observations from the results of Defoe and Hall dictate a few minor changes to the distortions that are studied in this work. Vertically stratified total temperature distortions are not considered, as this is not physically consistent with BLI. As well, radial swirl distortions will be eliminated, as the results were seen to be highly non-linear. This distortion matrix is later discussed in this thesis.

2.4 Volumetric Source Term Representation of Blade Rows

To study the scaling effects of a matrix of distortions, the use of traditional full annulus unsteady Reynolds-averaged Navier-Stokes (URANS) would require exorbitant computational resources. A full annulus, bladed, computational grid can be in excess

of 100 million cells, and require 20-30 rotor revolutions to obtain a converged solution [11, 10]. A single calculation of this nature can take in excess of two months. Rather, in this work, a volumetric source term model representation of the rotor and stator blade rows is employed. A VSTM replaces physical blades in a computational domain with a volumetric source term field, as shown in Figure 2-9. The volumetric source terms are used to create the same circumferentially-averaged flow turning, total enthalpy rise, and viscous losses as the physical blade rows. The volumetric source term model is a circumferentially-averaged representation of the blade rows, meaning individual blade wakes and blade-to-blade flow features are not captured. Volumetric source term models have been shown to accurately capture unsteady flow effects using a steady calculation [15, 1, 16, 13, 17]. This is possible through the assumption that the flow is quasi-axisymmetric, meaning that the flow is dependent on local flow conditions but, not on circumferential gradients [18]. This assumption is dependent on two conditions, the flow non-uniformity must have a characteristic length scale significantly larger than a single blade pitch, and a reduced rotor frequency, $g_{red} \ll 1$ [13]. The reduced rotor frequency is given by

$$g_{red} = \frac{c_x/V_x}{2\pi/\Omega} \approx \frac{cos\xi(1 - R_{hub}/R_{tip})}{2\pi\phi AR}, \tag{2.7}$$

where c_x is the axial chord, Ω is the rotational speed, ξ is the blade stagger angle, and AR is the blade aspect ratio ($= c_x/(R_{tip} - R_{hub})$). R_{hub} and R_{tip} are the radii of the hub and tip of the blade row, respectively.
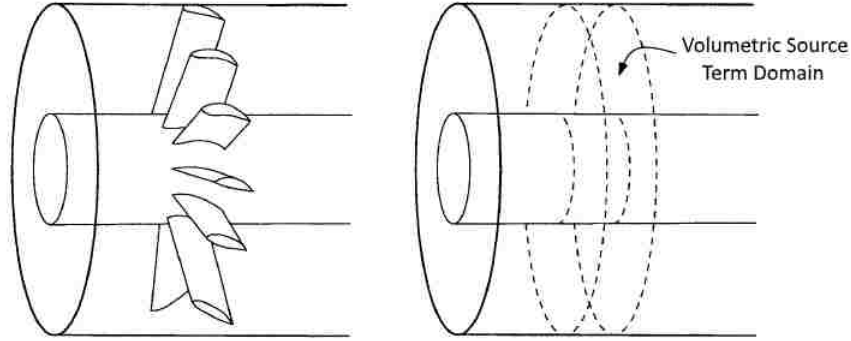
Figure 2-9: Volumetric source term representation of a blade row. Adapted from [16].

2.4.1 Previous Volumetric Source Term Model Usage

The volumetric source term methodology (otherwise known as a body forces) was first introduced by Marble [19], replacing the physical blade row by an infinite number of infinitely-thin blades. The volumetric source terms themselves can then be broken down in to a normal force, f_n, and parallel force, f_p. The normal force acts perpendicular to the relative streamline, acting to reduce the deviation of the flow from the blade camber surface. The parallel force acts against the streamwise direction and generates viscous losses in the flow. These two forces are illustrated in Figure 2-10.

In studying short-wavelength stall inception and distortion transfer in multi-stage compressors, Gong was able to expand upon Marble's VSTM [17]. Gong's model was different from traditional actuator disk methods in that the volumetric source term source terms are distributed axially and radially. In doing so, the volumetric source term is able to respond to local flow properties. The Euler equation used to describe this volumetric source term implementation is:
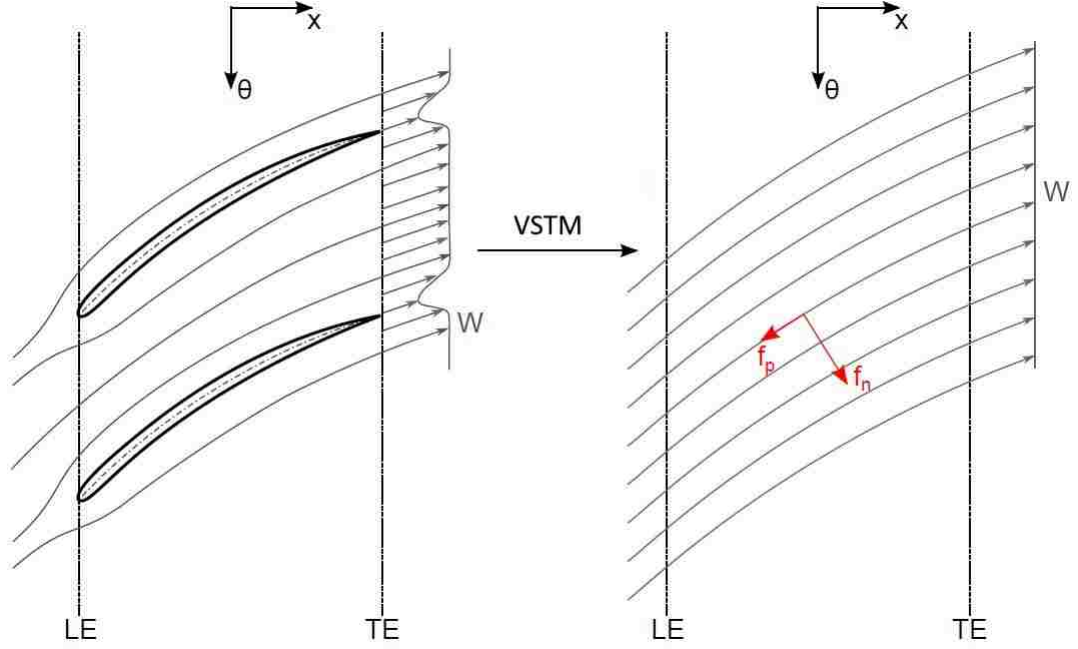
Figure 2-10: Volumetric source terms; normal turning force and parallel viscous force [15].

$$
\frac{\partial}{\partial t}
\begin{bmatrix}
r\rho \\
r\rho V_x \\
r\rho V_r \\
r\rho V_\theta \\
r_\rho e_t
\end{bmatrix}
=
\frac{\partial}{\partial x}
\begin{bmatrix}
r\rho V_x \\
r\rho V_x^2 + r\rho \\
r\rho V_x V_r \\
r\rho V_x V_\theta \\
rV_x(\rho e_t + p)
\end{bmatrix}
+
\frac{\partial}{\partial r}
\begin{bmatrix}
r\rho V_r \\
r\rho V_r V_x \\
r\rho V_r^2 + rp \\
r\rho V_r V_\theta \\
rV_r(\rho e_t + p)
\end{bmatrix}
$$

$$
+
\frac{\partial}{\partial \theta}
\begin{bmatrix}
\rho V_\theta \\
\rho V_\theta V_x \\
\rho V_\theta V_r \\
\rho V_\theta^2 + p \\
V_\theta(\rho e_t + p)
\end{bmatrix}
=
\begin{bmatrix}
0 \\
r F_x \\
\rho V_\theta^2 + p + r F_r \\
-\rho V_r V_\theta + r F_\theta \\
r\left(\vec{F} \cdot \vec{V} + \dot{Q}\right)
\end{bmatrix},
\qquad (2.8)
$$

where the momentum source per unit volume, $\vec{F}$, and momentum source per unit mass, f, are related through the local density,

17

$$\vec{F} = \begin{bmatrix} F_x \\ F_\theta \\ F_r \end{bmatrix} = \rho \begin{bmatrix} f_x \\ f_\theta \\ f_r \end{bmatrix}, \tag{2.9}$$

and the volumetric energy source term is expressed,

$$\dot{W} = \rho \vec{f} \cdot \vec{V} + \dot{Q}. \tag{2.10}$$

If the flow is considered to be adiabatic,

$$\dot{W} = \rho f_\theta \Omega r, \tag{2.11}$$

where the rate of work added to the flow at each spatial location is a product of the circumferential component of the volumetric source term, ρf_θ, and the circumferential blade velocity, Ωr. At each spatial location within a blade row, the rate of total enthalpy rise per unit volume is given by Equation 2.11.

2.4.2   Peters Volumetric Source Term Model

Based on an adaptation from Gong's volumetric source term model, Peters developed a volumetric source term model to investigate fan inlet and nacelle design parameters for low pressure ratio fans with increased fan and inlet coupling [15]. Peters model was modified from Gongs to include a radial component in the normal force, accounting for blade lean and radial streamline shifts due to area contractions. The normal force used by Peters can be decomposed in to two components, a blade loading normal force, $\vec{f_{n\nabla p}}$ and a blade loading response to local changes in deviation, $\vec{f_{n\delta}}$. The normal force magnitude is resolved to be,

$$f_n = f_{n\nabla p} + f_{n\delta} = \frac{1}{\rho} \frac{\partial p}{\partial x} \frac{sin\kappa}{cos^2\kappa} + \frac{K_n(x,r)}{h} W^2 \frac{1}{2} sin(2\delta), \tag{2.12}$$

18

where $\frac{\partial p}{\partial x}$ is the local axial pressure gradient, κ is the local blade metal angle, K_n is the blade loading coefficient, W is the local relative velocity, δ is the local deviation angle, and h is the staggered blade spacing,

$$h = \frac{2\pi r \sqrt{\sigma} cos\kappa}{B}. \tag{2.13}$$

Here, B is the number of blades and σ is the blade solidity,

$$\sigma = \frac{c}{s}, \tag{2.14}$$

where c is the blade chord length and s is the blade pitch. Given the magnitude of local normal force, the coordinate transformation about the blade metal angle and blade lean, is calculated,

$$\vec{f_{n\prime}} = \begin{bmatrix} f_{n\prime,\kappa} \\ f_{n\prime,\nu\prime} \\ f_{n\prime,\tau\prime} \end{bmatrix} = \frac{K_n\left(x,r,\delta,M_{rel}\right) W_{\nu\prime} W_{\tau\prime}}{h} \frac{1}{\left|\vec{W}\right|} \begin{bmatrix} 0 \\ W_{\tau\prime} \\ -W_{\nu\prime} \end{bmatrix} + f_{n\prime_{\nabla p}}, \tag{2.15}$$

where coordinates $\nu\prime$ and $\tau\prime$ are parallel and normal to the local camber surface, to account for radial flows. To calculate the volumetric source term coefficient K_n, the pressure difference across blade suction and pressure surfaces is calculated normal to the local camber line from single passage RANS calculations. Reworking Equation 2.12, K_n is solved for locally as,

$$K_n\left(x,r,\delta,M_{rel}\right) = \frac{f_{n_\delta} h}{W^2 \frac{1}{2} sin(2\delta)}. \tag{2.16}$$

There is a discontinuity where the local deviation angle is zero. In Peters work, at no location is the local deviation is zero. In the case where this does exist, such as in the work done by Brand [16], an offset constant, K_{off}, is implemented ,

$$K_n\left(x, r, \delta, M_{rel}\right) = \frac{f_{n_\delta} h}{W^2 \frac{1}{2} sin(2\delta + K_{off})}. \tag{2.17}$$

To avoid a change in the blade loading force, the offset constant must also be included in Equation 2.12,

$$f_n = f_{n\nabla p} + f_{n\delta} = \frac{1}{\rho} \frac{\partial p}{\partial x} \frac{sin\kappa}{cos^2\kappa} + \frac{K_n(x, r)}{h} W^2 \frac{1}{2} sin(2\delta + K_{off}). \tag{2.18}$$

Peters' volumetric source term model was shown to capture the flow features for a low speed fan with continuous positive deviation angles.

Expanding upon Gong's parallel force model, Peters implemented an off-design formulation to capture the variation in blade losses with operating condition. Peters formulation uses a mix of quadratic dependence on mass-averaged relative Mach number at the blade row inlet, combined with the existing quadratic dependence on local relative velocity,

$$f_p = \frac{K_{p1}}{h} \left[\left(\overline{M}_{rel}^M\right)^2 + K_{p2} \left(\overline{M}_{rel}^M - M_{ref}\right)^2 \right] W^2, \tag{2.19}$$

where K_{p1} and K_{p2} are viscous force coefficients, $\overline{M}_{rel}^M$ is the mass-averaged relative Mach number at the blade row inlet, and M_{ref} is the value of $\overline{M}_{rel}^M$ at peak efficiency. This formulation produces the desired quadratic loss profile typical of turbomachines.

In this research, Peters' loss model is used, however, the normal force poorly predicted the desired characteristic slope. This is due to the use of offset, K_{off}, which is unavoidable due to zero-value local flow deviations across the blade. For this reason, a different normal force model is used in conjunction with Peters' loss model.

2.4.3 Low-Speed Normal Force Model

More recently, an incompressible, inviscid normal force model was developed by Hall et al. [18]. The inviscid assumption eliminates the use of a parallel force model. The normal force model is a function of local flow quantities and blade camber angle, allowing the volumetric source term to be formulated without the need of a single passage RANS calculation for calibration. This is especially useful as a tool for commercial development of blade designs. The normal source, per unit mass, is defined,

$$f_n = \frac{(2\pi\delta)\left(\frac{1}{2}W^2/\,|n_\theta|\right)}{2\pi r/B}, \tag{2.20}$$

where n_θ is the circumferential projection of the local blade normal vector. In low solidity blades, the constant 2π yields a normal force equivalent to thin airfoil lift theory ($c_L = 2\pi\delta$). These low solidity blades have larger spacing between consecutive blades, therefore the blade to blade interaction is reduced, and flat plate lift theory is applicable. Conversely, in high solidity blades, the blade spacing is minimal and blade-relative flow is unable to circumferentially shift. The resultant is local flow deviation approaching zero ($\delta \to 0$) [18]. An adaptation of this incompressible normal force model is used in this work.

2.5 Performance Metrics

To assess the performance of the rotor and stator blades, three key performance characteristics are used in this thesis: isentropic efficiency, diffusion factor, and entropy-based loss coefficient.

2.5.1 Calculation of Efficiency in Uniform and Non-Uniform Flow

Isentropic efficiency is a metric used to assess the rotor efficiency in imparting energy to the flow, compared to an ideal, isentropic rotor. Due to system losses, a non-ideal rotor requires additional work input to produce the same total pressure rise as an isentropic rotor. In the case of a compressor, the isentropic efficiency is the ratio of isentropic rotor work to actual rotor work,

$$\eta_{is} = \frac{(\Delta h_t)_{ideal}}{(\Delta h_t)_{actual}}, \tag{2.21}$$

where Δh_t is the change in total enthalpy. Using isentropic flow relationships for a perfect gas, the ideal total enthalpy change is calculated,

$$\Delta h_o = c_p T_{t1} \left[\left(\frac{p_{t2}}{p_{t1}} \right)^{\frac{\gamma-1}{\gamma}} - 1 \right]. \tag{2.22}$$

Here, c_p is the specific heat capacity of air at constant pressure , T_t is the total temperature, p_t is the total pressure, and γ is the ratio of specific heats. Subscripts 1 and 2 represent the rotor inlet and outlet measurement planes, respectively. Equations 2.21 and 2.22 are combined to produce the rotor isentropic efficiency,

$$\eta_{is} = \frac{c_p T_{t1} \left[\left(\frac{p_{t2}}{p_{t1}} \right)^{\frac{\gamma-1}{\gamma}} - 1 \right]}{h_{t2} - h_{t1}}. \tag{2.23}$$

In the case of a volumetric source term model subjected to uniform inflow, this calculation is trivial. Since the upstream and downstream quantities are both axisymmetric, the value at each radial location needs to be determined, but there is no circumferential variation. For the non-uniform flow cases, however, the efficiency must be tracked and calculated along a streamline. This is due to the upstream spatial variation of total temperature and/or total total pressure. Finally, with the value of η_{is} determined

at each spatial location, the overall efficiency (isentropic or polytropic) is calculated using a mass-weighted average,

$$\overline{\eta}_{is}^{M} = \frac{\int \eta_{is} d\dot{m}}{\int d\dot{m}}.$$ (2.24)

2.5.2 Entropy-Based Loss Coefficient

As no work is done by a stator blade row on the flow, isentropic efficiency is not a reasonable metric to quantify the flow losses across the blade. Instead, an entropy-based loss coefficient is defined [20]

$$\zeta_3 = \frac{T_3 \Delta s_{2-3}}{(h_{t3} - h_3)}$$ (2.25)

where T_3 is the outlet static temperature, Δs_{2-3} is the entropy change across the stator blade row, and $(h_{t3} - h_3)$ represents the flow kinetic energy per unit mass at the blade outlet. The use of subscript 3 on ζ indicates that the loss coefficient is based on the stator blade row. A subscript of 2 is used to describe losses across the rotor blade row. In Equation 2.25, the numerator represents the lost work potential across the blade row. An advantage of this loss coefficient is that each component is calculated in the stationary reference frame regardless of whether it is for a rotor or stator.

A pressure-based loss coefficient has also been used in literature [21],

$$\omega = \frac{p_{t1,rel} - p_{t2,rel}}{p_{t2,rel} - p_2},$$ (2.26)

where the change in relative total pressure is computed across the blade row. The relative total pressure is calculated as

$$p_{t,rel} = p \left(1 + \frac{\gamma - 1}{2} M_{rel}^2 \right)^{\frac{\gamma}{\gamma - 1}}.$$ (2.27)

Equation 2.27 illustrates the relative total pressure's dependence on relative Mach number and in turn, relative velocity. Along a streamline, radial shifts due to machine geometry produce an associated change in relative velocity, in rotating components. For this reason, the loss coefficient shown in Equation 2.25 is used in this thesis.

2.5.3 Diffusion Factor

One of the goals of this research is to study the validity of using diffusion factor changes as a proxy for isentropic efficiency changes. The diffusion factor used is an adaptation of Lieblein's diffusion factor [?],

$$D = 1 - \frac{W_{out}}{W_{in}} + \frac{1}{2} \frac{|r_{out}W_{\theta,out} - r_{in}W_{\theta,in}|}{W_{in}} \frac{2\pi/B}{c_{ref}} \tag{2.28}$$

where the velocity, W, is in the relative frame for the rotor and absolute frame for the stator, and c_{ref} is the midspan chord for each of the respective blades. This diffusion factor accounts for both bulk diffusion as well as flow turning [10]. Diffusion factor was developed through boundary layer and pressure distribution theory across a compressor blade. The resultant diffusion factor provides a correlation between increased losses associated with increased blade loading. Therefore, diffusion factor changes are also correlated with isentropic efficiency changes, that is,

$$\Delta D = f(\Delta \eta_{is}) \tag{2.29}$$

As with the two previous performance metrics, the diffusion factor is calculated by tracking a streamline from inlet to outlet of each the rotor and stator blades.

2.6 State of the Art and Limitations of Previous Research

To observe distortion transfer in single stage turbomachinery, the current state-of-the-art is comprised of two separate methodologies: full annulus URANS calculations or steady volumetric source term representation of blade rows . With URANS calculations, computational costs have limited past research to observation of single distortions. For a low-speed fan, an inviscid normal force model has been used to observe several distortions. To the author's knowledge, no study on scaling between different distortions for a transonic fan has been carried out.

To achieve this improvement to the state-of-the-art, this work makes use of a compressibility correction to the incompressible normal force model, in combination with a double-sided loss model. Doing so produces a transonic blade volumetric source term model, allowing for a reduced full annulus computational cost. The output of the work is a parametric study of compressor performance scaling for a transonic fan in the presence of various distortion patterns and intensities.

Chapter 3

Approach

This chapter details the approach used to generate a transonic volumetric source term model and the non-uniform flow cases of interest. A high-level overview of the methodology employed in developing this volumetric source term model is first presented. Following that, the chronological steps in developing the volumetric source term are explained in detail, and finally the development and selection of a matrix of inlet distortions is outlined.

3.1 High-Level Overview of Transonic Volumetric Source Term Model

To accurately model the stagnation pressure rise, flow turning, and viscous losses through a transonic compressor stage, an innovative viscous volumetric source term model is developed. This model is a combination of adaptations from the normal force created by Hall, Greitzer, and Tan [18] and the parallel (viscous) force from Peters [15]. Figure 3-1 illustrates the work flow used to produce the final volumetric source term model. The machine and operating speed of interest must first be selected, from which the single-passage RANS speedline can be calculated, and finally the

resultant volumetric source term model can be developed from the extracted flow characteristics.
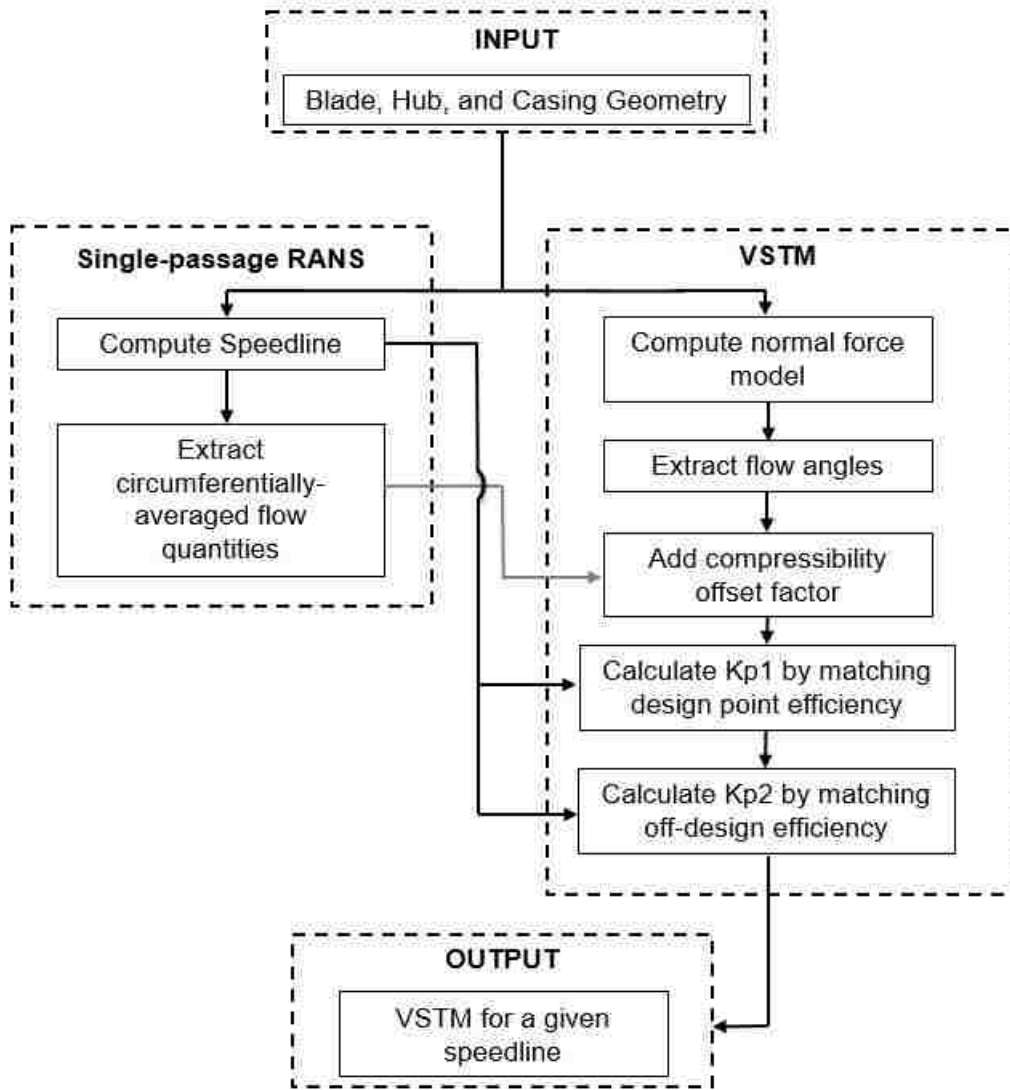
Figure 3-1: A high-level overview of the volumetric source term model creation process.

3.2 Machine of Interest

In this work, the transonic compressor NASA stage 67 is used. Important features for this machine are shown in Table 3.1. This single-stage, axial compressor is selected for three distinct reasons:

1. at 90% rotor speed, the tip relative Mach number is 1.20 [22], meaning that the flow is in the desired transonic regime for this study.

2. NASA stage 67 is the only known low hub-to-tip-ratio transonic compressor to have blade geometry and experimental results both available in the open literature.

3. Previous research completed by Fidalgo et al. [11] was performed on NASA Stage 67, meaning the accuracy of the volumetric source term model's response to non-uniform flow can be assessed.

With a mean hub-to-tip radius ratio of 0.427, this machine lies in between a fan and a typical compressor, meaning the flow response is similar to that of a first stage compressor or a fan in a low bypass ratio turbofan.

Table 3.1: Important design characteristics for NASA Rotor 67 at 90% speed [22, 11].

Ω (rad/s)	1512	σ_{hub}	3.11
$M_{rel,tip}$	1.20	σ_{tip}	1.29
FPR	1.48	$\left(\frac{r_{hub}}{r_{tip}}\right)_{inlet}$	0.375
$\dot{m}$ (kg/s)	31.10	$\left(\frac{r_{hub}}{r_{tip}}\right)_{outlet}$	0.478
B	22	η_{is} (%)	92.2
AR (Aspect Ratio)	1.56	$\phi = \frac{\overline{v_x}^M}{U_{mid}}$	0.50
$\frac{tip\,clearance}{r_{tip}}$ (%)	0.39		

The rotor consists of 22 blades which rotate clock-wise (facing downstream); the stator has 36 blades. A NASA technical report on rotor 67 has made blade data available at 14 spanwise locations for the rotor, and 16 spanwise locations for the stator [22]. At each of these spanwise locations, blade geometry is given in cylindrical coordinates, from blade leading edge to trailing edge and back to the leading edge.

Figure 3-2 shows blade stacking of the available data. Additionally, streamline data is given along the meridional axis, where the low-radius streamline represents the hub, and the high-radius streamline represents the casing.
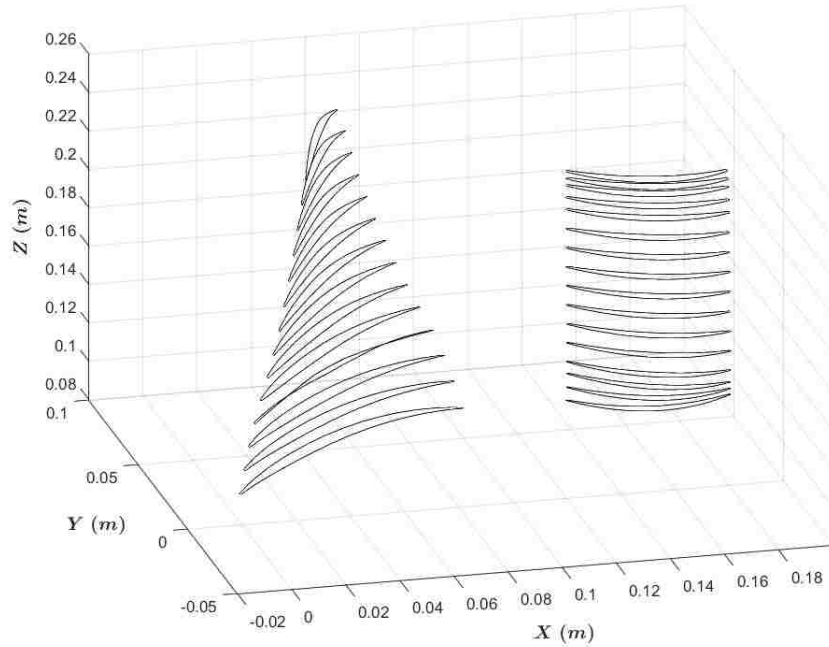
Figure 3-2: Rotor and Stator blade profiles for NASA Stage 67.

Geometry for the upstream and downstream ducts are not available. Instead, an artificial nose and inlet duct is produced to match those used in the study by Fidalgo et al. [11]. The nose itself is stationary, and only a portion of the hub rotates with the rotor, as shown in Figure 3-3. In this sense, the machine behaves as a compressor rather than as a fan; the latter would typically have a rotating nose. The downstream duct is different from Fidalgo et al. in that a converging nozzle is not used. Converging nozzles are typically placed far enough downstream to avoid any upstream flow influence. They are used to aid in reaching a converged computational fluid dynamics (CFD) solution near stall conditions [23]. In this work, only solutions near design are needed.
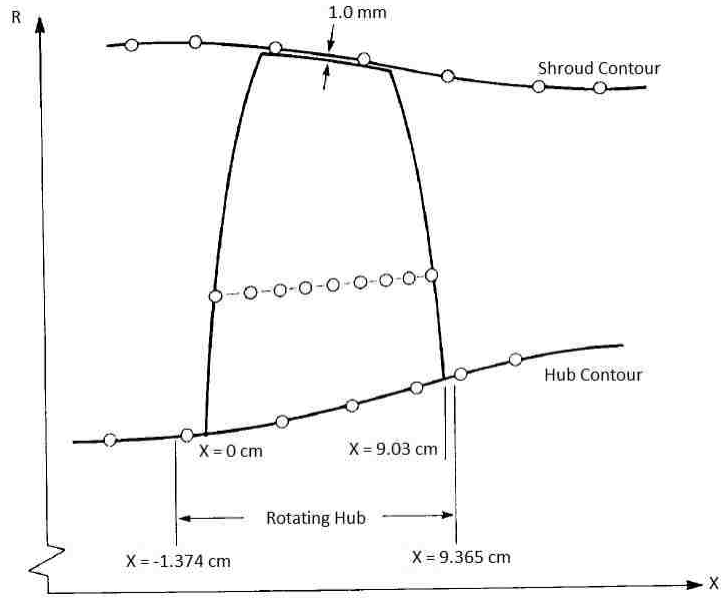
Figure 3-3: Rotational and non-rotational sections of the NASA Rotor 67 hub [22].

3.3   Single-Passage Computational Setup and Speed-line Results

Using the data available in Section 3.2, single passage RANS computations are set up. This process consists of four phases:

1. computer-aided design (CAD) model,

2. grid generation,

3. CFD setup, and

4. CFD calculation using external resources.

Each of these steps are explained in detail in this section.

3.3.1 CAD Model

Using the blade data available, the single passage domain is created using AutoDesk Inventor, a 3D CAD software package [24]. The machine inlet is placed approximately 10 rotor chords upstream of the rotor inlet, and the machine outlet approximately 10 stator chords downstream of the stator outlet. A full annulus 3D model of the machine used is shown in Figure 3-4.
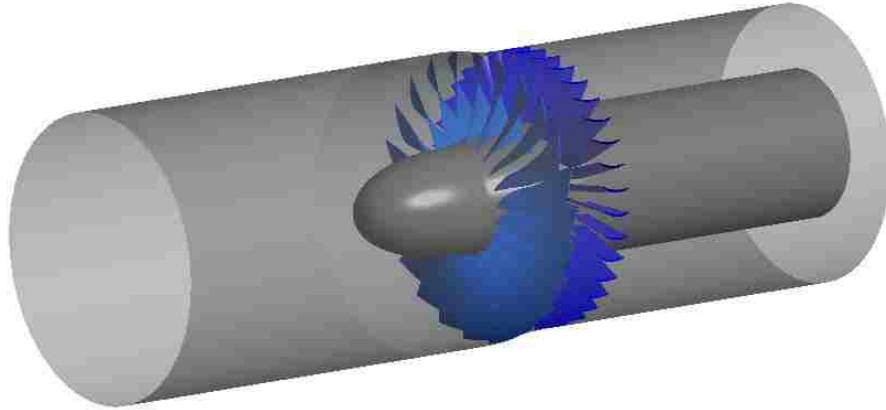
Figure 3-4: 3D CAD model of the NASA 67 machine, including artificial upstream and downstream ducts.

3.3.2 Grid Generation

The single passage grid is comprised of two sections, shown in Figure 3-5. The first section, the domain inlet, is produced using Pointwise [25]. Pointwise is a mesh generation software with the capability of producing a completely user-customized grid. The remaining sections of the grid, namely the rotor inlet, rotor blade, stator blade, and downstream duct are created using ANSYS TurboGrid [26]. Due to the complexity of the grid near the physical blade, TurboGrid is the preferred software for this region. TurboGrid makes use of an automated grid generation algorithm, catered towards the study of turbomachinery. As its name suggests, the single passage grid represents one single blade passage meaning 1/22 of the inlet and rotor region and

1/36 of the stator and outlet regions. An illustration of the single passage rotor and stator grid topologies is shown in Figure 3-6.
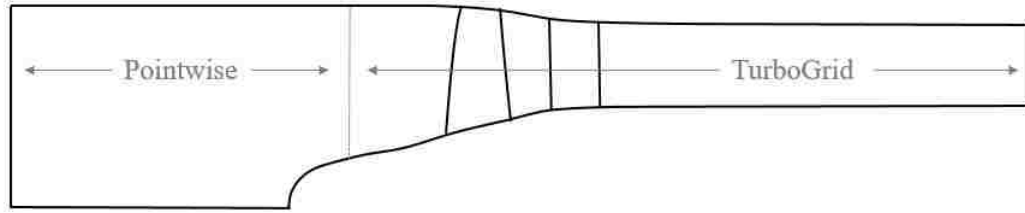
Figure 3-5: Single passage grid generation software usage.
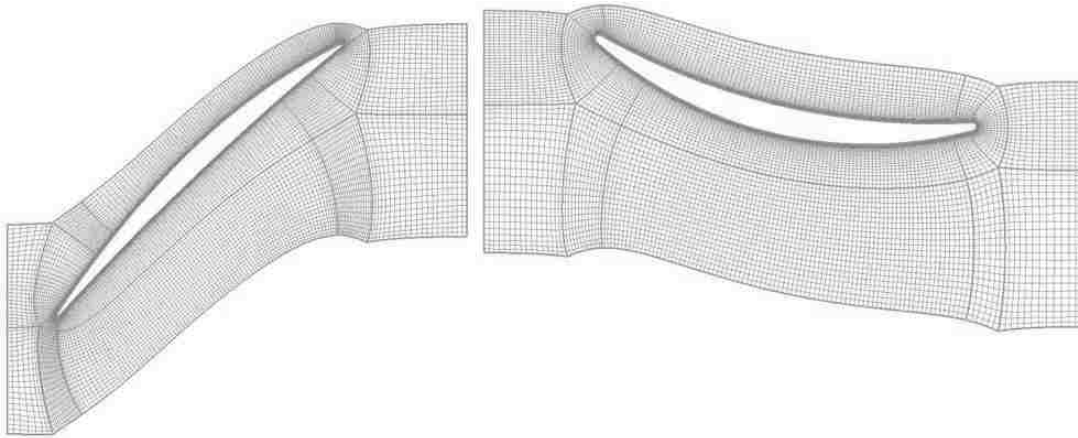
Figure 3-6: Single Passage rotor (left) and stator (right) grid topologies at midspan.

NASA Stage 67 rotor has a large stagger angle near the blade tip. This is a characteristic shared with fan blades, as the large radius creates high rotor blade velocity, requiring a steep blade angle. Due do this stagger, the complexity of the grid is significantly increased in these outer span locations, driving home the importance of using TurboGrid, as opposed to a more manual grid generation method. Another advantage of TurboGrid is its handling of a non-conformal tip gap. In the rotor region, a tip gap of $0.0039R_{tip}$ is needed to allow the rotor clearance while in operation. An overhead view of the rotor blade, Figure 3-7, shows the grid generated in the tip gap region and the non-conformal grid intersection.
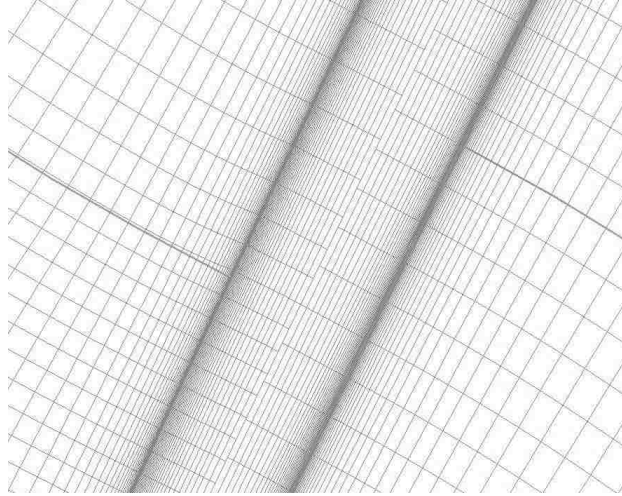
Figure 3-7: Overhead view of the rotor blade tip; rotor tip gap grid.

Finally, the upstream grid generated in Pointwise, and the rotor, stator, and downstream grids generated in TurboGrid are imported to CFX to produce one single grid with no geometric gaps. Grid count statistics are shown in Table 3.2, where the relative grid density, v, is calculated as

$$v = \frac{Cell\,\%}{Volume\,\%}.$$

(3.1)

As expected, the relative grid density is greatest in the rotor and stator, with values of 6.747 and 9.301 respectively. NASA stage 67 is comprised of 22 rotor blades and 36 rotor blades, meaning comparatively, there is reduced blade spacing within the stator. Blade boundary layer regions require increased cell density, which is why the stator domain with 36 blades has a larger relative grid density than the rotor. The total grid count is 96,163,722 cells, more than twice the density used by Fidalgo et al., 42,500,000[11]. Their study were performed on the identical NASA Stage 67 machine, however, they were performing an unsteady full annulus calculation where an increased cell count comes at a severe computational time penalty. Due to the increased grid density, in addition to the availability of both experimental and previous CFD results, an extensive grid independence study is unnecessary.

Table 3.2: Grid count statistics for both single passage and full annulus RANS calculations.

Region	Cells/ Passage	Passages/ 360°	Cells/360°	Volume %	Cell %	υ
Inlet	458,346	22	10,083,612	52.89	10.49	0.198
Rotor Inlet	106,848	22	2,350,656	8.42	2.44	0.290
Rotor	1,781,061	22	39,183,342	6.04	40.75	6.747
Stator	1,065,792	36	38,368,512	4.29	39.90	9.301
Outlet	171,600	36	6,177,600	28.37	6.42	0.226
Total	3,583,647		96,163,722			

3.3.3 Single-Passage RANS Grid Independence

Availability of experimental data and previous CFD calculations limits the required grid independence study. At a minimum, two grids need to be tested to ensure a grid refinement does not change the computational result to a significant degree. Ideally, a more coarse grid should be tested as well to determine if the total cell count can be reduced. In the case of Fidalgo et al., a single passage rotor grid count of 1.18 million cells was used [11]. This serves as a starting point for rotor grid density. Several grids are produced using TurboGrid. Table 3.3 shows the final grid resolutions. It is determined that the medium grid density is a sufficient grid. The total pressure ratio and isentropic efficiency both change by less than 1%.

Table 3.3: A summary of the grid independence study performed.

	Medium Grid	Fine Grid	Percent Change
Rotor Cell Count	1.78×10^6	2.45×10^6	37.6%
FPR	1.493	1.496	0.71%
Rotor η_{is}	0.9231	0.9229	0.022%

3.3.4 CFD Case Setup

The commercial software ANSYS CFX is used as the CFD solver for this work [27]. This software has been designed and customized for applications involving rotating machinery [27]. CFX includes a pre-processor and solver, allowing the case setup and calculation to be completed on one platform. CFD-Post, an ANSYS package, and Matlab are used for post-processing [28].

The generated grids are imported to CFX-Pre, with the single-passage setup shown in Figure 3-8. The calculation is steady state, with the shear-stress transport (SST) turbulence model [29]. This turbulence model is especially useful in capturing the separation of flow over a smooth surface in an adverse pressure gradient [27]. It is a two equation turbulence model widely used in turbomachinery [27]. CFX recommends a boundary layer resolution of a minimum of 10 nodes in order to accurately capture the secondary flow effects; in this study a boundary layer with a minimum of 15 layers is used. A non-conformal grid, and a general grid interface (GGI) within CFX, is used in the tip gap region. The boundary layer cell specification is, however, unchanged in this region, with a minimum of 15 boundary layer cells used. Within the entire domain, the y+ value does not exceed 40. At the inlet of the domain, total conditions are specified and the flow direction is normal to the inlet face. Two separate outlet conditions are imposed, depending on the flow coefficient. In flow conditions near choke, the static pressure is specified at outlet until the desired flow coefficient is achieved. This is performed to accommodate for the nature of a compressor characteristic, where the total pressure ratio is highly sensitive to static pressure changes near choke. Near stall, the physical mass flow is specified as the outlet condition. At flow coefficients away from these two critical values, the mass flow rate outlet condition is once again used, as it allowed for a desired flow coefficient to be directly obtained, as opposed to an arbitrary static pressure value. The no-slip condition is imposed on all walls.
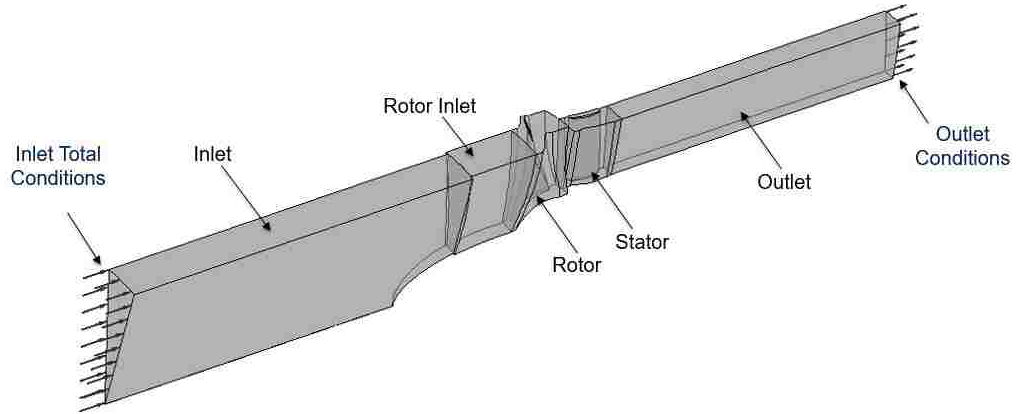
Figure 3-8: Single-passage domain as defined in CFX-Pre.

To compare the single passage results to NASA experimental values for R67, 100% rotational speed (1680 rad/s) is needed. However, with a tip relative Mach number of 1.38, severe stator separations are expected in the presence of distortion [11]. For this reason, the distortion study performed by Fidalgo et al. was calculated at 90% rotational speed [11]. Thus, the work in this thesis is also performed at 90% rotational speed (1512 rad/s).

In a steady calculation of rotating axial turbomachinery, the flow travels from a stationary frame (inlet) to a rotating frame (rotor) and back again (stator). To transfer flow data downstream across a changing reference frame, a mixing plane is necessary. In this machine, a mixing plane is needed between the upstream region and rotor, and once again between the rotor and stator. Within CFX, the stage mixing plane is used. This type of mixing plane circumferentially averages the flow at the domain outlet and converts it to the appropriate reference frame. In the process of averaging, the mixing plane incurs a mixing loss, where the upstream domain is allowed to mix out any velocity variations before entering the downstream domain [27]. The effect of this mixing plane can be seen in Figure 3-9, the pressure loss coefficient from rotor to stator is $\omega = 0.0089$. To minimize the effect of this mixing plane upstream of the rotor, where upstream rotor effects are present, the mixing

plane is moved two chords upstream of the rotor. As a result, the rotor inlet region is created. This region has the same rotational speed as the rotor, with the use of counter-rotating walls to keep the boundary conditions consistent with that of the actual machine. When placing the mixing plane between the rotor and stator regions, the midpoint is selected.
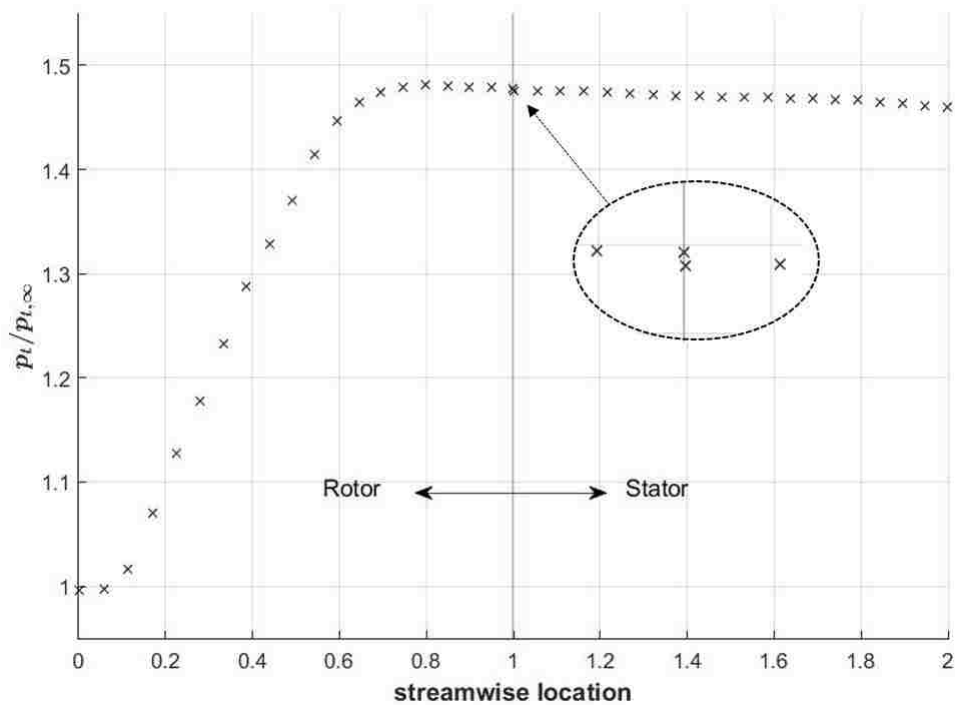
Figure 3-9: Artificial mixing loss when using a stage interface between rotating and non-rotating frames.

3.3.5 Computational Resource

To significantly reduce the computational time, Sharcnet is used as a computing resource. This cluster of high-performance computers is available to 18 Canadian academic institutions [30], allowing for the scope of this research to be realizable. Job submissions vary based on several factors including initializing conditions, grid density, Sharcnet resource availability, and the purpose of the submission. A typical setup allows for the parallel usage of 24 CPUs and 48GB RAM.

37

3.3.6 Single Passage Results

For 90% rotational speed, Fidalgo et al. have published both experimental and CFD results of rotor total pressure ratio and isentropic efficiency [11]. Those results are compared against the single-passage results obtained in this work in Figure 3-10. The values obtained for total pressure ratio are in agreement with both experimental and Fidalgo et al. CFD data, with an error ranging from 0.3% to 3.8%. The rotor isentropic efficiency, near design corrected mass flow rate (31.1 kg/s), lies in between the experimental and Fidalgo et al. computed values. At flow coefficients (mass flow rates) near choke, the experimental data for isentropic efficiency has large variability, making it difficult to calculate absolute error. In this region, the results from this work lie between experimental and Fidalgo et al. CFD results. When comparing the results from this work to that of Fidalgo et al., the use of a different grid and solver, is the main source of inconsistency. It is also noteworthy that the corrected mass flow rate of the CFD results is only run to a minimum of 30.07 kg/s. The reason for this is instability in the solver as the rotor incidence angles become larger and flow separations are more severe. To obtain values at lower mass flow rates, an unsteady calculation, or choked nozzle is necessary. However, this is not necessary in this work, as data extraction is only needed at peak efficiency.
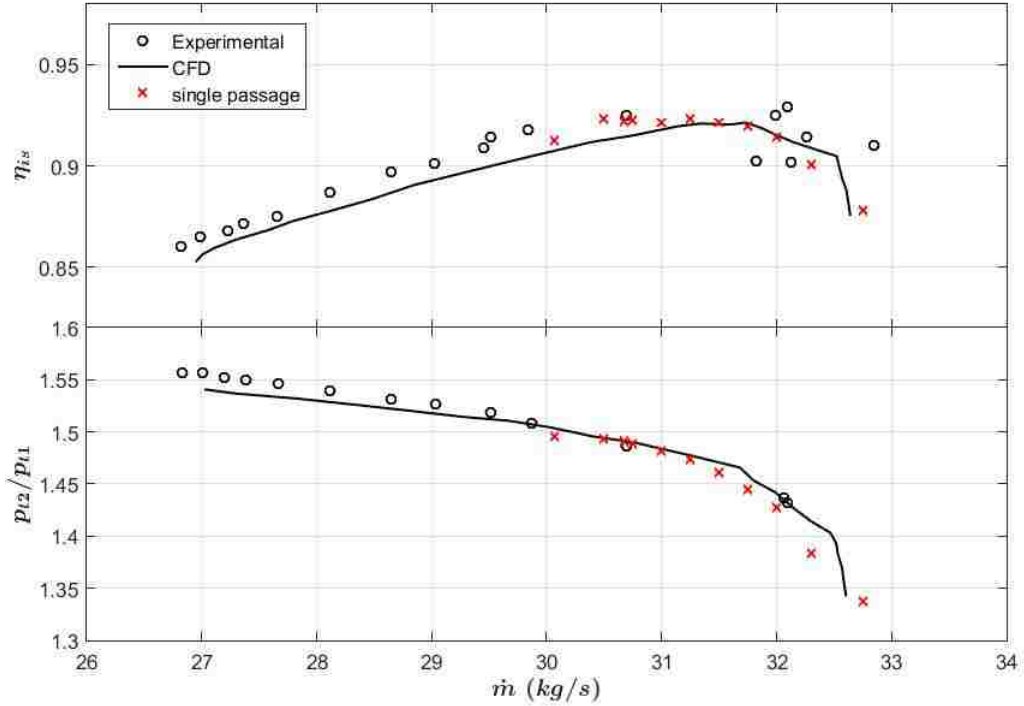
Figure 3-10: Single passage 90% rotor speed, η_{is} and FPR results against experimental and Fidalgo et al. CFD [11].

3.4 Volumetric Source Term Model Domain Setup

As outline in section 2.4, the volumetric source term model is a pitchwise-averaged representation of the actual machine. The computational domain is thus a meridional projection of the single passage domain, rotated about the axial direction. The rotor and stator domains encompass the swept volume of the physical blades. Since the volumetric source terms are frame-independent, there are no rotational sections, allowing for one continuous grid. For uniform flow cases, the circumferential rotation of the grid is a 1/16th sector of the full annulus. However, non-axisymmetric inflow distortions require a full annulus domain. The resultant volumetric source term model domain, for uniform inflow (1/16 section), is shown in Figure 3-11 and measurement station locations are shown in Figure 3-12. The grid used in the volumetric source domain is produced entirely within Pointwise. It is a single, continuous, axi-symmetric

grid with no rotating components. A meridional view of the rotor and stator grids
shown in Figure 3-13.
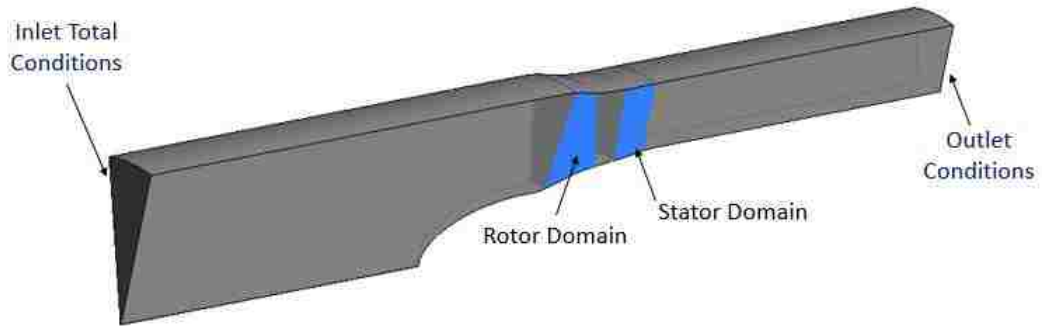
Figure 3-11: Uniform inflow volumetric source term model domain, a 1/16th sector
of the full annulus machine.
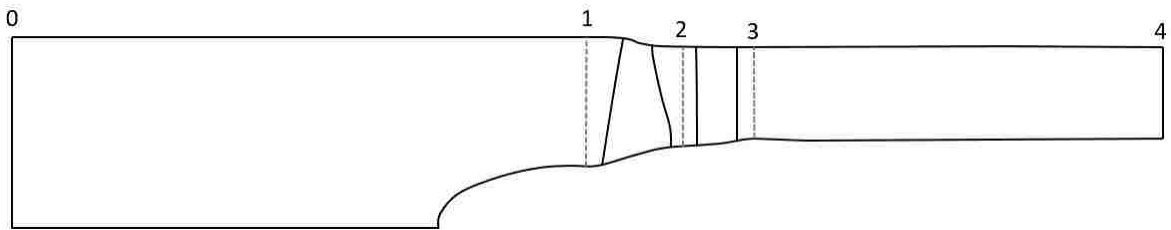
Figure 3-12: Axial measurement locations in the volumetric source term grid.
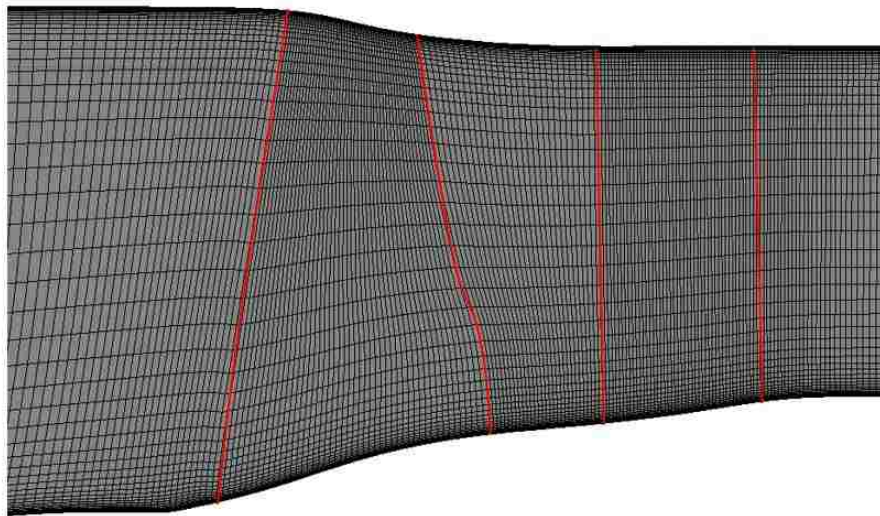
Figure 3-13: Volumetric source term model, rotor domain grid (left) and stator do-
main grid (right) outlined in red.

Inlet total conditions, mass flow outlet , free-slip walls, a periodic rotational interface, and a ratio of specific heats of $\gamma = 1.4$ is used. The rationale for use of free-slip walls is presented later in this section. The same turbulence model, SST, is used as in the single passage calculations. In determining an automatic time scale, CFX makes use of two characteristic length scales [27],

$$L_{vol} = \sqrt[3]{V}, \tag{3.2}$$

$$L_{ext} = max(L_x,\ L_y,\ L_z), \tag{3.3}$$

where V is the domain volume, and L_x, L_y, and L_z are the x, y, and z extents of the domain. The length scale for a conservative scheme is the minimum of the two length scales,

$$L_{scale} = min(L_{vol},\ L_{ext}). \tag{3.4}$$

For a conservative scheme, the velocity scale is calculated as the maximum arithmetic average velocity at any boundary [27],

$$v_{scale} = max\left|\bar{v}_{bc}\right|. \tag{3.5}$$

The ratio of velocity to length scales, multiplied by a factor of 0.3 is used as the conservative automatic time scale. In this volumetric source grid, a physical time scale equal to 50.7% of the conservative automatic time scaled is used to ensure stability of the computations.

NASA stage67 contains sharp hub radius increases in the rotor and stator domains. Within the stator, these area contractions coincide with the adverse pressure gradient produced by flow straightening and boundary layer development. Due to

these conditions, non-physical severe flow separation and subsequent re-circulation is observed. The separation is not consistent with the results observed in the single passage model. To avoid the separation, slip-wall conditions are used. Within the rotor and stator blade regions, the parallel force model accounts for the end-wall losses. Using slip-wall conditions leads to the absence of boundary layer development upstream of the rotor. While it is desired to be able to capture this effect, the use of slip-walls only affects the flow in the bottom 5% span and upper 5% span. For the purpose of this study, the overall efficiency trends are still observable.

Without the physical presence of blades in the volumetric source term model, flow is able to circulate in the tip gap region, as it is unimpeded by a solid blade. An ideal volumetric source term model would allow for the the tip gap region to be a separate domain from the rotor, in which volumetric source terms do not exist. However, this is not possible in this model, as this tip flow circulation previously discussed leads to a divergent solution. To overcome this, the normal and parallel forces in the last 3 spanwise cell locations are averaged and then extrapolated to the tip region. By eliminating the tip gap, work is done on the flow in this region, meaning the total enthalpy rise is over-estimated, and the tip leakage flow details cannot be observed. The tip gap in this machine is less than 0.4% of the blade span. A comparison of the mass flux between the volumetric source term model and single-passage model at 1% rotor chord is shown in Figure 3-14, which illustrates the effect of eliminating the tip gap. The volumetric source term model continues to push the mass flux through the machine, even in the tap gap, whereas the single passage tip leakage exhibits itself as a mass flux deficit.
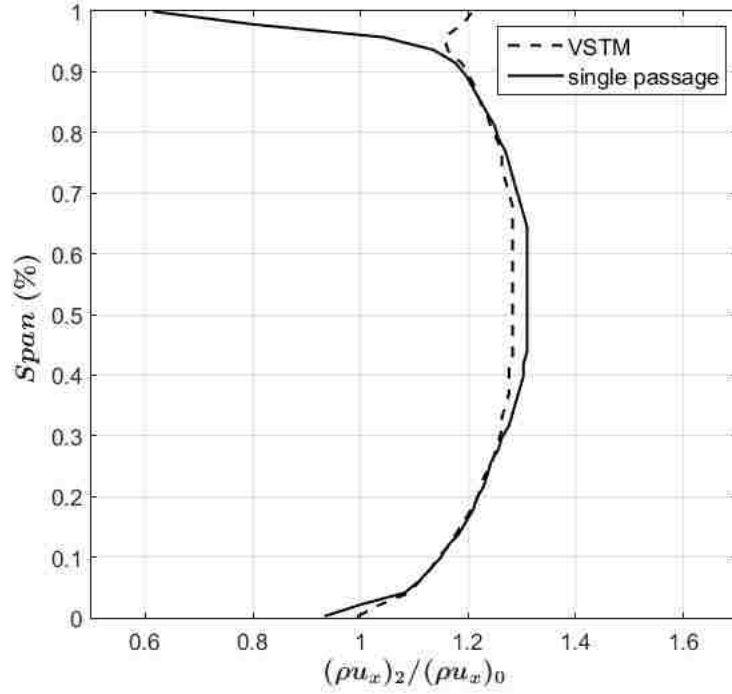
Figure 3-14: Spanwise rotor exit total temperature ratio; tip gap leakage is not modelled in VSTM.

3.5   Normal Force - Compressibility Correction

The normal force model in this work is based on incompressible thin airfoil theory. To account for flow compressibility, a three-step process is carried out:

1. incompressible normal force calculation,

2. iterative calculation of compressibility correction constant, ϵ, and

3. blade re-cambering.

As detailed in section 2.4.3, the Hall et al. normal force model is based on thin airfoil theory [18] and the force per unit mass is,

$$
f_n = \frac{(2\pi\delta)\left(\frac{1}{2}W^2/|n_\theta|\right)}{2\pi r/B},
\tag{3.6}
$$

where δ is the deviation angle, W is the relative velocity, $|n_\theta|$ is the camber surface normal projection on to the azimuthal direction, r is the radius, and B is the number of blades. This equation can be further simplified using the staggered blade spacing relationship [15],

$$h = \frac{2\pi r \sqrt{\sigma} cos\kappa}{B},$$ (3.7)

so that

$$f_n = \pi\sqrt{\sigma}\frac{\delta W^2 cos\kappa}{h|n_\theta|},$$ (3.8)

where σ is the blade solidity and κ is the blade metal angle. Finally, the trigonometric relationship shown in Figure 3-15 can be used to produce the final equivalent form of this normal force equation

$$f_n = \pi\sqrt{\sigma}\frac{\delta W^2}{h}.$$ (3.9)
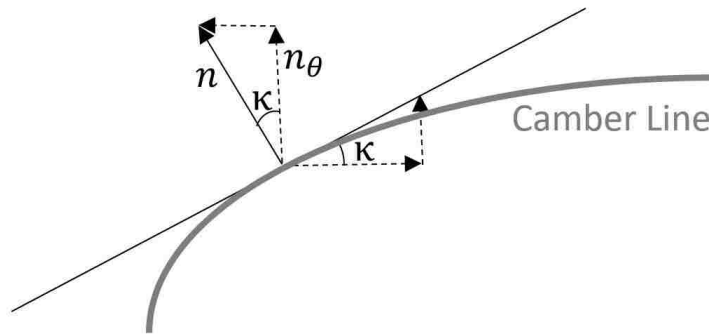
Figure 3-15: Example blade passage used to illustrate the relationship between $cos\kappa$ and $|n_\theta|$.

To adapt this model for a transonic fan, a compressibility correction constant, ϵ, is added to the local deviation angle,

$$f_n = \pi \sqrt{\sigma} \frac{[\delta + \epsilon] W^2}{h}, \tag{3.10}$$

where ϵ is a spatially dependent constant. The constant itself is calculated from an observation in the Euler turbine equation,

$$h_{t,out} - h_{t,in} = \omega \left(r_{out} v_{\theta,out} - r_{in} v_{\theta,in} \right). \tag{3.11}$$

Knowing the volumetric source term model must produce the same stagnation enthalpy rise as the single-passage computations, if the relative swirl velocities are matched, so too will the enthalpy rise. In an attempt to accomplish this, the volumetric source term relative flow angles are matched to the single-passage relative flow angles, by making use of ϵ. An innovative method is used to match the relative flow angles. The volumetric source term model is calculated at peak efficiency, using Hall et al.'s original definition of the normal force, Equation 3.9. From the results, the relative flow angles are extracted within the rotor domain in the $x - r$ plane. These relative flow angles are then subtracted from the pitchwise-averaged, peak efficiency, single-passage flow angles, as illustrated in Figure 3-16. The resultant flow angle field becomes the new value of ϵ. Due to the non-linear relationship between incompressible and compressible flow turning, ϵ is not directly calculated, rather it is iterated upon. After each iteration, the new value of ϵ is a cumulative sum of previous iterations,

$$\epsilon_{i,total}(x, r) = \epsilon_{i,extracted}(x, r) + \epsilon_{i-1,total}(x, r). \tag{3.12}$$

To obtain the final spatial ϵ field, a series of 19 iterations are performed.
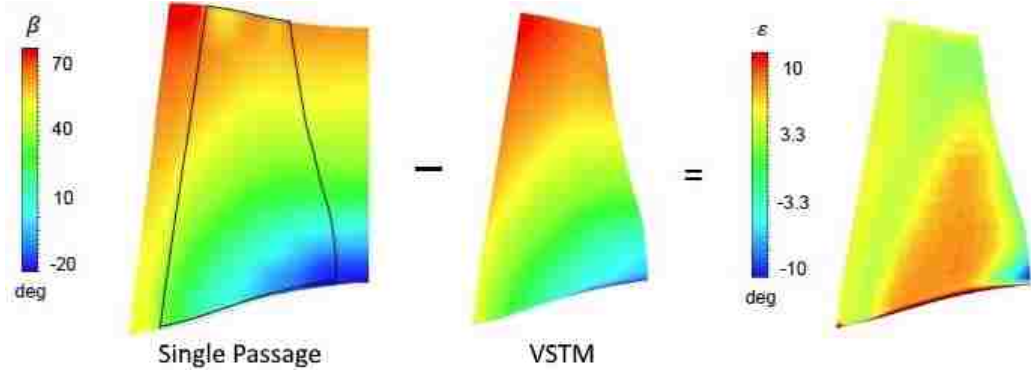
Figure 3-16: One iteration of the ϵ extraction process, comparing volumetric source term flow angles to single passage flow angles.

Matching the flow angles is only a first step in matching the total enthalpy rise, or exit swirl velocities. In a bladed single-passage calculation, the fan blades provide a physical blockage for the flow. This blockage effect is not modelled in the volumetric source term computation. The only means for axial mass flux gradients in the volumetric source term model is duct contraction or expansion. Therefore the axial velocity in the blade force model cannot be matched to the single passage calculation without altering the mass conservation equation. Instead, by matching the flow angles, as is done in the work, an incorrect axial velocity means that the swirl velocity is mismatched. There is no scenario is which both the swirl velocity and flow angle can be matched to the single-passage values, without blockage. In this volumetric source term model, rotor work is over-predicted in regions of increasing blade thickness, and under-predicted in regions of decreasing blade thickness. Figure 3-17 serves as a hypothetical example of this velocity mismatch. In this figure, blade thickness is increasing axially and the flow angle is conserved between single passage and volumetric source term, that is,

$$\beta_{1,SP} = \beta_{1,VSTM} \tag{3.13}$$

$$\beta_{2,SP} = \beta_{2,VSTM}, \tag{3.14}$$

.

without modeling blockage,

$$v_{x,1,SP} = v_{x,1,VSTM} \tag{3.15}$$

$$v_{x.2.SP} > v_{x,2,VSTM}, \tag{3.16}$$

which results in an uneven change in outlet swirl velocity,

$$\delta v_{\theta,rel,2,SP} < \delta v_{\theta,rel,2,VSTM}. \tag{3.17}$$
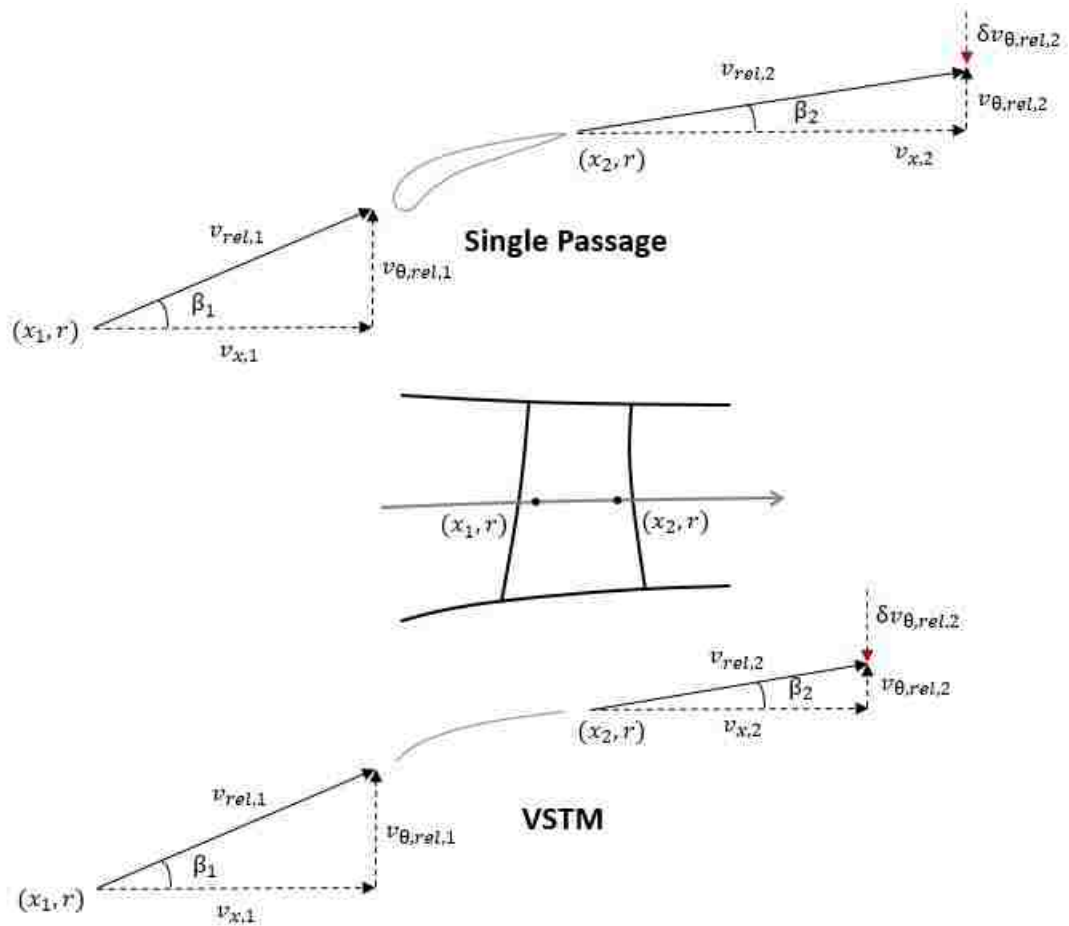
Figure 3-17: Mismatch of swirl velocity with a constrained flow angle due to the absence of blockage.

Since the work in the rotor is over-predicted, a blade camber line alteration is necessary to reduce the normal turning force. Within the volumetric source term normal force equation, the camber line, κ, controls the magnitude of flow turning and in turn, the work done on the flow by the rotor,

$$f_n = \pi\sqrt{\sigma}\frac{(\beta - \kappa)W^2}{h}.$$ (3.18)

Thus, to correct for over-predicted work, the rotor blade is re-cambered using the circumferentially-averaged spanwise rotor total temperature ratio from single passage RANS data. Since the blade loading is highest in the first quarter chord of the rotor blade, the re-cambering is performed linearly from leading edge to trailing edge, meaning that the camberline is unaltered at the leading edge. In performing a linear recambering, the resultant VSTM camberline is a blend of correct swirl angle at the leading edge and correct swirl velocity at the trailing edge. To produce the recambered blade, changes in flow angle from leading edge to trailing edge are extracted from single passage RANS and are used to radially scale the re-cambering. Doing so allows for the spanwise total temperature profile at rotor exit to be preserved.

The final form of the equation used for re-cambering is,

$$\kappa_{new}(x, r) = \kappa_{old}(x, r) + \Lambda\frac{(x - x_{LE}(r))}{(x_{TE}(r) - x_{LE}(r))}\left(\beta_{TE,SP}(r) - \beta_{LE,SP}(r)\right),$$ (3.19)

where $\kappa_{new}(x, r)$ is the new blade camber profile at each rotor grid point, $k_{old}(x, r)$ is the original camber profile at each rotor grid point, Λ is a re-cambering constant, x is the axial location within the rotor blade, $x_{LE}(r)$ and $x_{TE}(r)$ are the blade leading edge and trailing axial locations at radius r, and $\beta_{LE,SP}(r)$ and $\beta_{TE,SP}(r)$ are the relative flow angles at the leading edge and trailing edge of the single passage RANS results. The constant Λ is determined iteratively by comparing the rotor total temperature

ratio to the single passage RANS results; ultimately $\Lambda = 0.27$ is found to give the best agreement for the rotor-exit total temperature ratio vs. span profile between volumetric source term model and single passage RANS. The resultant rotor camber line profiles are shown versus the original rotor camber line profile is shown in Figure 3-18. The rotor total temperature ratio is plotted against mass flow rate in Figure 3-19 and a spanwise plot of rotor exit total temperature at peak efficiency before and after re-cambering is shown in Figure 3-20.

As an alternative, the normal force model can be constructed by matching the swirl velocity as opposed to the flow angles. Doing so, and again due to the absence of blockage modelling, the swirl velocity will be correct, but the flow angles will be incorrect. Incorrect flow angle, and in turn incidence angle, is especially detrimental at the blade leading edge. This is for two reasons: blade loading is most severe in the first 1/4 chord, and the normal force model is directly dependent on incidence angle. Future work will include a blockage model to circumvent the need for re-cambering.
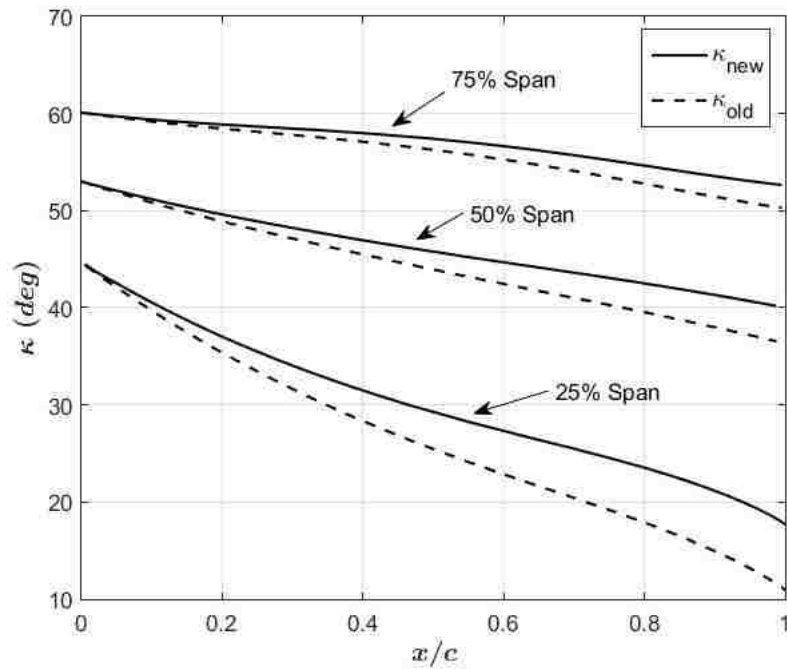
Figure 3-18: Rotor camber line angles, before and after re-cambering.
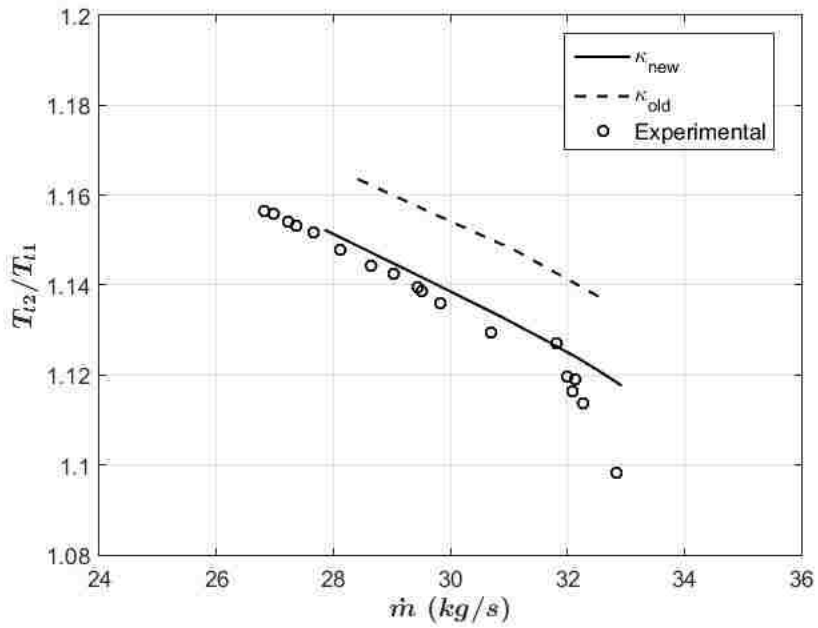
Figure 3-19: Rotor total temperature ratio, before and after re-cambering.
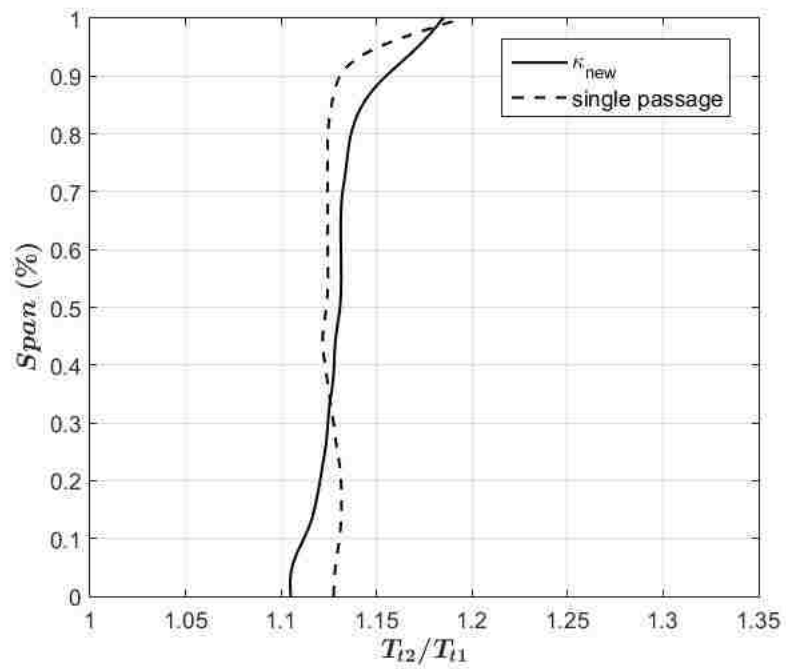
Figure 3-20: Spanwise rotor total temperature ratio at rotor exit at peak efficiency, compared to single passage results.

3.6   Updated Parallel Force Model

For NASA rotor 67, Peters parallel force model [15] requires a revision to allow the viscous model to replicate the shape of the desired efficiency versus corrected mass flow characteristic. Peters' model produces a rotor loss profile that has a quadratic dependence on blade-inlet relative Mach number, $\overline{M}_{rel}^{M}$,

$$f_p = \frac{K_{p1}}{h}\left[\left(\overline{M}_{rel}^{M}\right)^2 + K_{p2}\left(\overline{M}_{rel}^{M} - M_{ref}\right)^2\right]W^2. \tag{3.20}$$

The equation also contains quadratic dependence on the local relative velocity, W^2. $\overline{M}_{rel}^{M}$ is calculated as a mass-weighted average of an $y - z$ plane at the leading edge of the blade; station 1 for the rotor and station 2 for the stator. The shape of the efficiency characteristic can be altered by K_{p1}, K_{p2}, and M_{ref}. While K_{p1} and K_{p2} set the magnitude and slope of the efficiency curve, the constant M_{ref} is the single control point used to alter the shape of the resultant efficiency curve. By setting M_{ref} to equal $\overline{M}_{rel}^{M}$ at peak efficiency, the resultant efficiency vs. corrected mass flow characteristic is constrained as shown in Figure 3-21. K_{p1} controls the magnitude of peak efficiency and K_{p2} controls the slope of off-design efficiency. These constants do not allow for the creation of different efficiency characteristic shapes.

To allow for the design of more customizable efficiency curves, two innovations are implemented: M_{ref} is no longer located at the peak efficiency point, and a piecewise loss function is established,
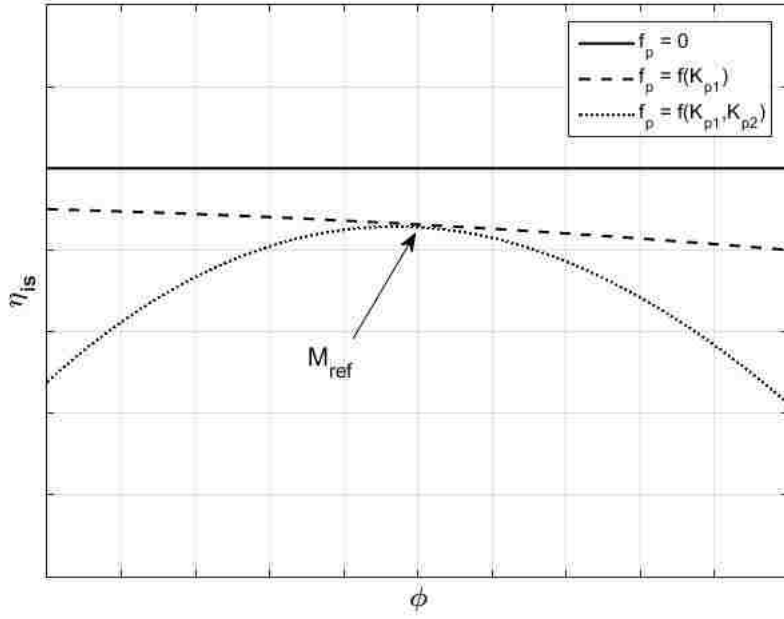
Figure 3-21: Peters' viscous model: rotor isentropic efficiency speedline is constrained to a near-quadratic shape.

$$f_{p,new} = \begin{cases} f_p & if \ \overline{M}_{rel}^M < M'_{ref} \\ f_p \left[1 + K'_{p2} \left(M'_{ref} - \overline{M}_{rel}^M \right)^2 \right] & if \ \overline{M}_{rel}^M > M'_{ref} \end{cases}, \qquad (3.21)$$

where K'_{p2} is a constant used to alter the efficiency at flow coefficients where $\overline{M}_{rel}^M > M'_{ref}$. The resulting formula allows for enhanced control of the resultant efficiency characteristic shape. M_{ref} and M'_{ref} serve as local loss minima within their respective multiplicative terms, allowing for 2 independent "shaping" variables. The values for K_{p1}, K_{p2}, K'_{p2}, M_{ref}, and M'_{ref} are calculated iteratively by comparing the resultant efficiency characteristic to the desired efficiency characteristic. The desired efficiency speedline is known from single-passage calculations, and each variable is adjusted until the desired output is obtained. The following is the expanded form of Equation 3.21, illustrating the difficulty of resolving an analytical solution:

$$f_{p,new} = \frac{\left(k_{p1} + k_{p1}k_{p2} + k_{p1}k_{p2}k'_{p2}\right)}{h} \left(\overline{M}^M_{rel}\right)^2 W^2 + \frac{k_{p1}k'_{p2}}{h} \left(\overline{M}^M_{rel}\right)^4 W^2 + \frac{k_{p1}k_{p2}}{h} M^2_{ref} W^2$$
$$- \frac{2k_{p1}k_{p2}}{h} \overline{M}^M_{rel} M_{ref} W^2 - \frac{-2k_{p1}k'_{p2}}{h} \left(\overline{M}^M_{rel}\right)^3 M'_{ref} W^2 + \frac{k_{p1}k'_{p2}}{h} \left(\overline{M}^M_{rel}\right)^2 \left(M'_{ref}\right)^2 W^2$$
$$- \frac{2k_{p1}k_{p2}k'_{p2}}{h} \overline{M}^M_{rel} M'_{ref} W^2 + \frac{k_{p1}k_{p2}k'_{p2}}{h} \left(M'_{ref}\right)^2 W^2 \tag{3.22}$$

To reduce the computational time required to solve for f_p, initial values are of significant importance. Given that the peak efficiency is known, the parallel force is initially reduced to the following form:

$$f_p = \frac{K_p}{h} \left(\overline{M}^M_{rel}\right) W^2. \tag{3.23}$$

Using this simplified form of the viscous model, K_p can be adjusted until the peak efficiency is matched to the single passage results. From here, the total viscous force at peak efficiency must remain constant in all future iterations. That means, despite the complex viscous force equation, when one variable is changed, there is a constraint on the other variables, such that the total value of f_p at peak efficiency must be conserved. Previously used values for K_{p1} (0.0336) and K_{p2} (0.6321) in the work by Patel [31] served as an initial guess. M_{ref} is initially set to be equal to $\overline{M}^M_{rel}$ at peak efficiency. The resulting constant values used in this work are shown in Table 3.4, the parallel force distribution is shown in Figure 3-22 and the resultant volumetric source term efficiency characteristic is shown in Figure 3-23. The new parallel force formulation is used in the rotor domain, and Peters' parallel force formulation is used unaltered in the stator. Without computational resources as a limiting factor, the revised parallel force model would be used in both domains. Future work will see this process automated and optimized to reduce computation time and increase parameter accuracy.

Table 3.4: Modified parallel force constant values for the rotor and stator domains.

Rotor		Stator	
k_{p1}	0.0145	k_{p1}	0.052
k_{p2}	650	k_{p2}	5
k'_{p2}	1125	k'_{p2}	n/a
M_{ref}	1.007	M_{ref}	0.6199
M'_{ref}	0.9870	M'_{ref}	n/a
$\left(\overline{M}^{M}_{rel}\right)_{peak-efficiency}$	0.9868	$\left(\overline{M}^{M}_{rel}\right)_{peak-efficiency}$	0.6045
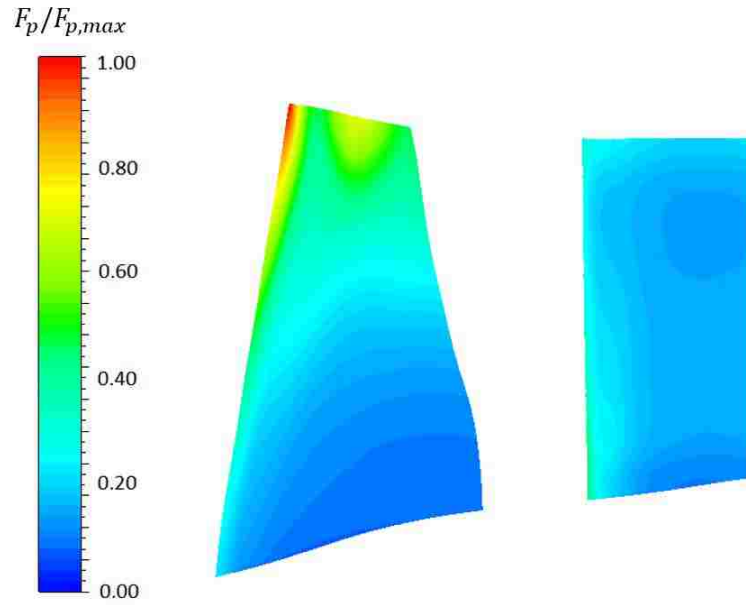
Figure 3-22: Rotor (left) and stator (right) parallel force values at peak efficiency.
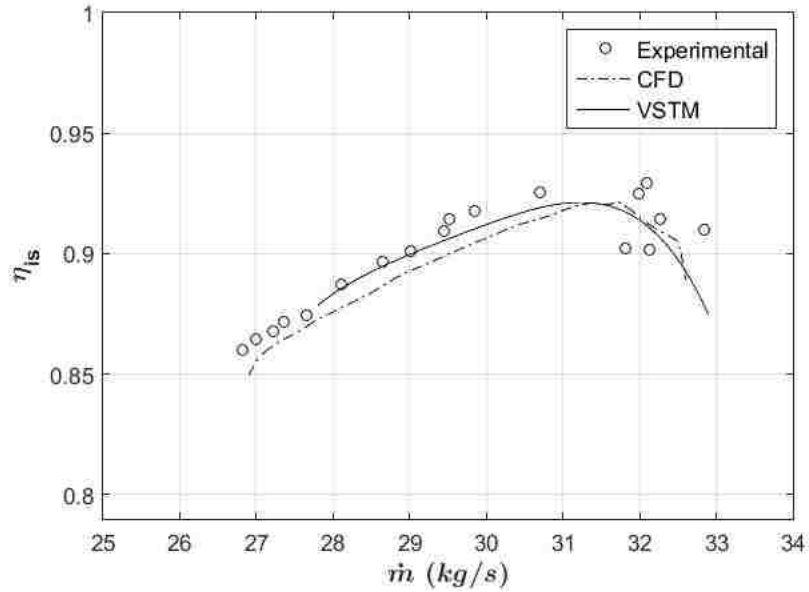
Figure 3-23: Volumetric source term rotor isentropic efficiency characteristic versus previously published results at 90% speed.

3.7   Implementation of the Volumetric Source Terms

As with the single passage model, CFX is used as the pre-processor and solver. The volumetric source term model is implemented as source terms in the momentum and energy equations. This is done via a series of expressions and user functions within CFX. Each of the locally calculated variables are represented as expressions, whereas the spatially dependent constants appear as user functions. Within the rotor domain, forces are expressed as both a general momentum source and energy source, whereas the stator requires only a general momentum source. CFX allows the user to express these forces in cylindrical components. The following transformation is used to convert the total force and energy to individual cylindrical components per unit volume:

$$F_{n,rotor} = \begin{bmatrix} F_{n,rotor,x} \\ F_{n,rotor,r} \\ F_{n,rotor,\theta} \end{bmatrix} = \rho f_{n,rotor} \begin{bmatrix} sin(\beta) \\ 0 \\ cos(\beta) \end{bmatrix} \tag{3.24}$$

$$F_{p,rotor} = \begin{bmatrix} F_{p,rotor,x} \\ F_{p,rotor,r} \\ F_{p,rotor,\theta} \end{bmatrix} = \frac{\rho f_{p,rotor}}{W_{rel}} \begin{bmatrix} -v_x \\ -v_r \\ -v_{\theta,rel} \end{bmatrix} \tag{3.25}$$

$$\dot{W}_{rotor} = \rho r \Omega (f_{n,rotor,\theta} + f_{p,rotor,\theta}) \tag{3.26}$$

$$F_{n,stator} = \begin{bmatrix} F_{n,stator,x} \\ F_{n,stator,r} \\ F_{n,stator,\theta} \end{bmatrix} = \rho f_{n,stator} \begin{bmatrix} sin(\alpha) \\ 0 \\ cos(\alpha) \end{bmatrix} \tag{3.27}$$

$$F_{p,stator} = \begin{bmatrix} F_{p,stator,x} \\ F_{p,stator,r} \\ F_{p,stator,\theta} \end{bmatrix} = \frac{\rho f_{p,stator}}{W} \begin{bmatrix} -v_x \\ -v_r \\ -v_\theta \end{bmatrix}. \tag{3.28}$$

Appendix A contains the CFX expressions for implementation of the volumetric source term model.

3.8 Volumetric Source Term Grid Independence Study

A series of five grids are tested, with increasing refinement in the axial, radial, and circumferential directions. The grid details are shown in Table 3.5. To achieve grid independence, it is desired to have the rotor work and isentropic efficiency reach a point of minimal change ($<0.5\%$) between grids. The actual change in rotor efficiency

and total temperature ratio between grids is given in Table 3.6. The grid results show that the efficiency is continually changing as grid density is refined. While the finest grid resolution provides the least amount of interpolation between cells and hence the greatest accuracy, there exists a tradeoff with computational cost. For this reason, a grid cell count of 279,760 is selected, corresponding to the second level of five grid densities. As the grid density increases, work input by the rotor changes at a rate that is acceptable ($<0.5\%$ in all cases). The efficiency however, is largely dependent on the grid discretization and subsequent interpolation of the parallel, viscous force. These traits are graphically shown in Figure 3-24. Therefore, any grid refinement requires an associated change in parallel force loss constants. It is deemed that all of the grids shown in Table 3.5 are acceptable. This assumption is made under the provision that the parallel force is tuned in accordance to the selected grid. Therefore, grid selection must first be determined, after which the parallel force is calculated for that specific grid.

Table 3.5: Volumetric source term grid independence study, grid details.

Grid	Cell Count	Spanwise Cells	Chordwise Cells	Circumferential Cells
	(per 1/16 annulus sector)		(per component)	(per degree)
1	187,440	40	50	0.71
2	279,760	60	50	0.71
3	609,500	80	60	0.89
4	1,115,125	100	75	1.11
5	1,953,300	120	85	1.33

Table 3.6: Volumetric source term grid independence study, rotor efficiency and total temperature ratio changes.

Grid	η_{rotor}	% difference	$T_{t,2}/T_{t,1}$	% difference
1	0.9084		1.1298	
2	0.9215	1.440	1.1300	0.154
3	0.9301	0.933	1.1302	0.154
4	0.9355	0.581	1.1305	0.230
5	0.9382	0.289	1.1306	0.077
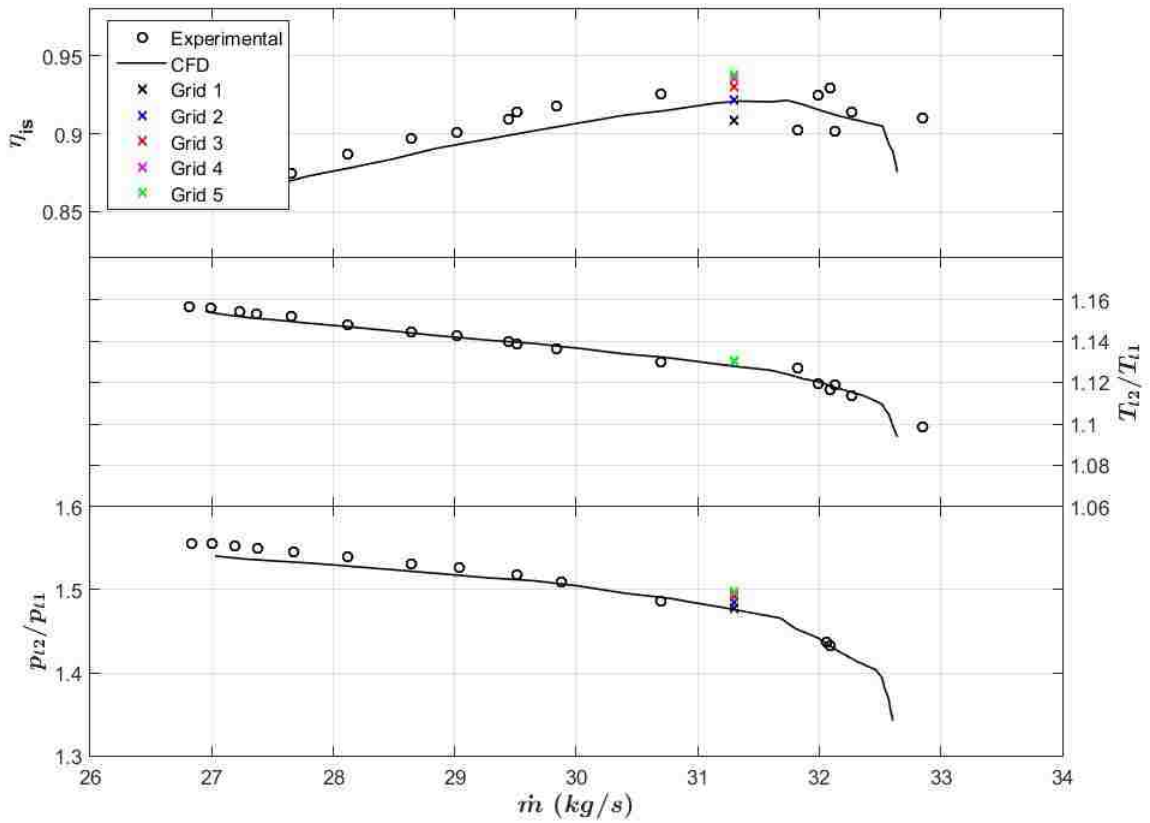
Figure 3-24: Volumetric source term rotor isentropic efficiency, total temperature ratio, and total pressure ratio for several grid densities.

3.9 Distortion Matrix Selection

Two practical types of distortions are of interest in this study: boundary layer inges-tion and turboprop propeller work profiles. In each case setup, the rotor flow coef-ficient (and hence mass-averaged inlet Mach number) is held constant. The method and reasoning behind this is firstly detailed.

3.9.1 Corrected Mass Flow Rate and Corrected Rotor Speed in the Presence of Inlet Distortion

In the presence of distortion, whether a total pressure or total temperature distortion, the inlet conditions must be corrected to compare against one another. Traditionally, an inlet-corrected mass flow rate and corrected rotor speed is used,

$$\dot{m}_{corr} = \dot{m} \frac{p_t}{p_{t,ref}} \frac{\sqrt{T_{t,ref}}}{\sqrt{T_t}} \tag{3.29}$$

$$\Omega_{corr} = \Omega \frac{\sqrt{T_{t,ref}}}{\sqrt{T_t}}, \tag{3.30}$$

where $T_{t,ref}$ and $p_{t,ref}$ are the reference total temperature and reference total pressure the flow is being corrected to. This method is applicable to varying conditions of uniform inflow, such as comparing engine operation at different altitudes. In this work, distortions only exists in a section of the inlet and vary spatially. Therefore, the order of operation in mass-weighted averaging is of importance. CFX computes the corrected mass flow as,

$$\dot{m}_{corr} = \dot{m} \frac{\overline{p_t}^M}{p_{t,ref}} \frac{\sqrt{T_{t,ref}}}{\sqrt{\overline{T_t}^M}}. \tag{3.31}$$

However, the desired function is not a multiplicity of the individual mass-weighted quantities, but rather a mass-weighted average of the entire function,

$$\dot{m}_{corr} = \dot{m} \overline{\frac{p_t}{p_{t,ref}} \frac{\sqrt{T_{t,ref}}}{\sqrt{T_t}}}^M . \tag{3.32}$$

As a consequence, the traditional method within CFX for calculating corrected mass flow rate is not used in this work. Additionally, with the complicated distortion geometry used in the radial distortion cases, the solution to Equation 3.32 is convoluted. Rather, two important variables can be conserved to ensure consistency between all cases: the corrected rotor speed, Ω_{corr} and flow coefficient, ϕ. The flow coefficient is defined [13],

$$\phi = \frac{\overline{v}_x^M}{U_{mid}} . \tag{3.33}$$

In the case of non-swirling flow, the flow coefficient has a one-to-one mapping to the relative rotor flow angle. By conserving these two dimensionless quantities, the physical mass flow rate which corresponds to the corrected mass flow rate is solved. This also ensures that that mass-averaged inlet Mach number, $\overline{M}_{inl}^M$, is conserved for non-swirling flows. For NASA stage 67 at 90% rotor speed, these values are shown in Table 3.7. These quantities can be be enforced within CFX, as an outlet mass flow rate, through use of a series of expressions combined with a Fortran routine. However, to reduce computational time in the full annulus calculation, a hard-coded outlet boundary condition is desired. Therefore, the physical mass flow is desired to be solved a priori.

Table 3.7: Non-dimensional flow characteristics conserved between test cases, NASA stage 67, calculated with uniform inflow, 90% speed, peak efficiency.

$\dot{m}_c$ (kg/s)	$\dot{m}$ (kg/s)	Ω (rad/s)	ϕ	$\overline{M}_{inl}^M$
31.1	31.1	1512	0.498	0.3944

To determine the correct boundary conditions, an additional CFD calculation is performed. A simplified computational mesh is developed - an extremely short duct

with the exact dimensions of the machine inlet. To produce this grid, the first four axial cells in the volumetric source term grid were extracted, keeping the radial and circumferential grid spacing unchanged. By creating a simplified grid with no external forces, the desired distortion pattern can be applied to the inlet and a converged solution can be found quickly. While running the calculation, the outlet mass flow rate is adjusted until the mass-averaged inlet Mach number is desired. Once a solution is reached, the resultant mass-averaged inlet axial velocity is used to solve for U_{mid} from Equation 3.33. The corresponding physical rotor speed is solved using,

$$\Omega = \frac{U_{mid}}{\Omega_{corr}r_{mid}}.$$ (3.34)

From this short duct calculation, the physical mass flow rate and physical rotor speed that yield the correct flow coefficient and corrected rotor speed is determined.

3.9.2 Boundary Layer Ingestion

In the case of boundary layer ingesting fans, the upstream boundary layer development results in a total pressure distortion at the engine inlet. This total pressure distortion is represented by a quadratic Mach number deficit in this thesis. Two separate profiles are considered: immersion-varying cases and depth-varying cases. The immersion of the distortion is expressed as,

$$\text{Immersion} = d/2R_{in},$$ (3.35)

where d is boundary layer thickness and R_{in} is the duct inlet radius. The depth of the distortion is expressed as,

$$\text{Depth} = \frac{M_{min}}{M_{\infty}},$$ (3.36)

where M_{min} is the Mach number at maximum distortion and M_∞ is the freestream, or undistorted, Mach number. A smaller value for depth represents a move severe distortion. Figure 3-25 represents a sample BLI inlet distortion profile, with 0.75 immersion and 0.25 depth. The 0.75 immersion means that 75% of the vertical span is subjected to the distorted Mach number, and 0.25 depth dictates that the minimum Mach number is 25% of the freestream Mach number.
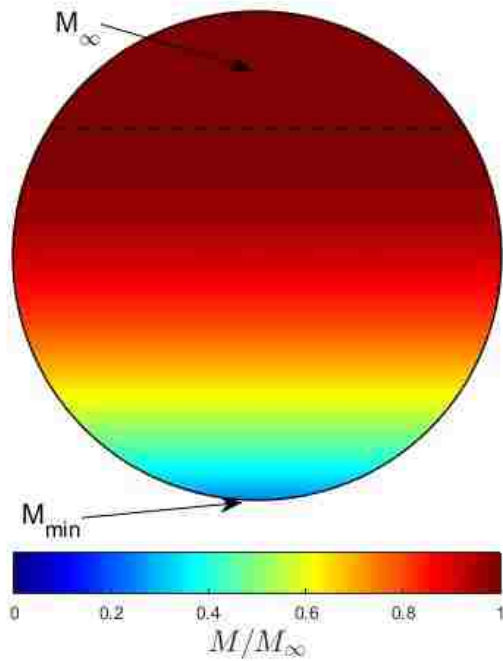
Figure 3-25: Sample BLI inlet Mach profile, 0.75 immersion and 0.25 depth.

A set of four immersion cases are tested, the immersion ranging from $d/2R_{in} = 0.25$ to $d/2R_{in} = 1.00$, each at a depth of $M_{min}/M_\infty = 0.50$ as shown in Figure 3-26. Further case characteristics are detailed in Table 3.8.

A set of three depth cases are also tested, the depth ranging from $M_{min}/M_\infty = 0.75$ to $M_{min}/M_\infty = 0.25$, each with an immersion of $d/2R_{in} = 0.50$ as shown in Figure 3-27. Further case characteristics are detailed in Table 3.9.
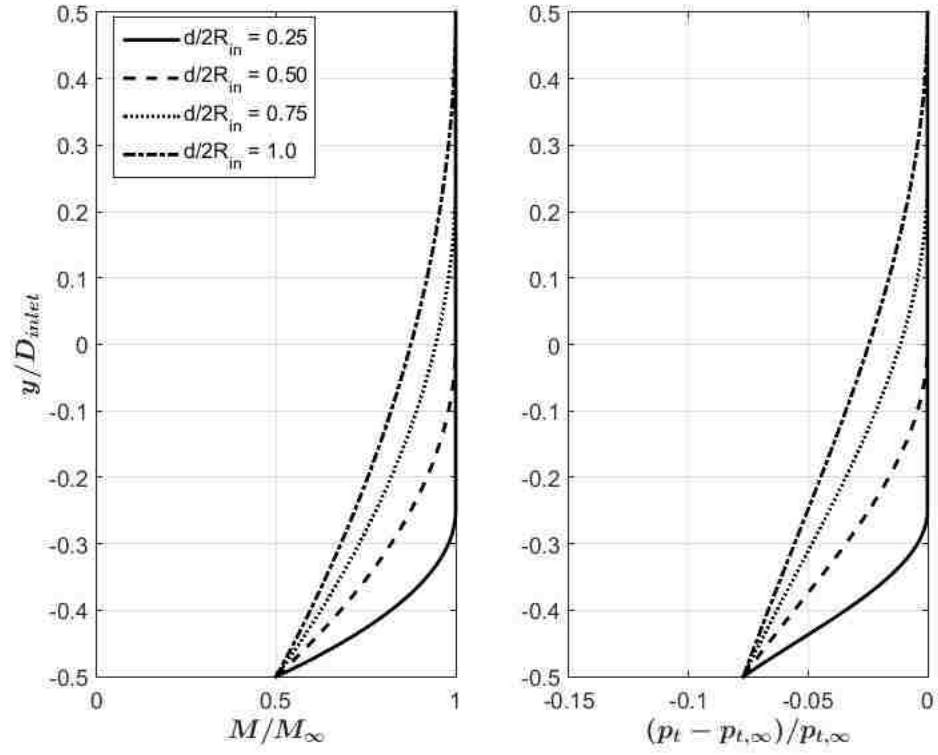
Figure 3-26: Rectilinear total pressure distortions; immersion-varying cases.

Table 3.8: Rectilinear total pressure distortions; immersion-varying cases.

Immersion	Depth	$\dot{m}$	Ω/Ω_{100}	ϕ	$\overline{M}_{inl}^{M}$
$d/2R_{in}$	M_{min}/M_∞	(kg/s)			
0.25	0.50	30.815	0.9		
0.50	0.50	30.350	0.9		
0.75	0.50	29.835	0.9	0.49801	0.3944
1.00	0.50	29.333	0.9		
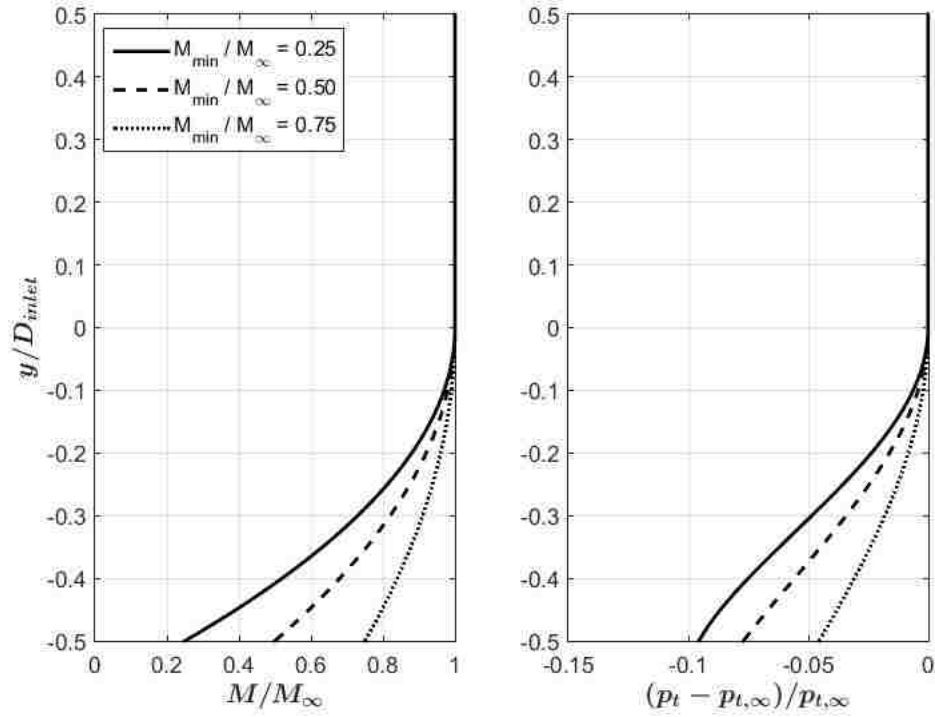
Figure 3-27: Rectilinear total pressure distortions; depth-varying cases.

Table 3.9: Rectilinear total pressure distortions; depth-varying cases.

Immersion	Depth	$\dot{m}$	Ω/Ω_{100}	ϕ	$\overline{M}_{inl}^{M}$
$\delta/2R_{in}$	M_{min}/M_∞	(kg/s)			
0.50	0.75	30.812	0.9		
0.50	0.50	30.350	0.9	0.49801	0.3944
0.50	0.25	29.696	0.9		

3.9.3 Turboprop Work Profile

A simplified work profile leaving the propeller of a turboprop engine is one class of distortion considered. Based on the work by Defoe and Hall [13], it was shown that swirling flow in to the engine has a highly non-linear scaling trend. Therefore, it is assumed that an inlet guide vane is ahead of the engine fan or first stage compressor,

eliminating incoming swirl. Additionally, a uniform work profile from root to tip of the propeller is not desirable in this thesis, as it does not produce a non-uniform compressor inflow. Rather, a linear variation of propeller work from the axis of rotation to propeller tip is used, based on a forced-vortex assumption, as shown in Figure 3-28.
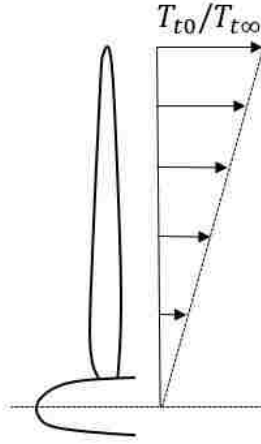
Figure 3-28: Linear profile of propeller exit total temperature ratio - propeller axis of rotation to blade tip.

Such a work profile is achieved by a spanwise-uniform exit flow angle combined with a spanwise-uniform inlet flow coefficient. The values used are based on the available specifications for the PW150 [32] turboprop engine. The specified flight speed for the Q400, using 2xPW150 engines is $179.44\ m/s$, or a flight Mach number of 0.625. Given that the propeller inlet area is $13.27\ m^2$, the corrected mass flow equation is used to solve the mass of air flowing through the propeller,

$$\frac{\dot{m}\sqrt{RT_t}}{Ap_t\sqrt{\gamma}} = \frac{M_x}{\left[1 + \left(\frac{\gamma-1}{2}\right)M_x^2\right]^{\frac{\gamma+1}{2(\gamma-1)}}}. \tag{3.37}$$

The provided propeller shaft horsepower for this turboprop machine, $5000\ hp$, is used to determine the change in total temperature from leading edge to trailing edge,

$$P = \dot{m}\Delta h_o, \tag{3.38}$$

$$\frac{T_{t2}}{T_{t1}} = 1 + \frac{\Delta h_o}{c_p T_{t1}}. \tag{3.39}$$

From this, the total temperature ratio for this propeller is calculated to be 1.0073, at mid-span. Linearly extrapolating this to the propeller tip, provides a ratio of 1.0146. The values tested in this thesis range from 1.04 to 1.12, providing a large safety factor in distortion severity.

Four distortion parameter variations are studied:

1. varying propeller rotational axis offset from the compressor rotational axis,

2. total temperature distortion, with varying intensity, at a constant axis offset,

3. total pressure distortion, with varying intensity, at a constant axis offset, and

4. a combination of the three previous distortions.

The first test case consists of shifting the propeller rotational axis offset from the compressor rotational axis, varying from $\Delta R/R = 0.00$ to $\Delta R/R = 3.00$. A sample of this distortion study ($\Delta R/R = 0.00$, $\Delta R/R = 0.50$, and $\Delta R/R = 1.00$) at the compressor inlet, station 0, is shown in Figure 3-29. The corresponding detailed flow characteristics for the entire study is shown in Table 3.10.
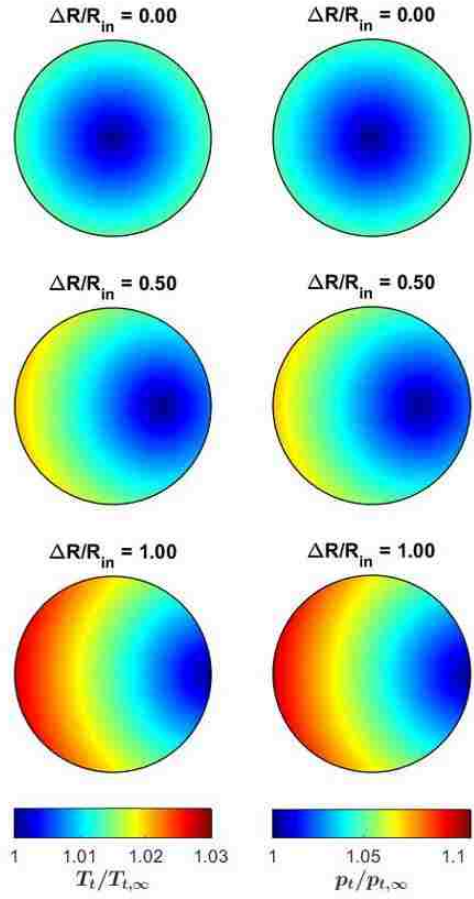
Figure 3-29: Radial distortions, three sample propeller offset distortion cases.

Table 3.10: Radial distortion detailed inlet parameters; offset cases.

Offset	Total Temperature	Total Pressure	$\dot{m}$	Ω/Ω_{100}	ϕ	$\overline{M}_{inl}^{M}$
$\Delta R/R_{in}$	$T_{t,prop,tip}/T_{t,\infty}$	$p_{t,prop,tip}/p_{t,\infty}$	(kg/s)			
0.00			31.9210	0.90445		
0.25			31.9308	0.90466		
0.50			31.9702	0.90531		
0.75	1.08	1.31	32.0680	0.90633	0.49801	0.3944
1.00			32.2687	0.90763		
1.50			32.8784	0.91061		
3.00			34.9907	0.92008		

To observe the effect of a radial total temperature profile, the total temperature ratio, measured at the propeller tip, is tested at three values, 1.04, 1.08, and 1.12. In each case the propeller offset is $\Delta R/R = 0.75$. The resultant distortion patterns are shown in Figure 3-30 and corresponding detailed flow characteristics in Table 3.11.
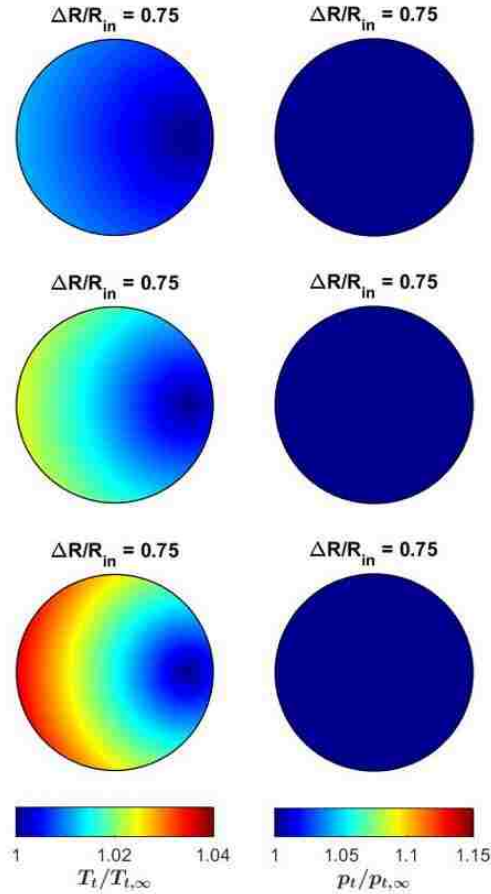
Figure 3-30: Radial distortions; total temperature cases.

Table 3.11: Radial distortion detailed inlet parameters; total temperature cases.

Offset	Total Temperature	Total Pressure	$\dot{m}$	Ω/Ω_{100}	ϕ	$\overline{M}_{inl}^{M}$
$\Delta R/R_{in}$	$T_{t,prop,tip}/T_{t,\infty}$	$p_{t,prop,tip}/p_{t,\infty}$	(kg/s)			
	1.04		30.9922	0.90309		
0.75	1.08	1.00	30.8871	0.90616	0.49801	0.3944
	1.12		30.7833	0.90922		

68

To observe the effect of a radial total pressure profile, the total pressure ratio, measured at the propeller tip, is tested at three values, 1.15, 1.31, and 1.49. In each case the propeller offset is $\Delta R/R = 0.75$. These values are determined from an isentropic relationship between total temperature and total pressure, corresponding to the values in the total temperature study,

$$\left(\frac{p_{t2}}{p_{t1}}\right) = \left(\frac{T_{t2}}{T_{t1}}\right)^{\left(\frac{\gamma}{\gamma-1}\right)}. \qquad (3.40)$$

The resultant distortion patterns are shown in Figure 3-31 and corresponding detailed flow characteristics in Table 3.12.
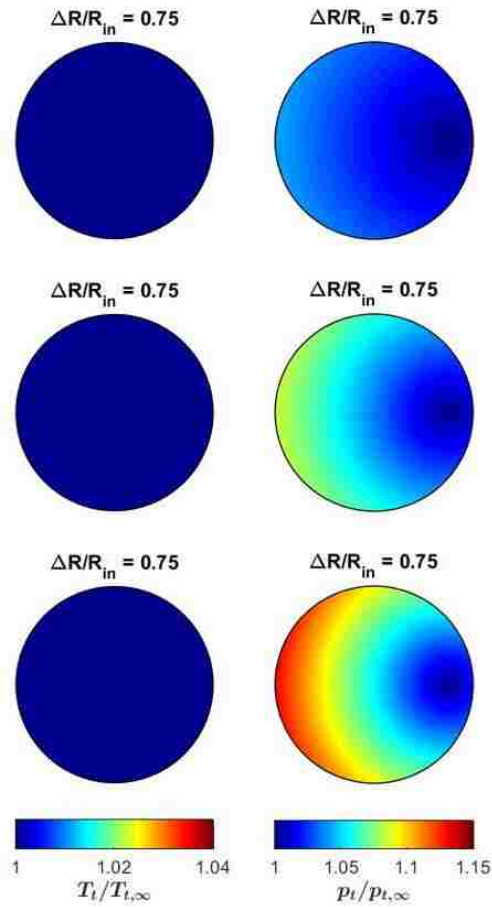
Figure 3-31: Radial distortions; total pressure cases.

69

Table 3.12: Radial distortion detailed inlet parameters; total pressure cases.

Offset	Total Temperature	Total Pressure	$\dot{m}$	Ω/Ω_{100}	ϕ	$\overline{M}_{inl}^{M}$
$\Delta R/R_{in}$	$T_{t,prop,tip}/T_{t,\infty}$	$p_{t,prop,tip}/p_{t,\infty}$	(kg/s)			
		1.15	31.7752	0.9		
0.75	1.00	1.31	32.2913	0.9	0.49801	0.3944
		1.49	32.5905	0.9		

Combinations of the three previous distortions is studied: offset, total temperature, and total pressure distortion. At an offset of $\Delta R/R = 0.75$, the total temperature propeller tip ratio is tested at 1.04, 1.08, and 1.12, as well as the corresponding total pressure propeller tip ratio, 1.15, 1.31, and 1.49. The resultant distortion patterns are shown in Figure 3-32 and corresponding detailed flow characteristics in Table 3.13.
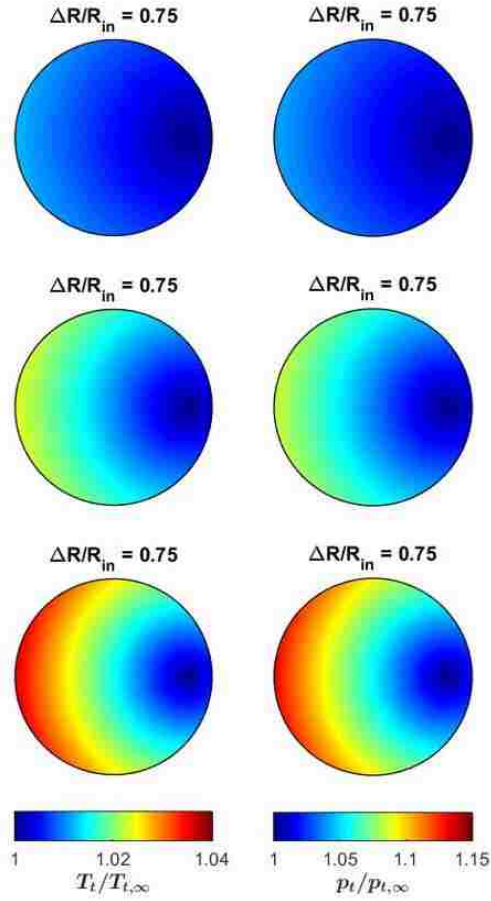
Figure 3-32: Radial distortions; combined total temperature and total pressure cases.

Table 3.13: Radial distortions; combined total temperature and total pressure cases.

Offset	Total Temperature	Total Pressure	$\dot{m}$	Ω/Ω_{100}	ϕ	$\overline{M}_{inl}^{M}$
$\Delta R/R_{in}$	$T_{t,prop,tip}/T_{t,\infty}$	$p_{t,prop,tip}/p_{t,\infty}$	(kg/s)			
	1.04	1.15	31.6657	0.90313		
0.75	1.08	1.31	32.0680	0.90633	0.49801	0.3944
	1.12	1.49	32.2510	0.90962		

Chapter 4

Volumetric Source Term Model Assessment

In this chapter, the resultant VSTM performance is assessed against uniform inflow single passage results as well as non-uniform inflow experimental and CFD results published by Fidalgo et al. [11].

4.1   Assessment of the VSTM in Uniform Inflow

To evaluate the VSTM accuracy, a comparison is made against the uniform inflow single passage RANS calculation. At peak-efficiency mass flow rate, 31.1 kg/s, the key characteristics are shown in Table 4.1. The rotor isentropic efficiency of the VSTM is correct to within 0.03%. This degree of accuracy is expected, as the VSTM loss model is calibrated using the single passage isentropic efficiency. In the stator, the loss coefficient is designed to replicate the entropy-based loss coefficient. There is a reduced accuracy of this loss coefficient, at 3.37% error, due to the VSTM design methodology. Firstly, an emphasis is placed on rotor isentropic efficiency, over stator loss coefficient. This is because the impact of the rotor on flow redistribution mechanics is greater than the impact of the stator. Secondly, the flow coupling between

the rotor and stator makes it difficult to adjust both the rotor and stator loss co-efficients simultaneously. For this reason, the rotor loss accuracy, at peak-efficiency, is more accurate than the stator loss coefficient. Future work will see an automated optimization scheme developed for the process of tuning the loss model, which will serve to increase the accuracy of all loss coefficients.

Table 4.1: Uniform inflow VSTM versus single passage RANS at peak efficiency.

	single passage	VSTM	% error
$\dot{m}_{corr}$ (kg/s)	31.1	31.1	
FPR (rotor)	1.48	1.49	1.43
η_{is} (rotor, %)	92.45	92.42	0.03
ζ (stator)	0.143	0.148	3.37

For a VSTM to accurately capture the effects of an inlet distortion, off-design performance must also match the physical machine. To assess this capability, rotor total temperature, total pressure, and isentropic efficiency is plotted at various mass flow rates in Figure 4-1. The isentropic efficiency is well matched at mass flow rates both below and above design condition, even out performing Fidalgo et al. bladed CFD results [11] at mass flow rates below peak efficiency. At mass flow rates near choke conditions, the VSTM is unable to capture the drop off in rotor work. This is expected, as blockage is not modelled, therefore choking effects are significantly delayed. This is not consequential, however, as no local flow region in any of the distortion studies approach choking flow rates. The total pressure ratio trend is also well predicted at all mass flow rates, aside from choke conditions, again attributed to the absence of blockage modelling. There is a shift in total pressure above the previously published results, an overestimation of 1.9% to 4.1% (versus Fidalgo et al. CFD [11]) . This overestimation does not have in impact on the non-uniform inflow study. The study is not machine specific, therefore the magnitude of total pressure is

not significant, rather the total pressure characteristic shape is of importance. It is determined that the off-design performance of the VSTM is representative of a first stage compressor and valid for use in a inflow distortion study.
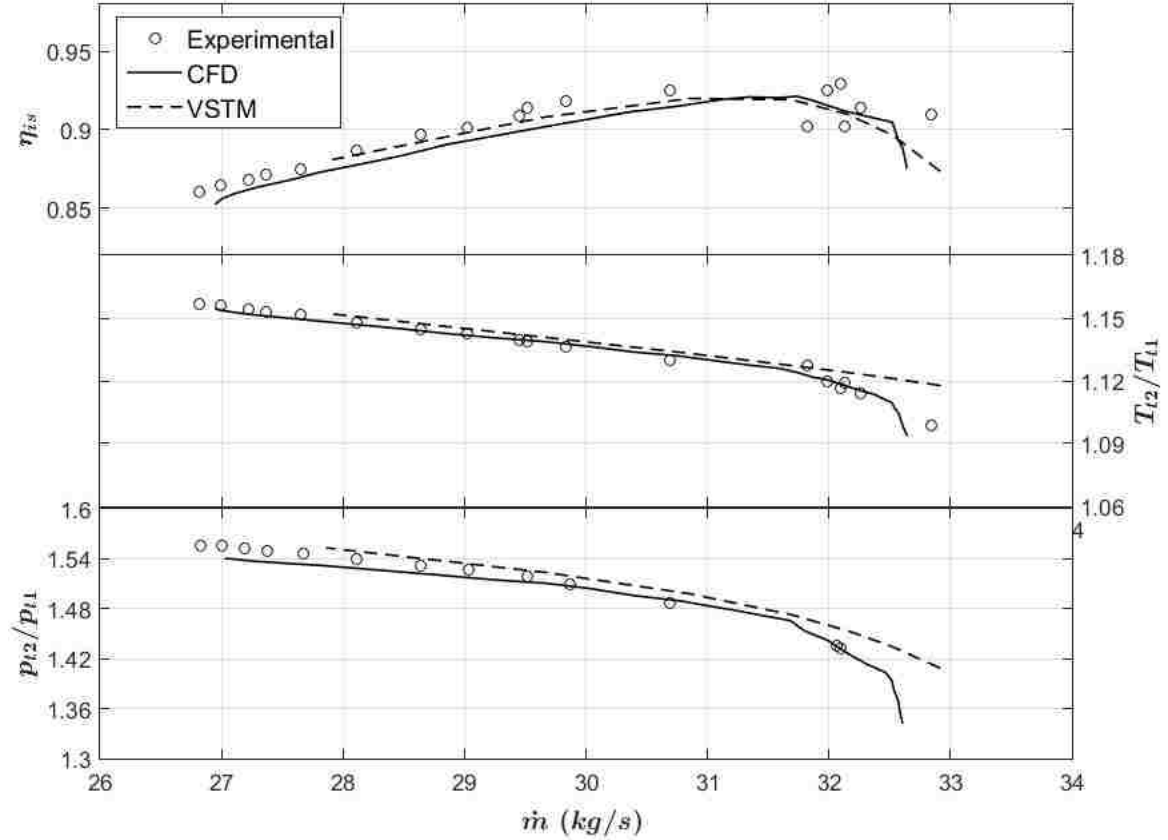
Figure 4-1: Rotor total temperature, total pressure, and isentropic efficiency at off-design conditions.

4.2   Assessment of VSTM in Non-Uniform Inflow

Of importance in this work is the VTSM accuracy in response to non-uniform inlet distortions. To assess the VSTM performance, the inlet distortion study performed by Fidalgo et al., discussed in section 2.2, represents a benchmark test to compare against. The full annulus, unsteady CFD results of their study was shown to accurately capture the experimental results performed on the same case setup [11]. The distortion itself is a 120 degree total pressure deficit region, at an operating speed of

90% of the design rotational speed, and the inlet-corrected mass flow rate based on mass-averaged, stagnation quantities, is 32 kg/s. Additionally, the distortion characteristic, DC_{120} is 83%. Since the distortion characteristic is calculated post priori, it is not of assistance in setting boundary conditions to match flow conditions. The midspan total pressure used by Fidalgo et al., in addition to the volumetric source term model (VSTM) is shown in Figure 4-2. The station location is far enough stream that minimal mixing between the distorted and undistorted regions has taken place. The minimum value of total pressure from this graphic is used to set up the VSTM calculation of the same distortion. The difficulty in this is that the exact value is unknown, however a best estimate is found through the use of plot digitization, $0.893p_{t0,clean}$. The resultant distortion, which covers 1/3 of the entire inlet domain, is highly sensitive to the value of $p_{t0,min}/p_{t0,clean}$ selected. The difference in total pressure profiles suggest that the total pressure distortion used in the VSTM is not consistent with the setup used by Fidalgo et al.. The corrected mass flow rate is dependent on this distortion, thus the magnitude of results in this study are incorrect and only qualitative trends can be observed.

Due to the discrepancy in inlet distortions between the VSTM and previously published CFD results, it is expected that the different physical mass flows will result in different rotor work. This is demonstrated in Figure 4-3, a plot of the mass flux at 0.5 and 5.5 axial chords upstream of the rotor leading edge. In the VSTM, the far upstream mass flux is greater than in the Fidalgo et al. CFD calculation. As a result, the rotor work is greater on the slower moving CFD case, and the difference between the cases is attenuated as the flow moves closer to the rotor, especially in the undistorted region. The mass flux redistribution is qualitatively similar between the two cases, as the regions distorted regions of counter-swirl are sucked harder than the regions of co-swirl, as expected. While there is a level of mass flux redistribution upstream of the compressor, $(\rho u_{x,max}/\rho u_{x,min})_{5.5} = 0.5577$ and $(\rho u_{x,max}/\rho u_{x,min})_{5.5} =$

0.6578, there is still a significant distortion ingested to the rotor.
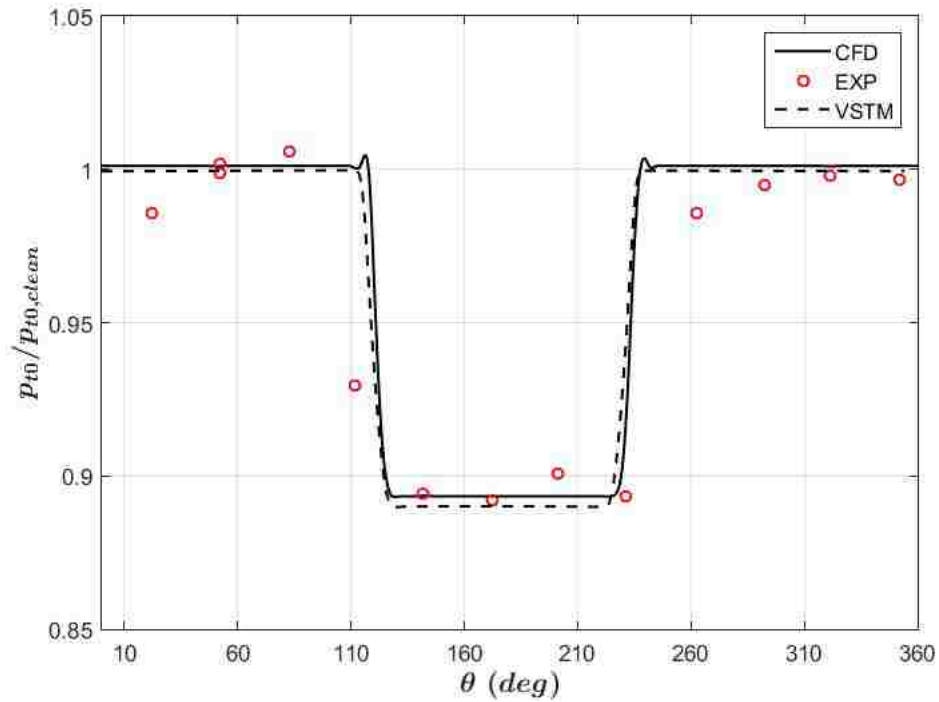
Figure 4-2: Far upstream circumferential traverse of total pressure at midspan, published in the work by Fidalgo et al. [11].

The effect of mismatched inlet conditions is further shown in Figure 4-4, a plot of the upstream whirl angle between the VSTM and Fidalgo et al. CFD. Here it is shown that at far upstream locations, where the rotor influence is minimal, the whirl angle is incorrect, due to a higher mass flow in the VSTM case. While the induced swirl angles are very similar, the axial velocity difference leads to different absolute flow angles. As the flow approaches the rotor, the regions of co-swirl and counter-swirl have reduced magnitudes due to a combination of two factors: reduced rotor work and increased axial velocity. For the remainder of the analysis between the two cases, a qualitative approach is enlisted, as a quantitative mismatch is expected.

Figure 4-3: Circumferential traverses of mass flux at midspan locations 0.5 and 5.5 axial chords upstream of the rotor leading edge.

Despite the mismatched inlet conditions, the rotor outlet characteristics are similar to the results from Fidalgo et al. The rotor work and trailing edge absolute whirl angle of the VSTM are well matched, as shown in Figure 4-5, a plot of three key variables at midspan. In particular, the rotor work and flow angle follows the CFD trendline near perfectly, while the total pressure has a wider margin of error. This is attributed to two factors. Firstly, the rotor work is dependent almost solely on the accuracy of the normal force model, while the pressure rise is dependent on the accuracy of both the normal and parallel forces, leading to a reduction in accuracy. Secondly, Fidalgo et al. published two different values for rotor isentropic efficiency at design flow coefficient, 92.4% and 93.5% [11]. The rotor parallel force model is based off the lower isentropic efficiency, thus it is reasonable to assume that the total pressure at rotor exit will be under-predicted, as shown here, if the incorrect rotor efficiency was published.
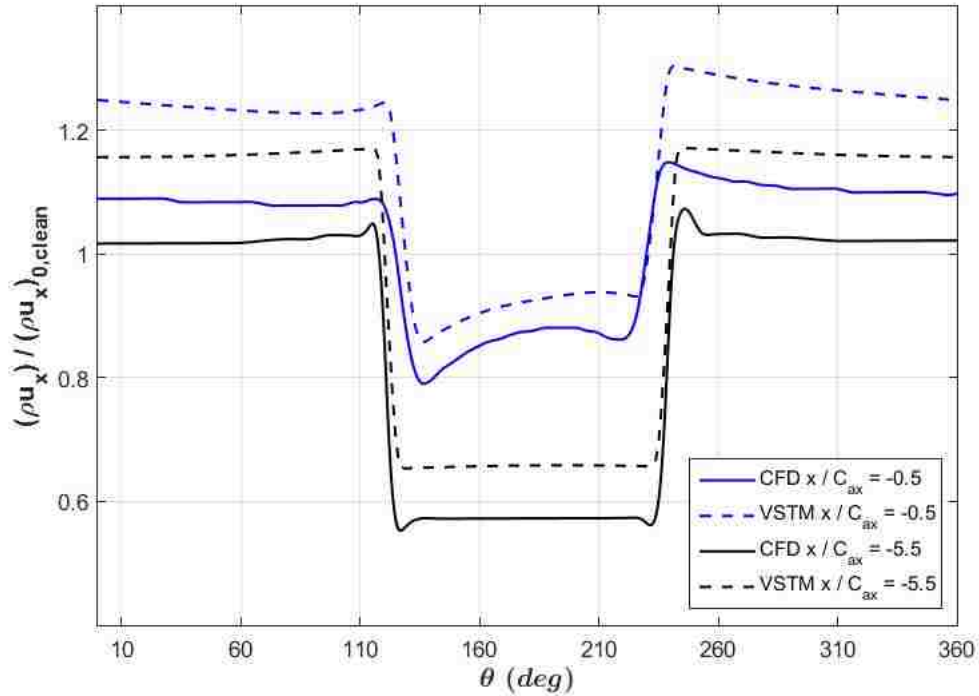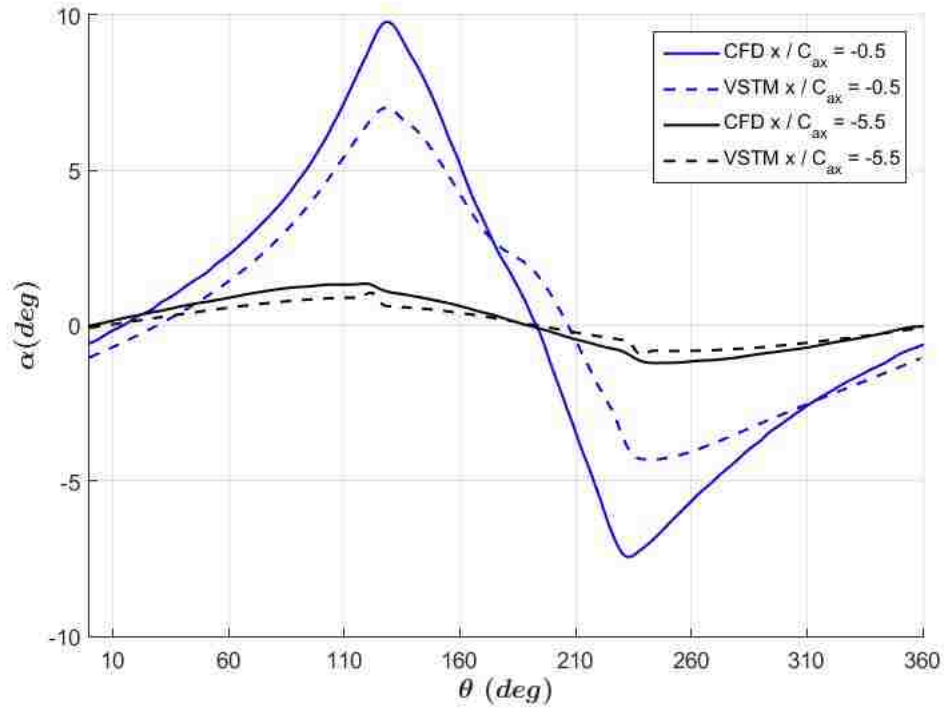
Figure 4-4: Circumferential traverses of absolute whirl angle at midspan locations 0.5 and 5.5 axial chords upstream of the rotor leading edge.

In addition to a well-matched circumferential flow characteristics, the VSTM also captures radial flow profiles accurately. As shown in Figure 4-6, the total pressure, total temperature, and absolute whirl angles are well matched at a circumferential coordinate location of 73 degrees, a spanwise location just outside of the distortion region. Two notable exceptions are in the VSTM near the hub and tip. Within the VSTM tip, the losses are poorly captured due to the absence of a physical tip gap. Additionally, near both the hub and tip, the flow angles are under-predicted, due to the use of slip-walls. For this reason, the end wall flow features are poorly predicted.

Figure 4-5: Midspan circumferential traverse of absolute whirl angle, total temperature, and total pressure at the rotor TE.

For the purpose of an efficiency scaling study, the end-wall flows and absolute values of isentropic efficiency and fan pressure ratio are less important than the change in these values, from clean inflow to distorted inflow. These results are shown in Table 4.2. To three significant digits, the rotor total pressure ratio is unchanged in both results, and the rotor efficiency change is correct within 2.7%.
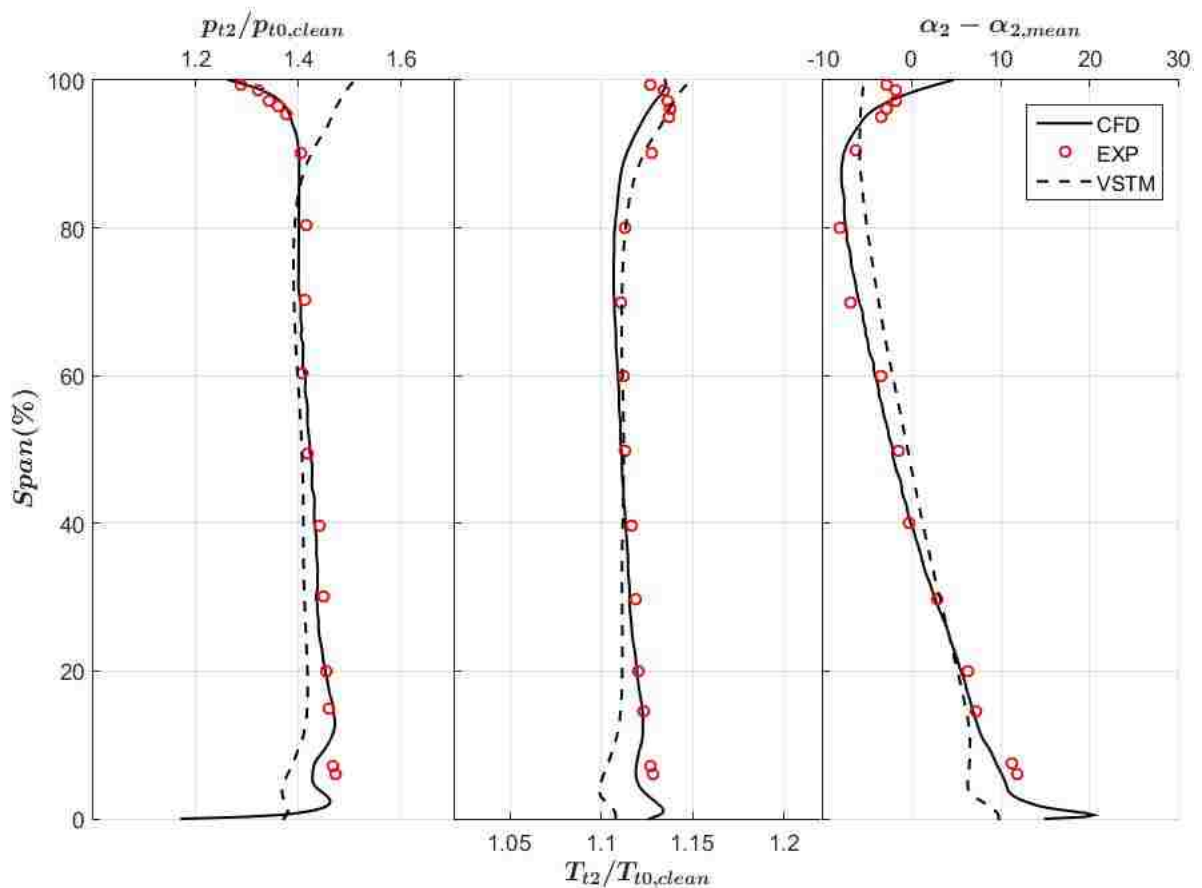
Figure 4-6: Spanwise profiles of total pressure, total temperature, and absolute whirl angle at the rotor TE, $\theta = 73°$.

Table 4.2: Summary of results at 90% rotor speed and 32 kg/s, from Fidalgo et al. CFD [11] vs VSTM.

	CFD (clean)	CFD (distorted)	VSTM (clean)	VSTM (distorted)
FPR (rotor)	1.46	1.46	1.45	1.45
η_{is} (%, rotor)	93.5	92.0	91.87	90.41
$\Delta\eta_{is}$ (%,rotor)		-1.50		-1.46

Within the stator blade passage, the qualitative flow response to the distortion excellently captures the results by Fidalgo et al. [11]. Midspan circumferential traverses of important flow characteristics, downstream of the stator are shown in Figure

80

4-7. The plot of absolute whirl angle demonstrates one key element of the VSTM, the absence of trailing edge blade wakes. While the mean value of flow angle is well predicted, the unsteady, bladed CFD calculation by Fidalgo et al. exhibits the trailing edge blade wakes. The total temperature is well predicted, as there is no work or energy lost within the stator, meaning the rotor work profile is transferred to the stator blade. The total pressure profile at stator exit is nearly identical to the rotor exit, aside from a vertical shift down, due to stator losses. Circumferential flow redistribution within the stator blade is minimal as illustrated by the similarity between rotor exit flow properties and stator exit flow properties.
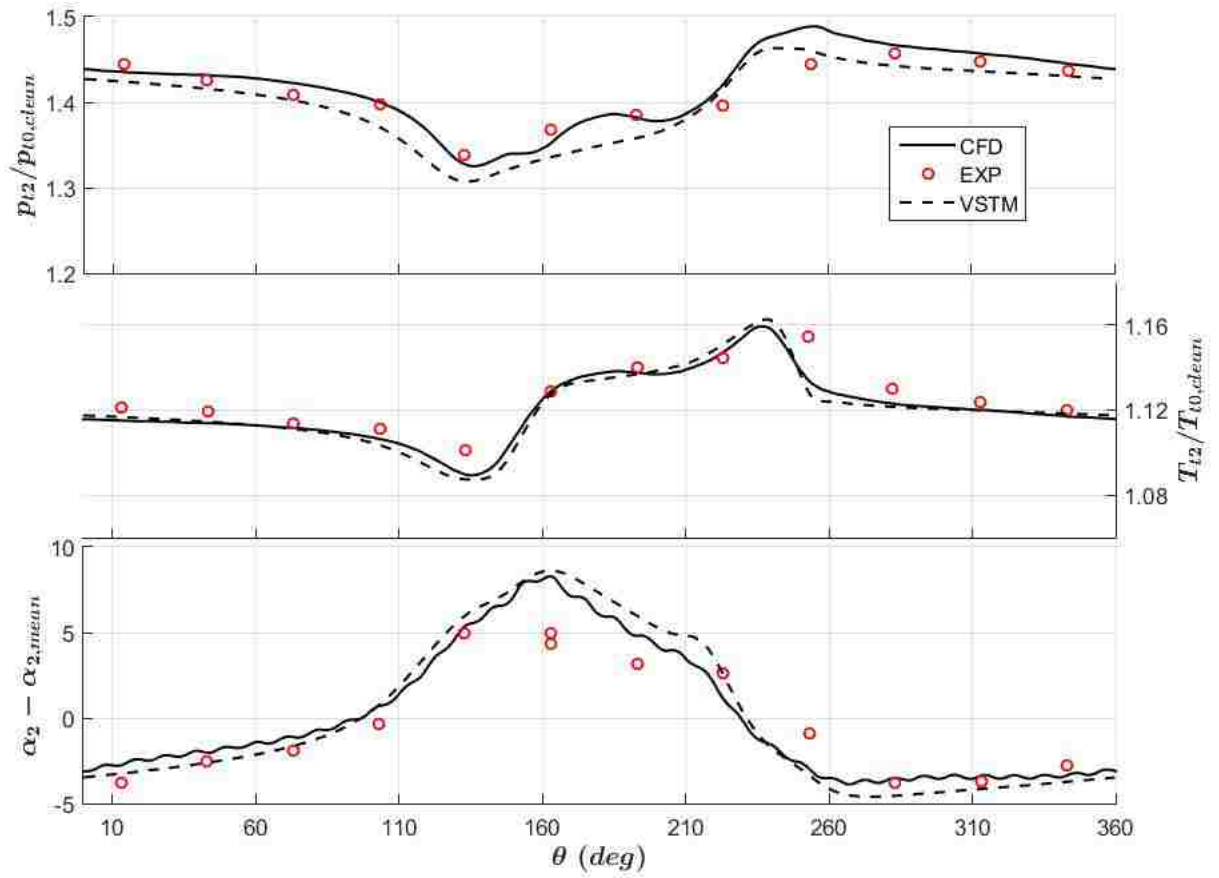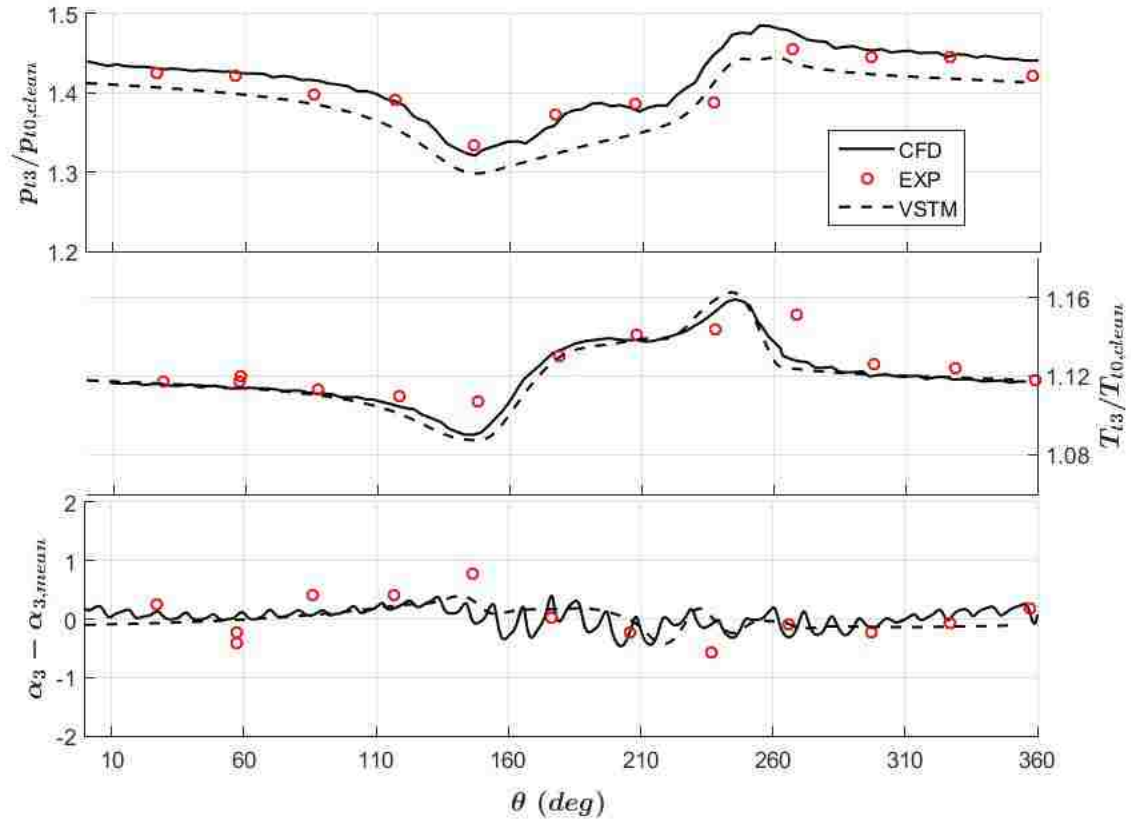

Figure 4-7: Midspan circumferential traverses of absolute whirl angle, total temperature, and total pressure at the stator trailing edge.

The results presented in this chapter show an excellent response by the VSTM to both uniform and non-uniform inflow. The change in overall rotor efficiency from

clean to non-uniform inflow compared to Fidalgo et al. URANS results is predicted within 2.7%. Given that this is the steady calculation of an unsteady effect, this degree of accuracy drives home the effectiveness of a VSTM representation of a single stage compressor and the associated reduced computational requirements.

Chapter 5

Non-Uniform Inflow Efficiency Scaling

In this chapter, the limitations of the volumetric source term model are discussed, in addition to the efficiency scaling results of the distortion matrix.

5.1 Limitations of the VSTM Parallel Force

The parallel force model in this work is dependent on two variables, the mass-averaged inlet relative Mach number and local relative velocity. This model was shown in Chapter 4 to be able to accurately capture viscous losses in uniform inflow at both design and off-design conditions. In the parallel force formulation, a single value for $\overline{M}_{rel}^{M}$ is calculated and applied at all spatial locations within the domain. This value is calculated just upstream of the blade domain inlet. Within the blade domain, the local loss force is dependent only on $\overline{M}_{rel}^{M}$ and the local relative velocity. This method for calculating the parallel force is illustrated in Figure 5-1. In non-uniform inflow, a limitation of this model arises: the loss force is unable to capture local parallel force changes due to deviation from the design flow coefficient.
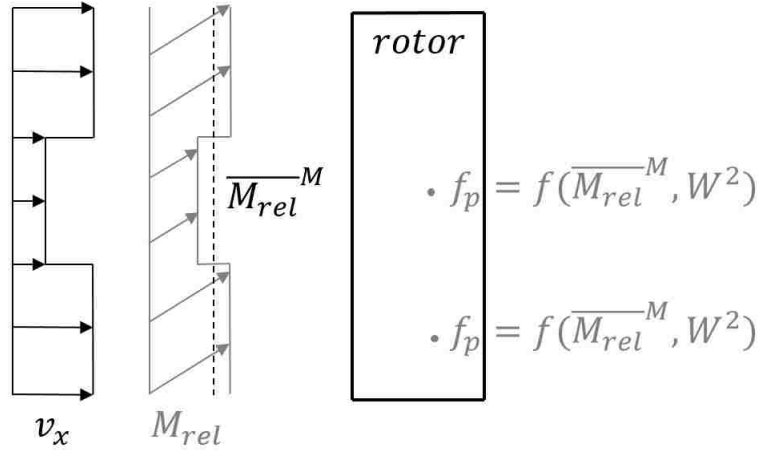
Figure 5-1: Rotor domain, unwrapped circumferential sketch of the current parallel force implementation.

In a physical compressor, the loss force has a "bucket"-like behaviour. At each spanwise and chordwise location along the blade, deviations from the design flow coefficient work to increase the local loss force quadratically. In the loss force model used in the work, this behaviour is not captured. This phenomena is sketched in Figure 5-2, where the quadratic dependence on local velocity alone creates a loss profile inconsistent with the expected loss bucket.
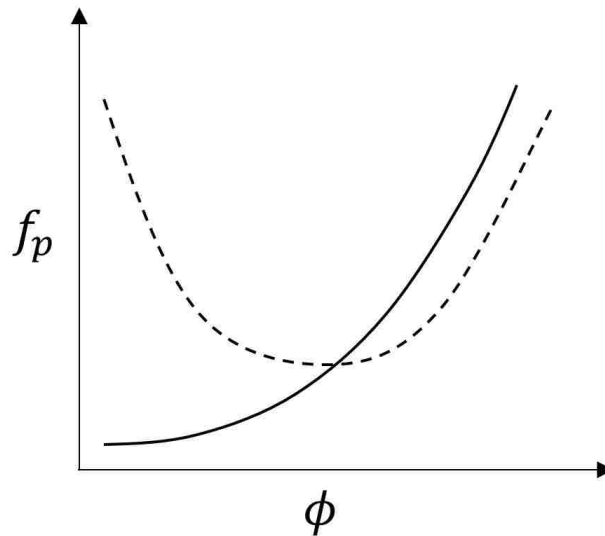
Figure 5-2: A sketch of the expected "loss bucket" (dashed line) vs the loss profile in this work (solid line).

This loss force deficiency is apparent in the non-uniform inflow cases studied in this thesis. Figures 5-3 to 5-6 contain rotor mass flux, relative flow angle, diffusion factor, and loss coefficient. Each of these plots are at 90% span circumferential traverses for a BLI distortion with 50% immersion. The mass flux profile illustrates the extent of non-uniformity ingested by the rotor domain. This mass flux deficit, or flow coefficient deficit, also leads to an increased relative incidence angle entering the engine. Increases in relative incidence angle have an associated increase in blade loading, and thus increased boundary layer development along the blade and associated flow losses. This flow feature is captured as increases in relative flow angle, compared to clean inflow, leads to an increase in diffusion factor. The loss coefficient behaviour, however, is not as expected. Due to the parallel model's local dependence on relative velocity, the loss coefficient changes very closely resemble mass flux changes. In other words, distorted flow regions of reduced axial velocity directly lead to a reduced local loss force, such that it dominates the losses from increased boundary layer development. A more accurate loss model should produce a correlation between diffusion factor and loss coefficient.
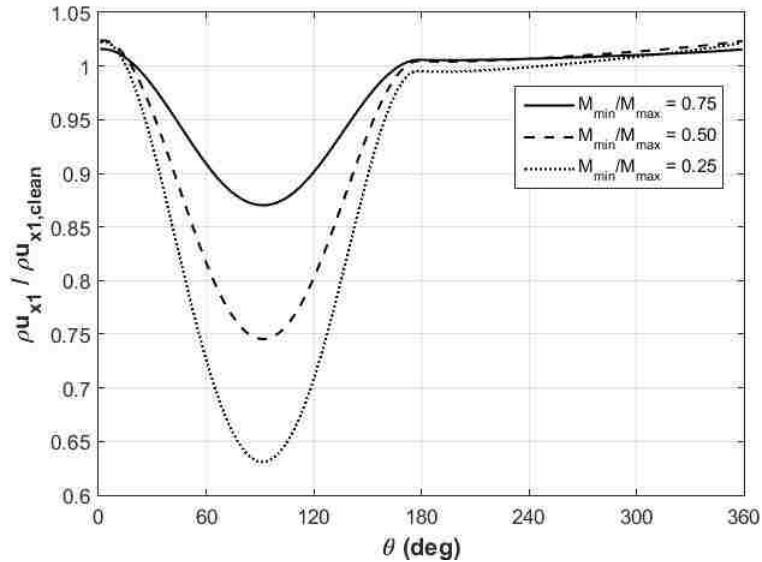
Figure 5-3: Rotor incoming mass flux (right) at 90% span, BLI 50% immersion.

Figure 5-4: Rotor incoming relative flow angle at 90% span, BLI 50% immersion.

Figure 5-5: Rotor diffusion factor at 90% span, BLI 50% immersion.
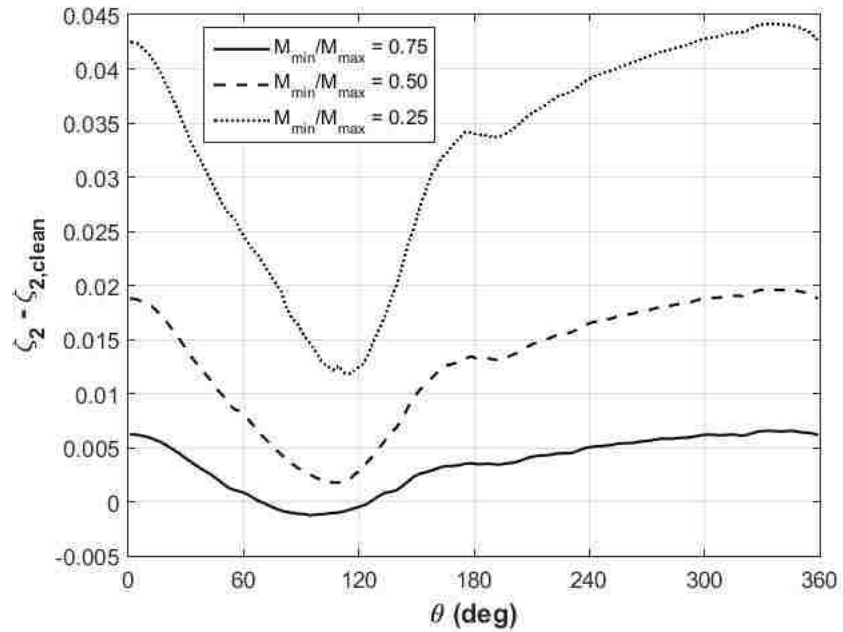
Figure 5-6: Rotor entropy-based loss coefficient at 90% span, BLI 50% immersion.

Pertinent information in the stator domain is shown in Figures 5-7 to 5-10. Within the stator domain, the incoming flow distortion has been further attenuated by the rotor. The maximum mass flux deficit is 15.7%, compared to a maximum rotor mass flux deficit of 37.1%. Due to a change in reference frame, the incidence angle change from design is actually larger in the stator than in the rotor (10.7° to 7.3°). This reduction in mass flux distortion, combined with an increased incidence angle distortion and lower relative velocity within the stator leads to diffusion loss effects being dominant. For this reason, there is a correlation between diffusion factor and loss coefficient in the stator, despite the incorrect formulation of the parallel force in non-uniform flow.
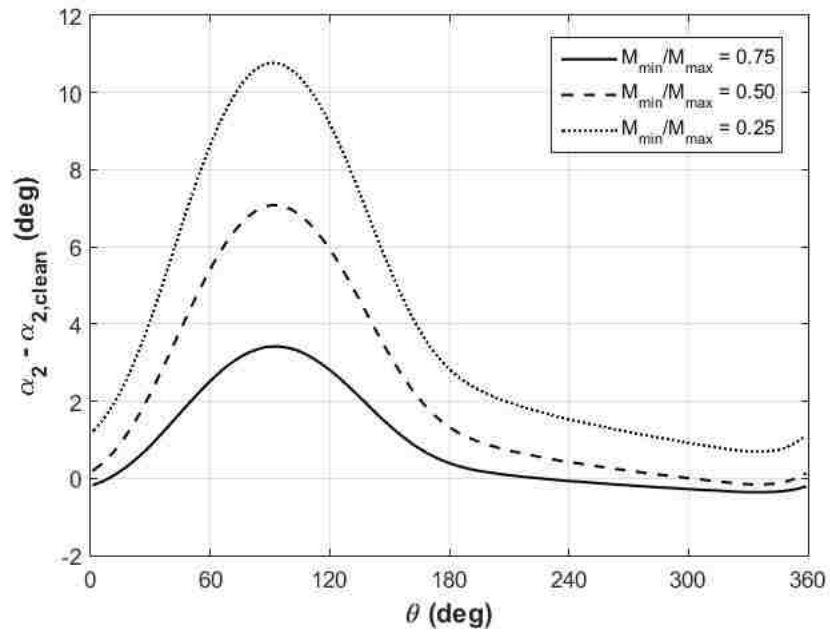
Figure 5-7: Stator incoming flow angle at 90% span, BLI 50% immersion.
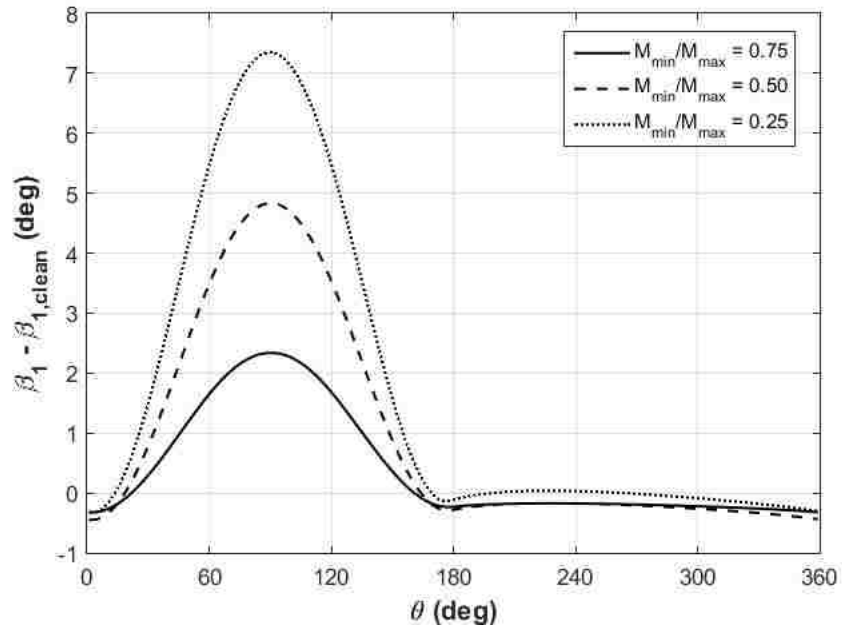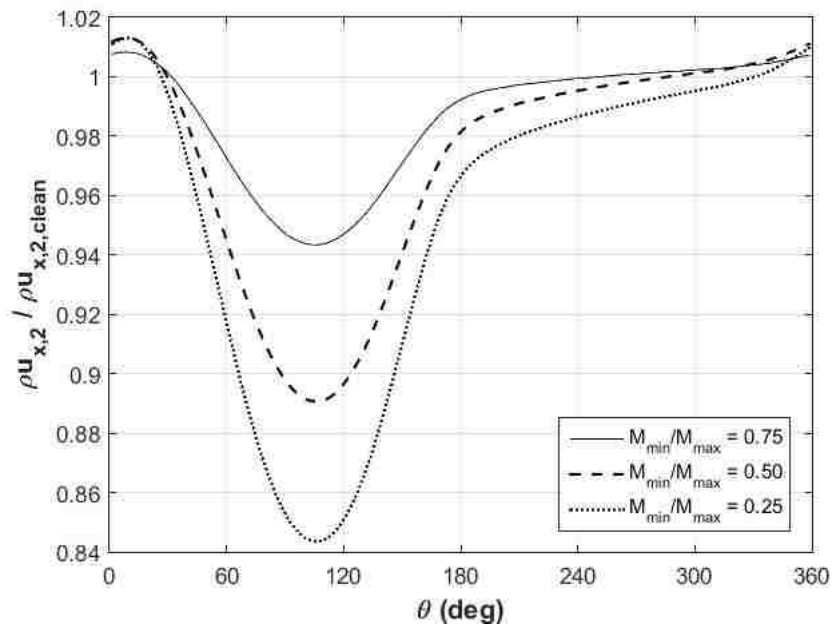

Figure 5-8: Stator incoming mass flux at 90% span, BLI 50% immersion.
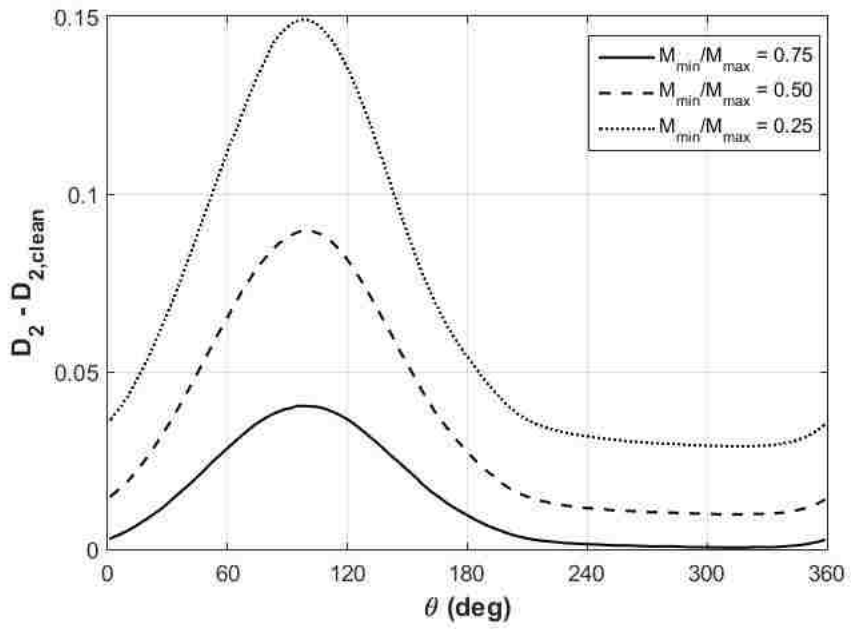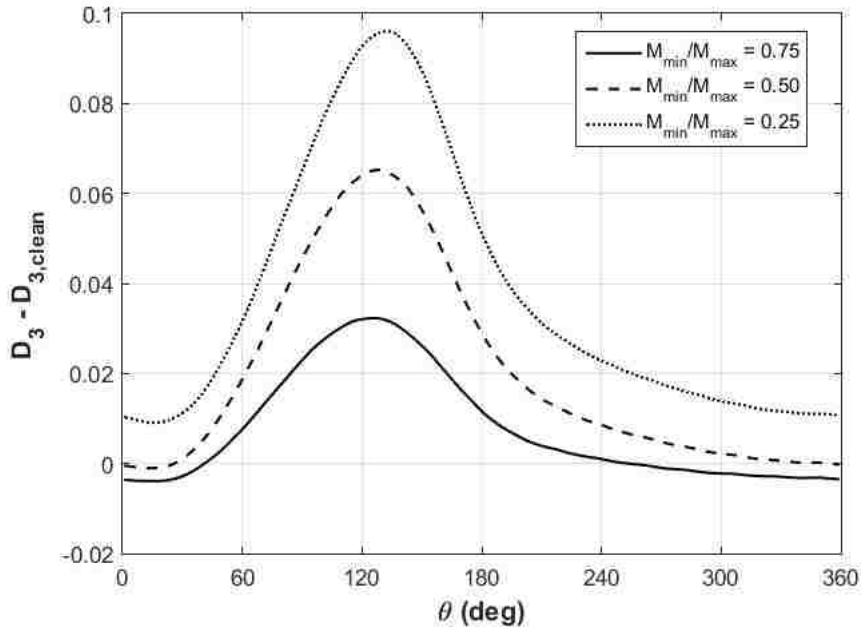
Figure 5-9: Stator diffusion factor at 90% span, BLI 50% immersion.
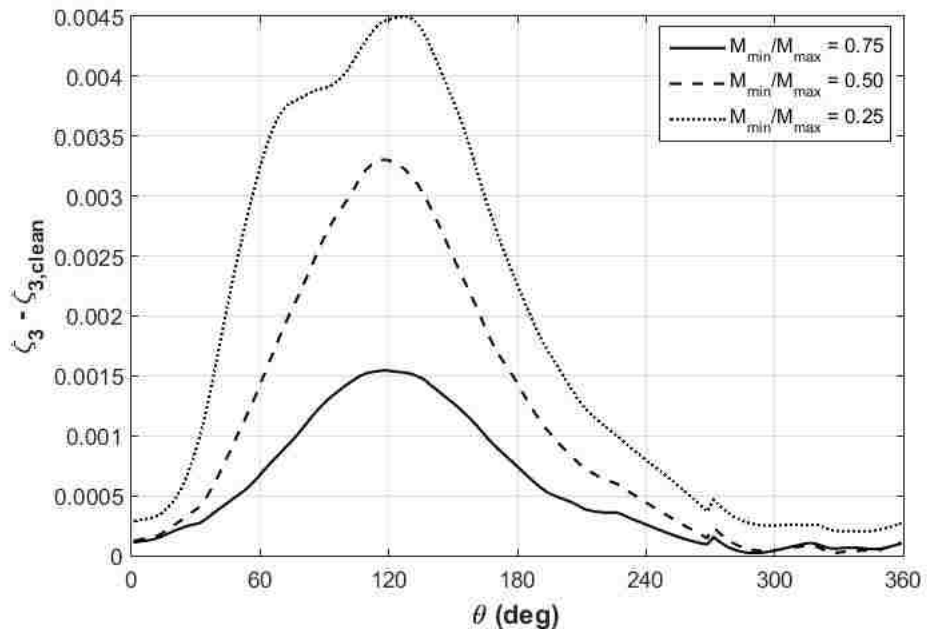
Figure 5-10: Stator loss coefficient at 90% span, BLI 50% immersion.

In future work, to overcome this limitation, a spatial dependence on flow coefficient is to be implemented. A schematic of this revised parallel force method is shown in Figure 5-11. This implementation allows for the parallel force to respond to incoming

flow distortions; at each radial and circumferential location the blade exhibits the properties of a blade efficiency characteristic. To accomplish this, the design flow coefficient at each radial location for uniform inflow needs to be calculated a priori. From this, an efficiency characteristic is developed at each radial location and finally, the loss coefficient along a streamline becomes dependent on the streamline inlet flow coefficient.

Due to the limitation of the parallel force model used in this thesis, the distortion matrix results focus on upstream flow redistribution and rotor diffusion as opposed to changes in isentropic efficiency and loss coefficient across blade domains.
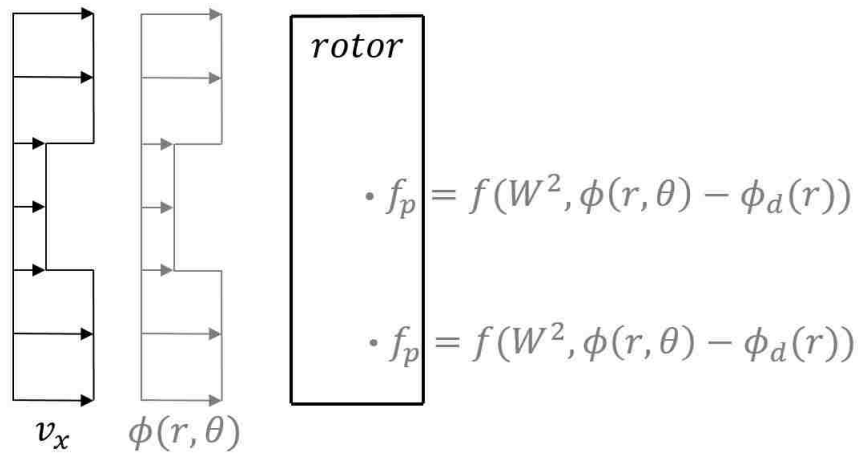
Figure 5-11: Future parallel force implementation; local force magnitude is circumferentially and radially dependent on flow coefficient as well as local velocity squared.

5.2 Performance Scaling in BLI Distortions

In depth-varying BLI distortion cases, the upstream mass flux redistribution and change in relative flow angle exhibits a linear scaling trend. This observation is consistent with the results of a low-speed fan study performed by Defoe and Hall [13]. In Figure 5-12 this phenomena is observed at station 1 (stations previously detailed in Figure 3-12) as the mass flux deficit for a distortion depth of $M_{min}/M_{max} = 0.25$ is predicted by the addition of distortions $M_{min}/M_{max} = 0.50$ and $M_{min}/M_{max} = 0.75$,

within 2.1%. Note that for all of the mass flux distortion studies in this paper, mass flux addition is calculated as,

$$\text{distortion}_1 + \text{distortion}_2 = \left[\frac{\rho u_{x1}}{(\rho u_{x1})_{clean}} - 1\right]_1 + \left[\frac{\rho u_{x1}}{(\rho u_{x1})_{clean}} - 1\right]_2 + 1. \qquad (5.1)$$

Linear scaling is also observed within the relative flow angle distribution at station 1, shown in Figure 5-13. A deviation from the low-speed results is observed in the rotor diffusion factor. Where Defoe and Hall found that the diffusion changes scaled with distortion intensity, this relationship does not hold true for a transonic compressor. A combination of distortions, $M_{min}/M_{max} = 0.50$ and $M_{min}/M_{max} = 0.75$, underpredicts the resultant diffusion of $M_{min}/M_{max} = 0.25$ in the rotor by 14.7% to 57.1%.

Figure 5-12: BLI distortion (90% span, 50% immersion) mass flux ratio compared to uniform inflow at station 1.

Figure 5-13: BLI distortion (90% span, 50% immersion) relative flow angle change from uniform inflow at station 1.
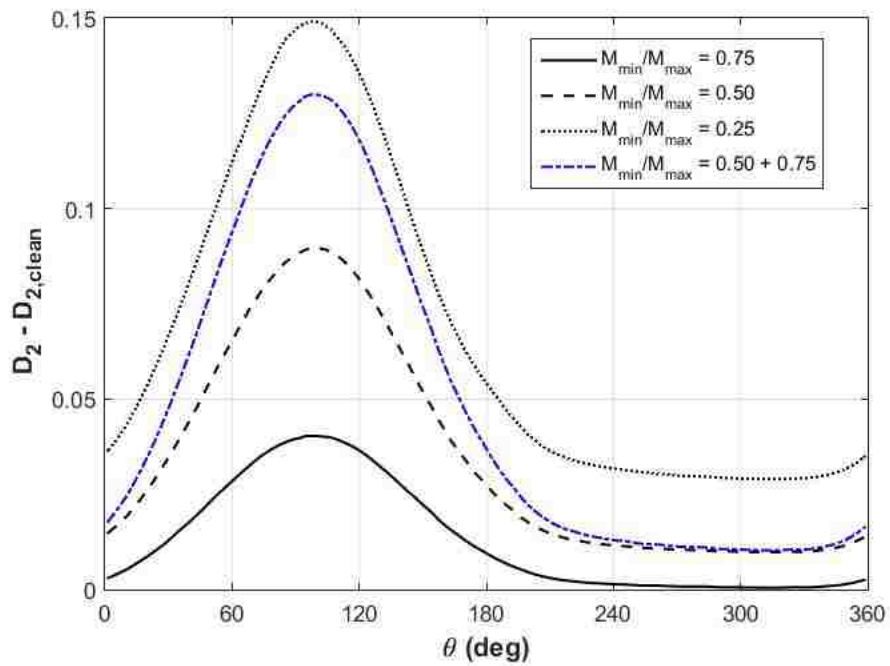
Figure 5-14: BLI distortion (90% span, 50% immersion) rotor diffusion factor changes from uniform inflow.

In immersion-varying distortions, no mass flux, relative flow angle or diffusion scaling is observed. An increase in distortion immersion has a diminishing effect on the resultant mass flux and flow angle changes, as seen in Figures 5-15 and 5-16, respectively. As expected, due to diffusion factor dependence on inlet relative flow angle, a non-linear rotor diffusion factor relationship exists, shown in Figure 5-17.
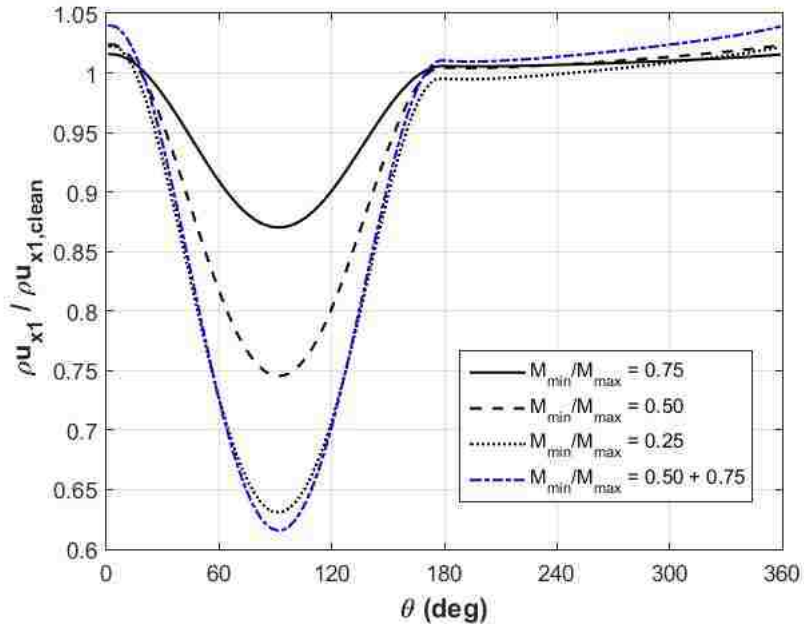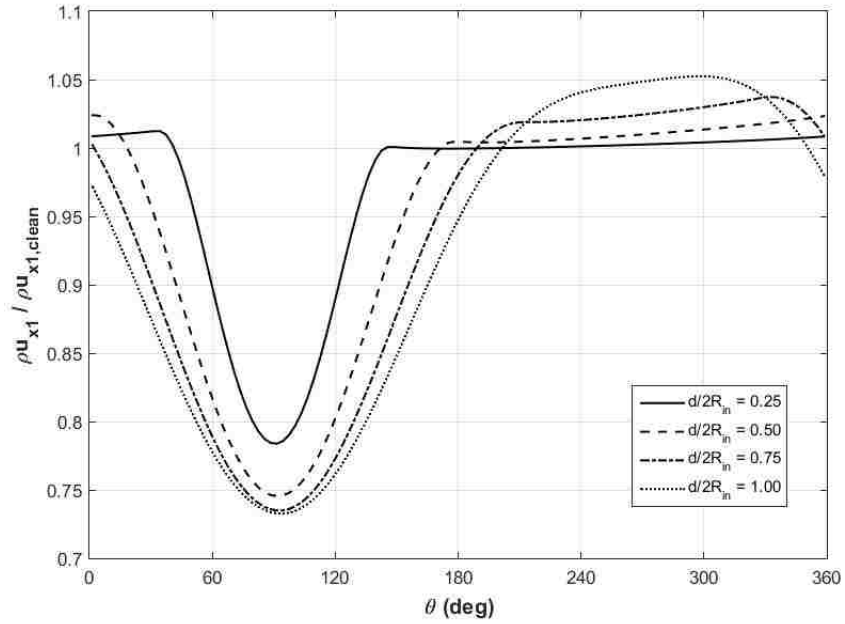

Figure 5-15: BLI distortion (90% span, 50% depth) mass flux ratio compared to uniform inflow at station 1.
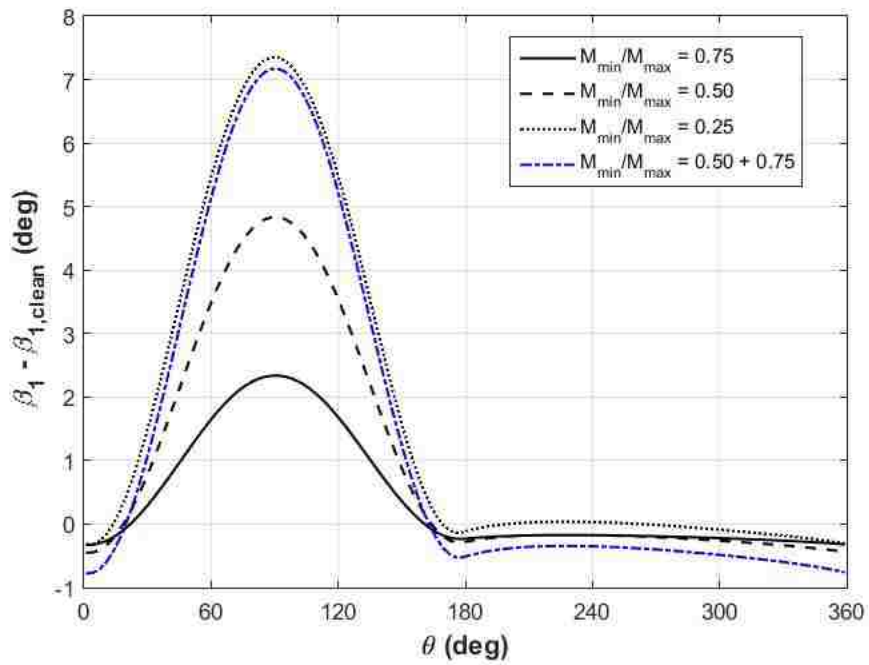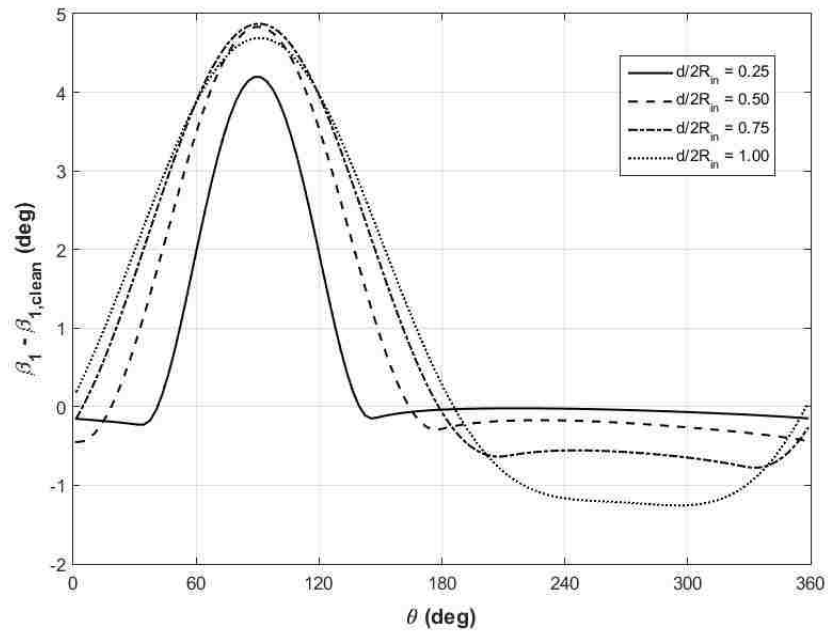
Figure 5-16: BLI distortion (90% span, 50% depth) relative flow angle change from uniform inflow at station 1.
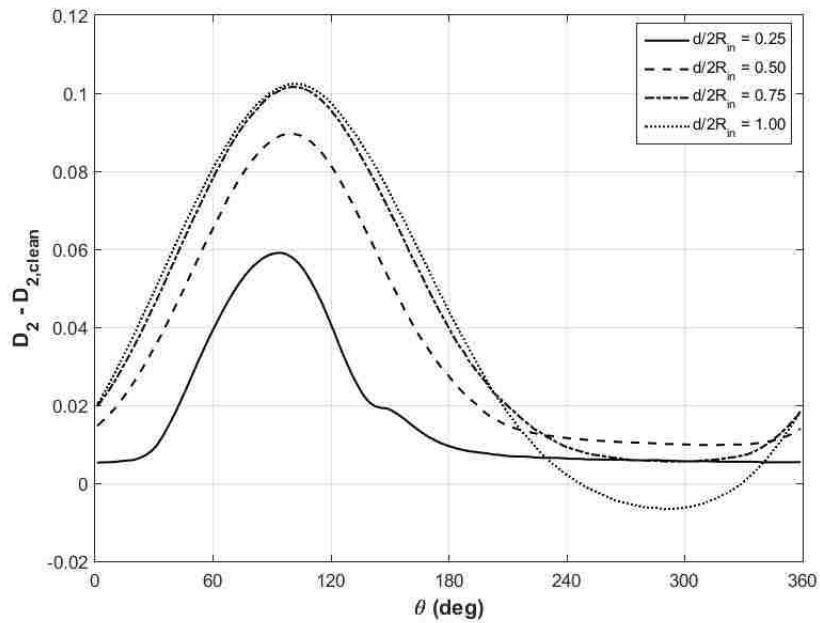
Figure 5-17: BLI distortion (90% span, 50% depth) rotor diffusion factor changes from uniform inflow.

5.3 Performance Scaling in Turboprop Radial Distortions

This section explores the various parameters of interest for a radial distortion profile: propeller offset, total temperature distortion, total pressure distortion, and a combined total temperature and pressure distortion.

5.3.1 Flow Redistribution Mechanisms in a Total Temperature Distortion

Relevant flow redistribution mechanisms in flow subjected to a total pressure distortion have been observed in previous literature [10, 11]. In these distortions, such as boundary layer ingestion, non-axisymmetric rotor work results from a non-uniform velocity field entering the compressor. The rotor performs more work on low momentum fluid, causing upstream static pressure distortion and mass flux redistribution towards the region of total pressure deficit. In a total temperature distortion, the opposite reaction is present. Upstream flow redistribution arises from changes in local density and axial velocity. Changes in local total density are inversely proportional to changes in total temperature, as observed from the ideal gas law,

$$p_t = \rho_t R T_t, \tag{5.2}$$

$$\rho_t = \frac{p_t}{R T_t}, \tag{5.3}$$

$$\rho_t \propto \frac{1}{T_t}. \tag{5.4}$$

Further, changes in axial velocity are proportional to the square root of total temperature changes. This is explained through the corrected flow equation,

$$\dot{m}_{corr} = \dot{m}\frac{\sqrt{T_t/T_{t,ref}}}{p_t/p_{t,ref}}, \tag{5.5}$$

where the mass flux per unit area is calculated as,

$$\frac{\dot{m}}{A} = \rho v_x. \tag{5.6}$$

To further simplify the corrected mass flow, the reference stagnation values are ignored, ideal gas law is implemented, and the gas constant is neglected. Additionally, neglecting changes in Mach number (which are small), changes in density scale with changes in total density,

$$\dot{m}_{corr} \propto \dot{m}\frac{\sqrt{T_t}}{\rho T_t}. \tag{5.7}$$

Finally, the corrected mass flow rate is held constant between test cases and can also be neglected. In addition, the mass flow rate can be expressed in terms of axial velocity and density, leaving the final relationship,

$$\frac{1}{\dot{m}} \propto \frac{\sqrt{T_t}}{\rho T_t}, \tag{5.8}$$

$$\frac{1}{\rho v_x} \propto \frac{1}{\rho\sqrt{T_t}}, \tag{5.9}$$

$$v_x \propto \sqrt{T_t}. \tag{5.10}$$

The above relationships dictate that regions of reduced total temperature have an associated reduction in axial velocity and increase in density. Due to a typical com-

pressor characteristic, regions of lower axial velocity, or lower fluid momentum have a higher relative blade loading, meaning the upstream flow is pulled harder into the compressor. This non-axisymmetric rotor work profile exaggerates the upstream inlet total temperature distortion instead of attenuating it. This observation is shown in Figure 5-18, a sample turboprop total temperature distortion with an axis offset of $\Delta R/R = 0.75$ at 50% span. In Figure 5-18(a), the mass flux distortion is increased at the compressor inlet compared to far upstream. This observation is supported by Figure 5-18(b) where the static pressure upstream, normalized by the local minimum value, has been reduced in the region of maximum total temperature distortion. The result of this flow redistribution is that counter-swirl is added to the flow in regions of high total temperature and co-swirl is added to the flow in regions of low total temperature. This effect is shown in 5-18(c), where the upstream rotor incidence angles are attenuated further downstream. The final result is that the flow mechanisms present in a total temperature distortion are opposite of a total pressure distortion; the rotor upstream influence increases the distortion, as observed in 5-18(d).
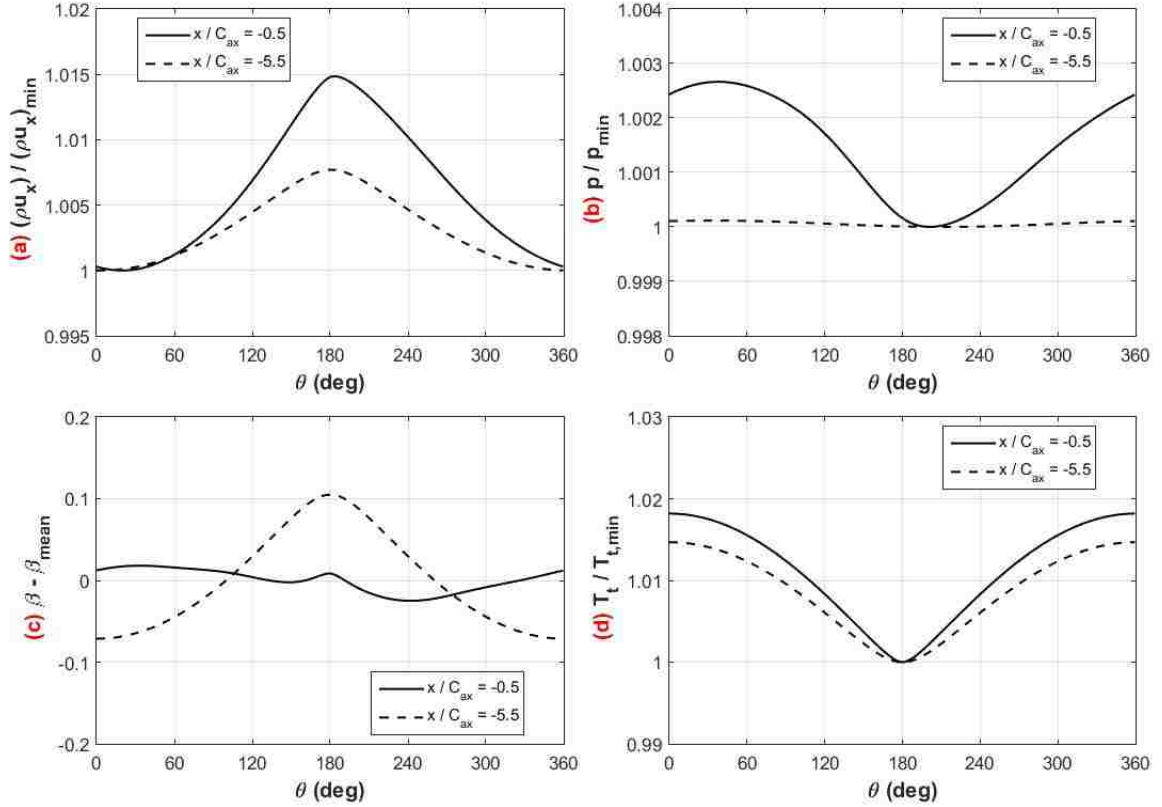
Figure 5-18: Total temperature radial distortion, plots (at 50% span) of (a) mass flux, (b) static pressure, (c) relative flow angle, and (d) total temperature at two locations upstream of the rotor leading edge.

5.3.2 Radial Distortion of Varying Propeller Offsets

To assess the upstream flow redistribution in the presence of radial offset distortions, the flow details at station 1 are observed at various propeller axis offset values. In this study, the total temperature ratio and total pressure ratio at station 0 are set to $T_{t0}/T_{t\infty} = 1.08$ and $p_{t0}/p_{t\infty} = 1.31$, respectively. Figures 5-19 and 5-20 show the change in mass flux and relative flow angle at station 1, respectively, compared to a uniform inflow case. The resultant ratio of rotor work to clean inflow rotor work is pictured in Figure 5-21. In the case of zero offset, upstream flow migrates radially towards the hub due to increased blade loading in the hub region. The mass flux, relative flow angle, and work profiles are radially variant, but circumferentially

invariant. At propeller offsets of of $\Delta R/R = 0.25$ and $\Delta R/R = 0.50$ the streamtube expansion near the distortion centre becomes apparent. Mass flux migrates towards the distortion centre, creating regions of co-swirl and counter-swirl near the hub. This leads to increased rotor work in the regions of co-swirl compared to the regions of counter-swirl. For this reason, mass flux is further redistributed towards the regions of co-swirl, causing the region of co-swirl to wrap around the spinner in the same direction as blade rotation. The magnitude of flow redistribution increases further at an offset distances of $\Delta R/R = 0.75$ and $\Delta R/R = 1.00$. Further increases in propeller axis offset have a diminishing effect on flow redistribution; propeller axis offsets larger than one compressor radius produce qualitatively similar inlet profiles.
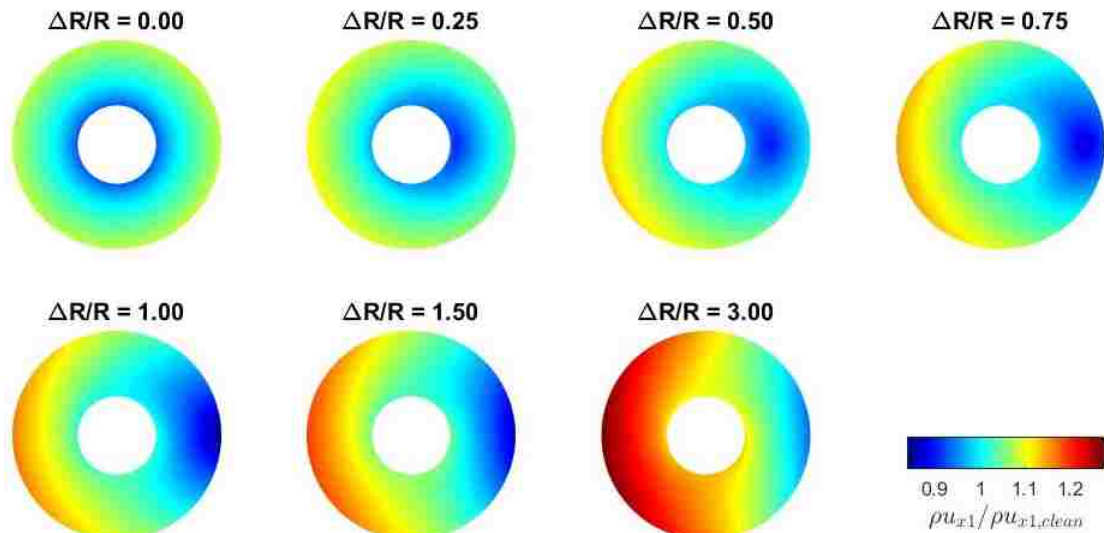
Figure 5-19: Mass flux ratio to clean inflow at station 1 for a radial distortion of various propeller offset distances.

99
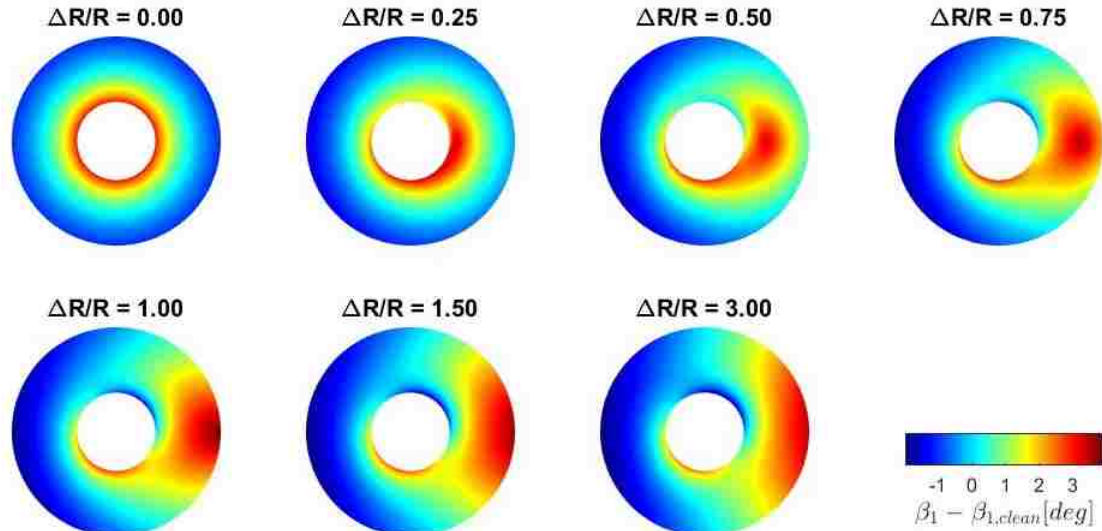
Figure 5-20: Change in rotor relative flow angle from clean inflow at station 1 for a radial distortion of various propeller offset distances.
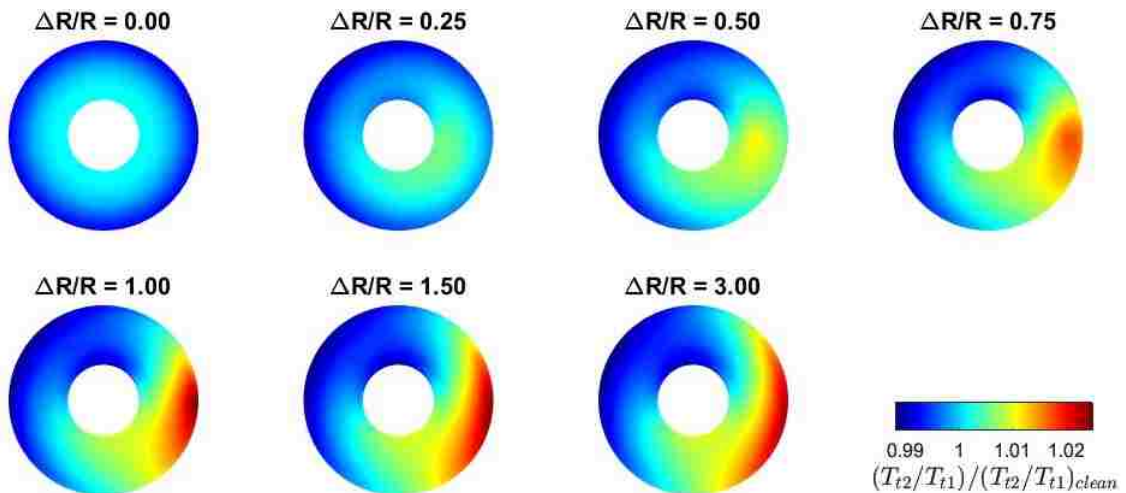
Figure 5-21: Rotor work ratio to clean inflow for a radial distortion of various propeller offset distances.

Circumferential plots at 90% span for a radial offset distortion, with offset values of $\Delta R/R = 0.50$, $\Delta R/R = 1.00$, and $\Delta R/R = 1.50$ are shown in Figures 5-22 to 5-24. Qualitatively, the mass flux and relative flow angle profiles are similar irrespective of the propeller offset. Mass flux migrates away from the propeller centre, causing streamtube contraction on the opposite side of the compressor inlet. The most severe mass flux deficit occurs at an offset equal to the compressor radius, $\Delta R/R = 1.00$;

further increases in propeller axis offset smooth the distortion profile. This smoothing is explained by examining the compressor inlet total pressure gradients, and the increased distortion radius of curvature at increased offsets. This effect is illustrated in Figure 5-25, a sketch of the total pressure at compressor inlet for two propeller offsets.
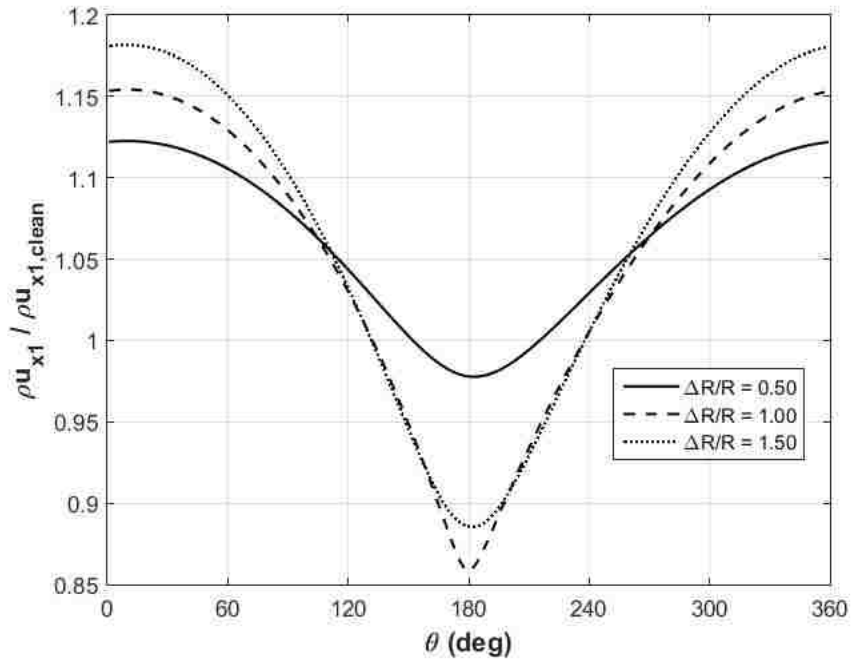
Figure 5-22: Radial offset distortion (90% span) mass flux ratio compared to uniform inflow at station 1.
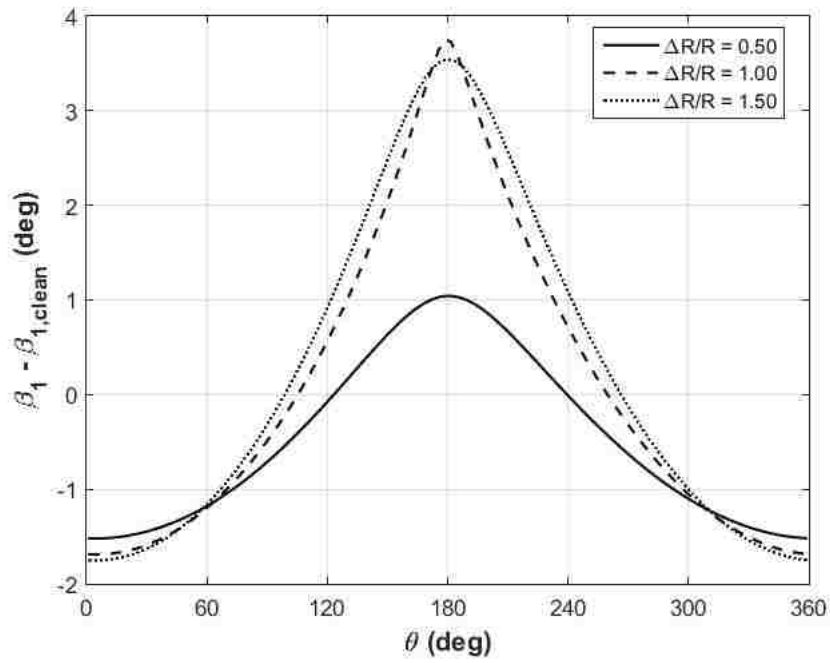
Figure 5-23: Radial offset distortion (90% span) relative flow angle change from uniform inflow at station 1.
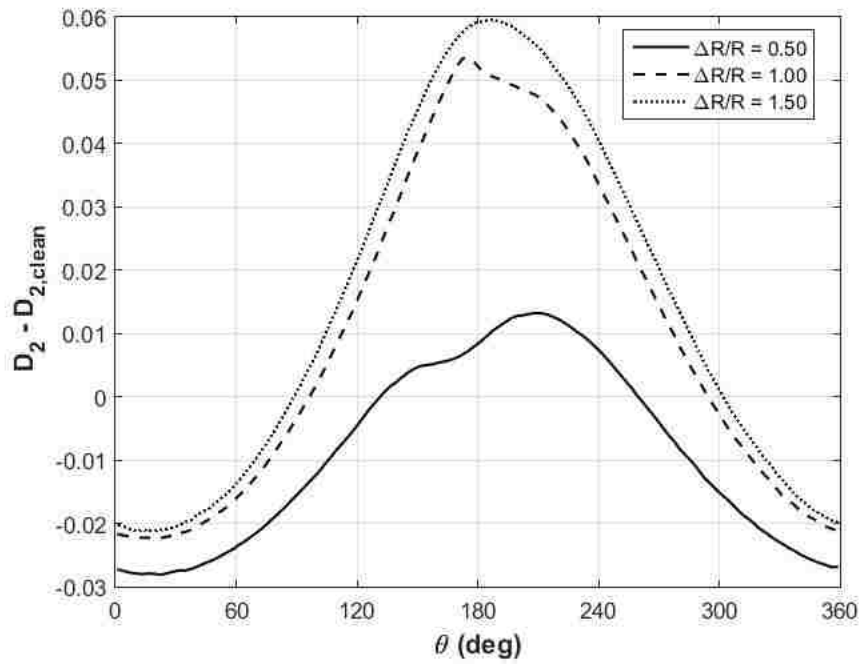
Figure 5-24: Radial offset distortion (90% span) rotor diffusion factor changes from uniform inflow.
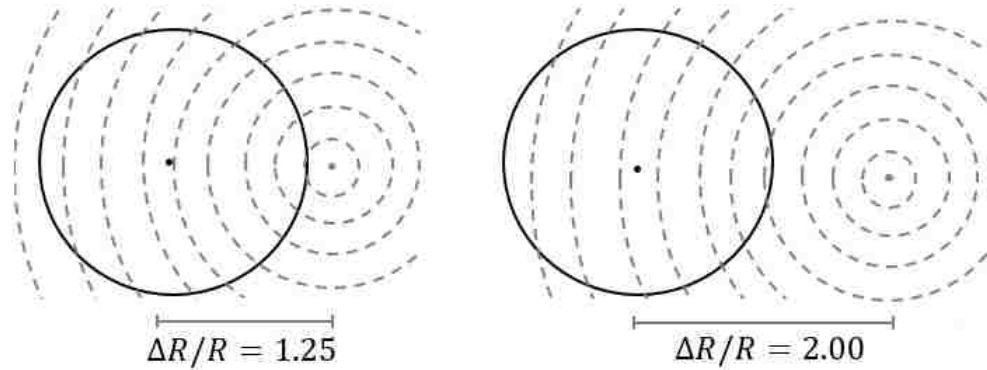
Figure 5-25: Radial distortion offset; compressor inlet total pressure distortion radius of curvature increases at offset locations further than one compressor inlet radius.

5.3.3 Radial Distortion of Varying Total Temperature Magnitude

At a propeller axis offset of $\Delta R/R = 0.75$, varying propeller outlet total temperature, and hence the compressor inlet total temperature, exhibits a linear scaling trend for all metrics observed. In Figure 5-26, the mass flux redistribution of a propeller tip total temperature ratio of 1.12 is predicted by the summation of propeller tip total temperature ratios of 1.04 and 1.12, by an error margin of 0.01% to 0.05%. The relative flow angle at station 1 and rotor diffusion factor changes, shown in Figures 5-27 and 5-28 also exhibit linear scaling trends. The rotor diffusion factor changes show low frequency oscillations. This due to the low magnitude of the changes from uniform case, where the maximum diffusion factor change is 0.45% from the uniform case. This is a result of the computational precision and not a physical phenomena.

Figure 5-26: Radial total temperature distortion (90% span, $\Delta R/R = 0.75$) mass flux ratio compared to uniform inflow at station 1.
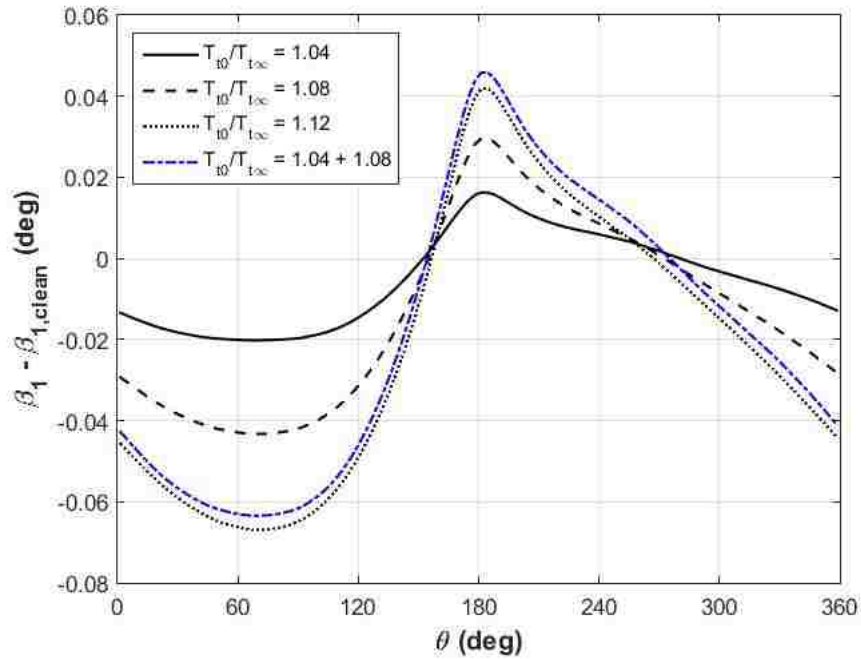
Figure 5-27: Radial total temperature distortion (90% span, $\Delta R/R = 0.75$) relative flow angle change from uniform inflow at station 1.
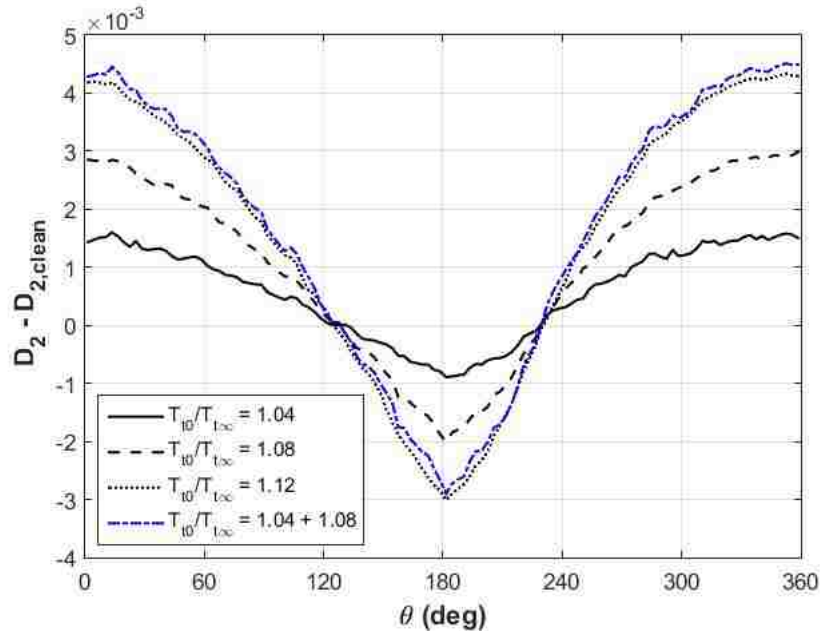
Figure 5-28: Radial total temperature distortion (90% span, $\Delta R/R = 0.75$) rotor diffusion factor changes from uniform inflow at station 2.

5.3.4   Radial Distortion of Varying Total Pressure Magnitude

In a radial total pressure distortion, a linear scaling relationship of mass flux and relative flow angle exists with distortion severity. This is shown in Figures 5-29 and 5-30, plots of the mass flux and relative flow angle at station 1 compared to the uniform inflow case. Compared to a mass flux distortion error of 2.1% in the BLI case, an error of 3.9% in present in the radial distortion. Also consistent with the BLI results shown in section 5.2, a non-linear scaling relationship of diffusion factor is observed in a total pressure distortion, shown in Figure 5-31.. This deviates from the observation made by Defoe and Hall [13] in a study of a low speed fan, as a total pressure distortion exhibited a linear scaling trend.
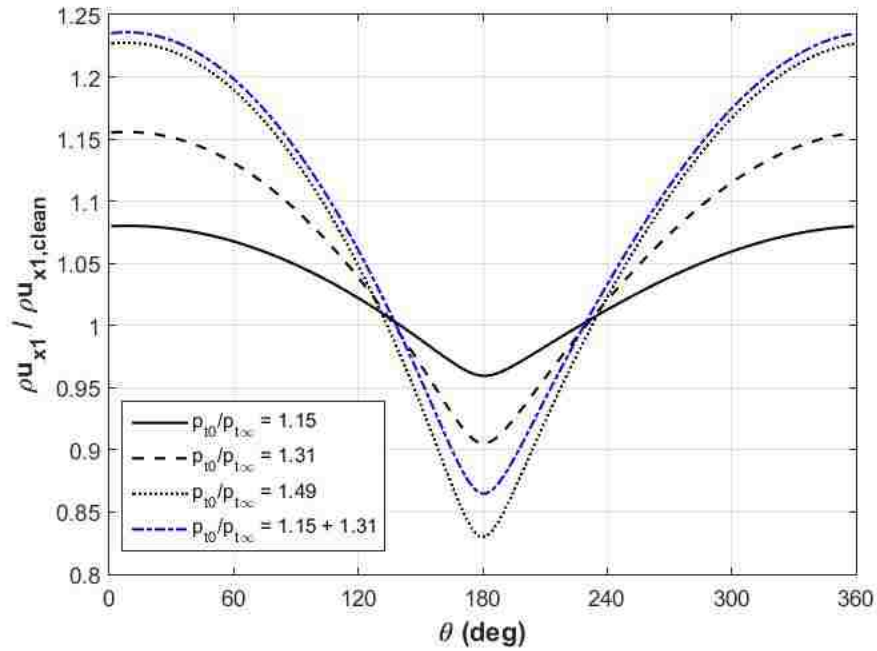
Figure 5-29: Radial total pressure distortion (90% span, $\Delta R/R = 0.75$) mass flux ratio compared to uniform inflow at station 1.
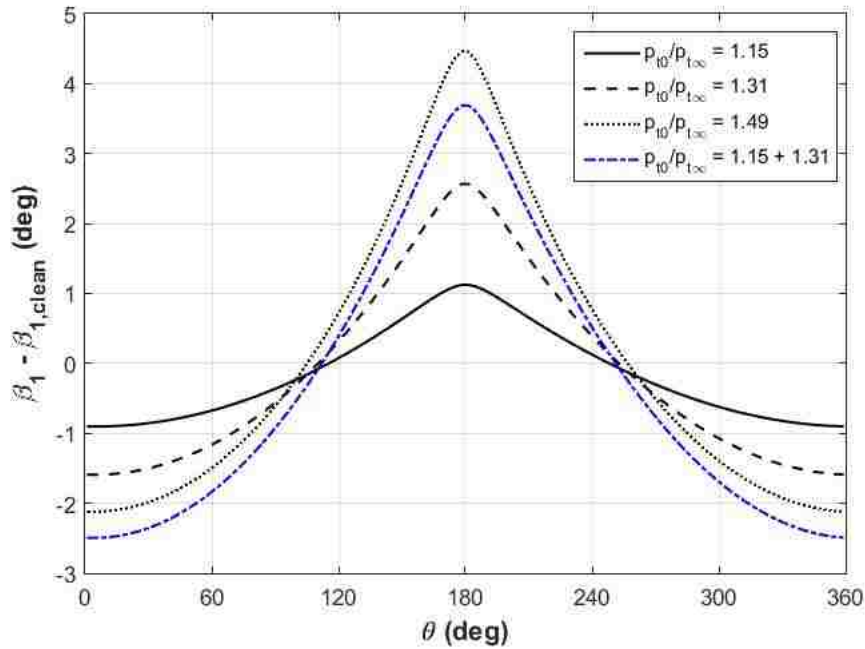
Figure 5-30: Radial total pressure distortion (90% span, $\Delta R/R = 0.75$) relative flow angle change from uniform inflow at station 1.

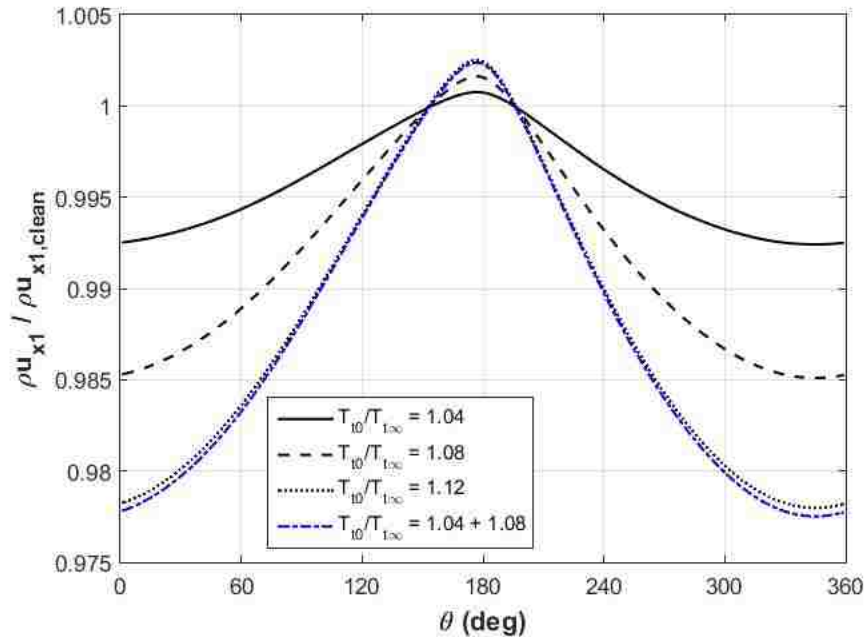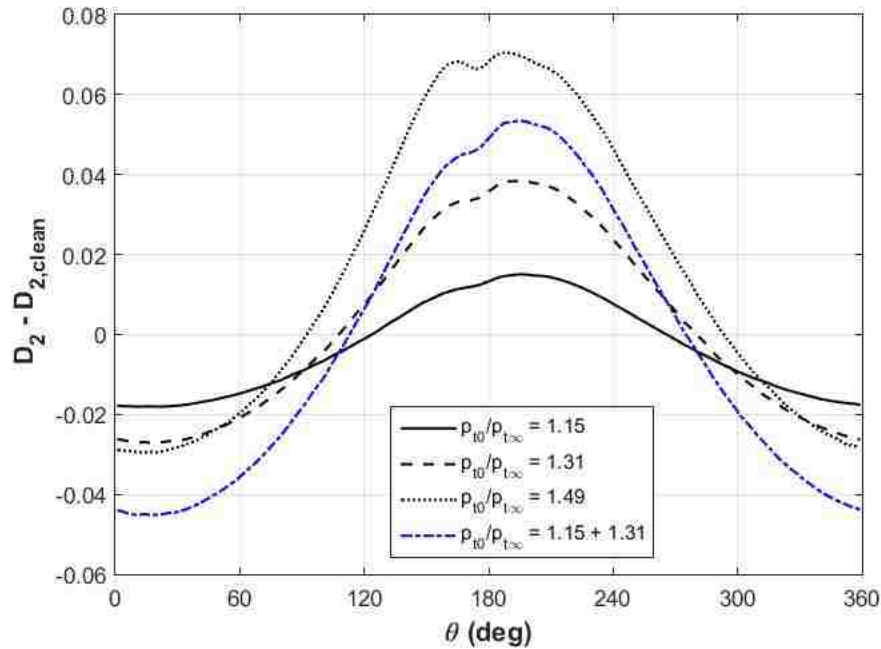Figure 5-31: Radial total pressure distortion (90% span, $\Delta R/R = 0.75$) rotor diffusion factor changes from uniform inflow.

In this thesis, the propeller work outlet is that of a perfectly efficient propeller and the total pressure is calculated from an isentropic compression. The magnitude of total pressure distortion compared to total temperature distortion is,

$$p_t = T_t^{\frac{(\gamma-1)}{\gamma}} . \tag{5.11}$$

For this reason, changes in diffusion factor and mass flux redistribution cannot be directly compared between the total temperature and total pressure distortion. A comparison is made by scaling the diffusion factor changes by a factor of $\Delta D^{\frac{(\gamma-1)}{\gamma}}$. Additionally, total temperature and total pressure distortions exhibit opposite mass flux redistribution trends as discussed earlier. In addition to the magnitude scaling, the results must also be phase shifted by $180^{\underline{o}}$. The resultant comparison of diffusion factor changes is shown in Figure 5-32. The total pressure distortion creates diffusion factor changes more significant than the total temperature distortion, ranging from

165% at $\theta = 0^{\circ}$ to 457% at $\theta = 180^{\circ}$. This phenomena can be explained by the nature of the two individual distortions. A total pressure distortion incorporates a velocity distortion, however, a total temperature distortion incorporates both a velocity and density distortion. The velocity and density distortions have opposite effects on diffusion factor changes, thus reducing the magnitude of diffusion factor changes compared to a total pressure distortion.
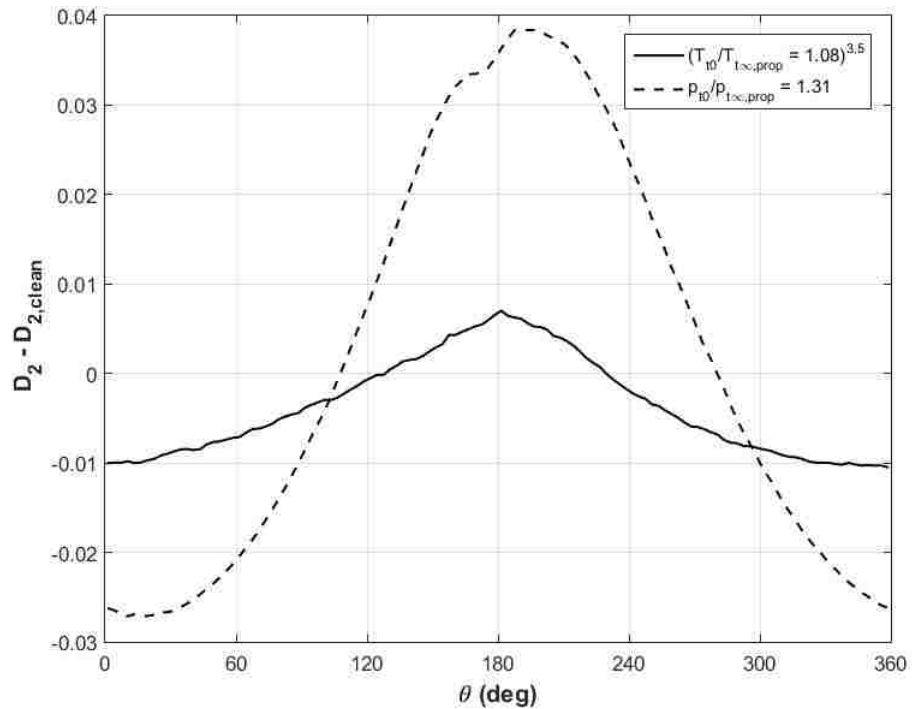
Figure 5-32: Comparison of total pressure and scaled total temperature distortion diffusion factor changes at 90% span.

5.3.5 Combined Total Temperature and Total Pressure Radial Distortion

In the presence of a combined total temperature and total pressure distortion at a propeller axis offset of $\Delta R/R = 0.75$, a non-linear diffusion factor relationship between distortion severities exits. This is expected based on the results from the

previous subsection. However, a summation of the individual total temperature and total pressure distortion is able to quantitatively predict the upstream mass flux redistribution and relative flow angles, shown in Figures 5-33 and 5-34. As expected by matching upstream conditions, the diffusion factor results are also represented by a summation of the individual distortions, as shown in Figure 5-35, to within 3.65%.
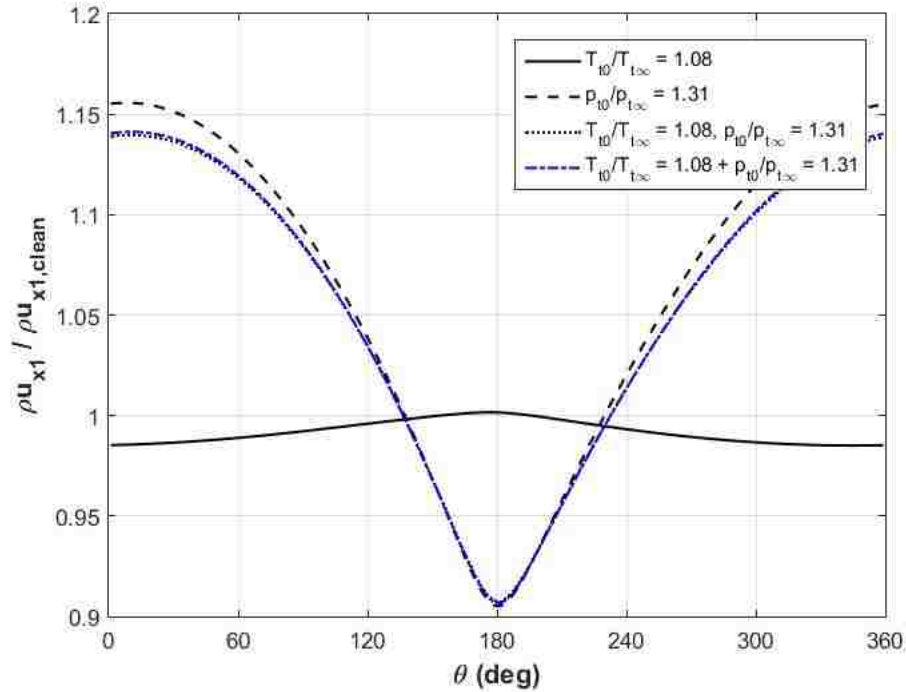
Figure 5-33: Radial combined total temperature and total pressure distortion (90% span, $\Delta R/R = 0.75$) mass flux changes from uniform inflow.

In this chapter, important generalized findings as well as machine specific findings were observed. First, the mechanisms for upstream flow redistribution in a total temperature distortions were identified. Regions of high total temperature have an associated reduction in density, increase in axial velocity and thus reduced blade loading compared to regions of low total temperature. These mechanisms result in a rotor upstream influence that works to exaggerate the inlet total temperature distortion, the opposite mechanism of a total pressure distortion. For NASA r67, non-linear diffusion factor scaling was observed for all total pressure distortions, despite

linear scaling of upstream flow redistribution; a result different from the results of a low-speed fan case. In a total temperature distortion, linear scaling of both upstream effects and rotor diffusion factor were observed. Finally, the effects of a combined total temperature and total pressure distortion were well predicted by the addition of the individual distortions.
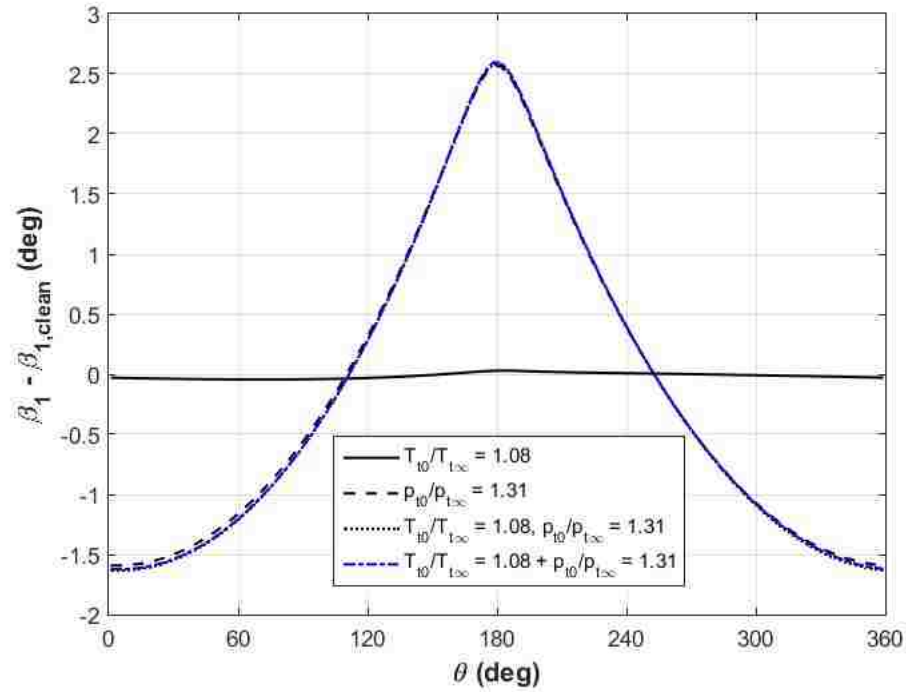
Figure 5-34: Radial combined total temperature and total pressure distortion (90% span, $\Delta R/R = 0.75$) relative flow angle changes from uniform inflow.
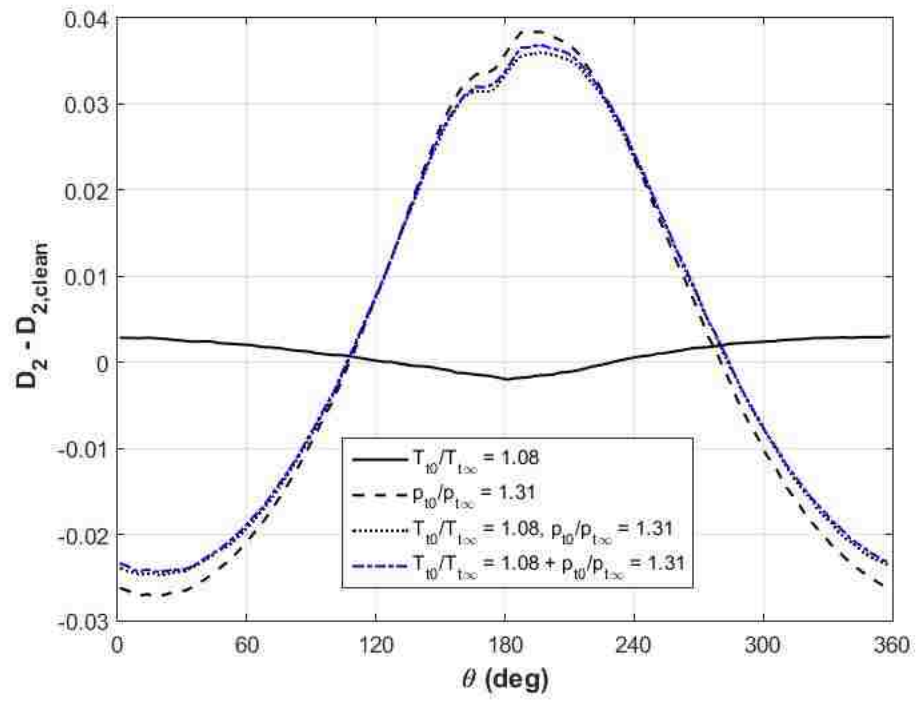
Figure 5-35: Radial combined total temperature and total pressure distortion (90% span, $\Delta R/R = 0.75$) rotor diffusion factor changes from uniform inflow.

Chapter 6

Conclusions and Future Work

In this thesis, a volumetric source term model is used to assess the performance of a single stage compressor across a parametric study of non-uniform inflow distortions. In this chapter, a summary of the work performed is outlined, the key outcomes of the study are presented, and recommendations for future work are discussed.

6.1   Summary

Several previous authors have studied the flow mechanisms present in a BLI compressor or fan. A study on the scaling of both BLI and turboprop inlet distortions has been performed on a low-speed fan, however, no such study has been performed on a transonic compressor. This limitation in previous research is the motivation behind the work in this thesis. Due to the extensive computational requirement of a full annulus URANS calculation, a volumetric source term model of the NASA stage67 machine was developed.

In Chapter 3, the methodology behind the development of this volumetric source term model is discussed. To develop both the normal and parallel force models, a single passage RANS calculation is first carried out. The results of this study are assessed versus previously published experimental and CFD results. The normal

force model is an adaptation of a previously developed low-speed blade loading model based on thin airfoil theory. Using the extracted flow angles from the single passage RANS results, a compressibility correction constant is found to allow the low-speed model to be used on a transonic fan. For the parallel force, a double-sided loss bucket is developed to create a more robust efficiency characteristic, again by comparison against the single passage results. Finally, the distortion matrix of interest in this thesis is established.

The resultant volumetric source term model is assessed in both uniform inflow and non-uniform inflow conditions in Chapter 4. For a uniform inflow, the model is assessed against the single passage RANS results. To determine the accuracy of the model in non-uniform inflow, the VSTM is compared against previously published experimental and CFD results, with a 120° total pressure distortion. Upstream flow redistribution and downstream circumferential and spanwise flow profiles are observed, however flow characteristics within the blade domain are not examined.

In Chapter 5 a key limitation in the VSTM parallel force is examined. A flaw in the formulation of off design loss characteristics is revealed, which limits the extent to which the distortion matrix can be studied. Rather than each streamtube being dependent on the local deviation from design flow coefficient, a mass averaged parameter across the entire blade inlet is used, meaning that the flow response to non-uniform inflow is incorrect. The remainder of the chapter observes the upstream flow redistribution and rotor diffusion factor in both BLI and turboprop distortions. These parameters are unaffected by the loss force limitation.

6.2   Key Outcomes and Conclusions

From the results obtained in this thesis, key outcomes and conclusions are drawn regarding two facets of the work: development of the VSTM itself and the transonic

compressor response to an array of non-uniform inflow distortions.

The VSTM in this work is successful in significantly reducing the computational resources required to study a matrix of distortions. This is achieved through two separate advantages, a full annulus grid count reduction of 95.3% and the use of a steady calculation. Previously published results using unsteady RANS calculations have indicated the need for 30 rotor revolutions to obtain a converged solution [11], meaning the use of a steady calculation is the main advantage of the VSTM. Within the VSTM, innovations were made to both the normal and parallel force models. More specifically, a normal force compressibility correction constant and a parallel force double-sided loss model (above and below peak efficiency) were implemented. Using this model, with uniform inflow, the rotor FPR, isentropic efficiency, and entropy-based loss coefficient are predicted within 1.43%, 0.03%, and 3.37% of single passage RANS results, respectively. The VSTM is also assessed against previously published experimental and CFD results on a 120° total pressure distortion. The VSTM is able to qualitatively capture the upstream flow redistribution, as well as rotor and stator TE total temperature, total pressure, and relative flow angles. Due to the uncertainty in inlet boundary conditions, distortion conditions are not able to be perfectly replicated. Despite this, the rotor total pressure ratio is perfectly matched by the VSTM, and the rotor isentropic efficiency change is correct to within 2.7%.

By subjecting the VSTM to non-uniform inflow, the entropy-based loss coefficient was shown qualitatively to match the mass flux redistribution profile, an inconsistency with typical compressors. This is the result of a shortcoming within the parallel force model. Using $\overline{M}_{rel}^{M}$ as an off-design loss coefficient scaling parameter does allow local deviations in flow coefficient to be captured, rather a single value is applied to the entire blade domain inlet. Therefore, local loss forces are highly dependent on local relative velocity, explaining the relationship between mass flux and loss coefficient. For this reason, only three key parameters, each of which are weakly dependent of the

blade domain loss value, are studied: mass flux ratio, change in relative flow angle, and rotor diffusion factor, all compared against uniform inflow conditions.

For a BLI total pressure distortion of varying depth, a linear scaling trend for mass flux redistribution and relative flow angle was observed. A distortion of $M_{min}/M_{max} = 0.25$ is predicted by the addition of distortions of $M_{min}/M_{max} = 0.50$ and $M_{min}/M_{max} = 0.75$, within 2.1%. This result is consistent with that observed on a low-speed fan. A difference from the low-speed fan is observed in studying the rotor diffusion factor, where the error between the same two conditions ranges from 14.7% to 57.1%. No scaling between cases was observed for immersion-varying BLI distortions, increasing the distortion immersion has a diminished effect on diffusion factor. This effect is attributed to the compressibility effects of the transonic compressor.

Mechanisms for flow redistribution were observed in a total temperature distortion. Relative increases in total temperature create an associated local reduction in density and increase in axial velocity. Due to this, non-axisymmetric rotor work is performed and the compressor pulls harder on the undistorted flow, working to exaggerate the total temperature distortion. This upstream flow redistribution is the opposite of a total pressure distortion of the same pattern.

In the case of varying propeller axis offset, no scaling parameter was observed. Due to the change in distortion pattern at varying axis offsets, this result is expected. The maximum change in rotor diffusion factor was observed at a propeller axis offset of $\Delta R/R = 1.00$; increases in axis offset beyond this point smoothed diffusion factor changes. This effect is due to increased radius of curvature of the compressor inlet distortion as the propeller is moved further off-axis. Radial total temperature distortions were observed at an axis offset of $\Delta R/R = 0.75$, for which a linear scaling trend was observed for mass flux redistribution, rotor inlet relative flow angle, and rotor diffusion factor, with a maximum error of 0.05%. For a radial total pressure distortion, similar results to the BLI distortion were found; a linear scaling between

distortion severity was observed for mass flux redistribution and relative flow angle, to 3.9%, but not for rotor diffusion factor. Comparing the effects of radial total pressure versus radial total temperature distortions, a total pressure distortion was found to have a significantly larger impact on the rotor diffusion factor, by up to 457%. Lastly, the effect of the individual total temperature and total pressure distortions was shown to capture the combined distortion diffusion factor to within 3.65%.

6.3   Current Outlook and Future Recommendations

This section contains work that is currently in progress that will serve to complement this work, as well as a recommendation for future work based on the discoveries in this thesis.

At the time of this thesis publication, work is being performed on creating an optimized, automated approach to determining the loss force coefficients. Through the use of analytical optimization methods, a significant reduction in the computational time to develop these coefficients will be achieved, in combination with an increased accuracy when compared to experimental results. Additionally, and based on the distortion matrix tested in this paper, work is being done by Defoe and Hall [13] to test non-dimensionally similar radial distortions on a low-speed fan. Doing so will allow a more extensive comparison between the two machines. Finally, work is being done to establish the use of a mass-source model to eliminate the need for blade recambering.

It is also recommended that a further modification to the parallel force model could be made, and the test matrix in this work re-studied. The limitation of the volumetric source term model in this work is that it is unable to correctly capture off-design local blade performance in the presence of non-uniform inflow. A modified parallel force description could be developed to trace individual streamlines through a blade domain. This approach would allow for the local deviation in flow coefficient

to be captured and thus the local entropy-based loss coefficient and overall rotor isentropic efficiency could be captured. Given that the parameters for the distortion matrix are established, the normal force model for the machine is already developed, and the reduced computational cost of a VSTM, this study could be replicated in a significantly shorter time frame.

Bibliography

[1] Plas, A., Crichton, D., Sargeant, M., et al. Performance of a boundary layer ingesting (bli) propulsion system. In *45th AIAA aerospace sciences meeting and exhibit*, page 450, 2007.

[2] Bonaccorsi, A., Giuri, P. When shakeout doesn't occur: the evolution of the turboprop engine industry. *Research Policy*, 29(7):847–870, 2000.

[3] Smith, A.M., Roberts, H.E. The jet airplane utilizing boundary layer air for propulsion. *Journal of the Aeronautical Sciences*, 14(2):97–109, 1947.

[4] Spakovsky, Z. *Trends in Thermal and Propulsive Efficiency*, chapter Thermodynamics and Propulsion. MIT, 2002.

[5] Federal Aviation Administration. *Pilot's Handbook of Aeronautical Knowledge*. Skyhorse Publishing, faa-h-8083-25a edition, 2014.

[6] Douglass, W.M. Propulsive efficiency with boundary layer ingestion. *Mc-Donnell Douglas, Tech. Rep*, 1600:J0860, 1970.

[7] Smith, L.H. Wake ingestion propulsion benefit. *Journal of Propulsion and Power*, 9(1):74–82, 1993.

[8] Sargeant, M.A. *Boundary layer ingestion for advanced airframes*. PhD thesis, University of Cambridge, 2008.

[9] Hynes, T., Madani, V. et al. Boundary layer ingesting intakes: Design and optimization. *International Symposium on Air Breathing Engines*, 2009.

[10] Gunn, E. J., Hall, C. A. Aerodynamics of Boundary Layer Ingesting Fans. *ASME Turbo Expo 2014: Turbine Technical Conference and Exposition. American Society of Mechanical Engineers*, 2014.

[11] Fidalgo, V.J., Hall, C.A., Colin, Y. A study of fan-distortion interaction within the nasa rotor 67 transonic stage. *Journal of Turbomachinery*, 134(5):051011, 2012.

[12] Anderson, B.H., Baust, H.D., Agrell, J. Management of total pressure recovery, distortion and high cycle fatigue in compact air vehicle inlets. Technical report, NASA, 2002.

[13] Defoe, J.J., Hall, D.K. Fan performance scaling with inlet distortions. In *ASME Turbo Expo 2016: Turbomachinery Technical Conference and Exposition*, pages V02AT37A052–V02AT37A052. American Society of Mechanical Engineers, 2016.

[14] Lieblein, S., Schwenk, F., Broderick, R. Diffusion factor for estimating losses and limiting blade loadings in axial-flow compressor blade elements. Technical report, National Advisory Committee for Aeronautics, 1953.

[15] Peters, A. *Ultra-Short Nacelles for Low Fan Pressure Ratio Propulsors*. Ph.D Thesis, MIT, Department of Aeronautics and Astronautics, February 2014.

[16] Brand, M. L. *An Improved Blade Passage Model for Estimating Off-Design Axial Compressor Performance*. MS Thesis, MIT, Department of Aeronautics and Astronautics, September 2013.

[17] Gong, Y., Tan, C.S., Gordon, K.A., Greitzer, E.M. A computational model for short wavelength stall inception and development in multi-stage compressors. In

ASME 1998 International Gas Turbine and Aeroengine Congress and Exhibition, pages V001T01A114–V001T01A114. American Society of Mechanical Engineers, 1998.

[18] Hall, D.K., Greitzer, E.M., Tan, C.S. Analysis of fan stage design attributes for boundary layer ingestion. In *ASME Turbo Expo 2016: Turbomachinery Technical Conference and Exposition*, pages V02AT37A047–V02AT37A047. American Society of Mechanical Engineers, 2016.

[19] Marble, F. Three-dimensional flow in turbomachines. *High Speed Aerodynamics and Jet Propulsion*, 10:83–166, 1964.

[20] Miller, R.J. Loss mechanisms in turbomachines. In *Cambridge Turbomachinery Course 2012*. Cambridge University, 2012.

[21] Greitzer, E.M., Tan, C.S., Graf M.B. *Internal Flows: Concepts and Applications*. Cambridge University Press, 2004.

[22] Strazisar, A.J., Wood, J.R., Hathaway, M.D., Suder, K.L. Laser anemometer measurements in a transonic axial-flow fan rotor. Technical report, NASA, 1989.

[23] Vahdati, M., Sayma, A., Freeman, C., Imregun, M. On the use of atmospheric boundary conditions for axial-flow compressor stall simulations. *Journal of turbomachinery*, 127(2):349–351, 2005.

[24] Autodesk, Novi, MI. *AutoCAD User's Guide*, 20.0 edition, 2014.

[25] Pointwise, Forth Worth, TX. *Pointwise User's Manual, V18*, 18.0r2 edition, 2016.

[26] ANSYS, Inc., Canonsburg, PA. *ANSYS TurboGrid User's Guide*, release 15.0 edition, November 2013.

[27] ANSYS, Inc., Canonsburg, PA. *ANSYS CFX Solver Theory Guide*, release 15.0 edition, November 2013.

[28] MathWorks, Inc., Natick, MA. *MathWorks MATLAB Documentation*, 2014b edition, 2014.

[29] Menter, F.R. Zonal two-equation k-omega turbulence model for aerodynamic flows. *AIAA Paper*, 93(2906), 1993.

[30] SHARCNET. All Systems. Online. Accessed on March 1, 2017 at `https://www.sharcnet.ca/my/systems`.

[31] Patel, K., Novak, C., Defoe, J.J. A novel numerical approach for generation and propagation of rotor-stator interaction noise. In *22nd AIAA/CEAS Aeroacoustics Conference*, page 2821, 2016.

[32] Pratt & Whitney Canada. PW100/PW150. Online. Accessed on January 19, 2017 at `http://www.pwc.ca/en/engines/pw100-pw150`.

Appendix A

Volumetric Source Term Model

CFX Expressions

```
AngularCoordinate = atan2(z,(−y))
AngularVelocity = Velocity v * sin(AngularCoordinate) + Velocity w * cos
    (AngularCoordinate)
BladeMetalAngle = BladeAngle(x,Radiusx,0[m])
BladeMetalAngleDeg = BladeMetalAngle * 180 [deg] / pi [rad]
DeviationFromDesiredRotor = (FlowAngleRotor − FlowAngleRotorDesired) *
    180 [deg] / pi [rad]
DeviationFromDesiredStator = (FlowAngleStatorDesired − FlowAngleStator)
    * 180 [deg] / pi [rad]
DeviationRotor = (FlowAngleRotor − BladeMetalAngle)
DeviationRotorDeg = DeviationRotor * 180 [deg] / pi [rad]
DeviationStator = (BladeMetalAngle − FlowAngleStator)
DeviationStatorDeg = DeviationStator * 180 [deg] / pi [rad]
EnergyR = (FthetaR+FthetaRp)*Radiusx*RotationSpeed
FRotor = sin(FlowAngleRotor − BladeMetalAngle + offsetrotor − decamber)
    * (rvelo^2) / h * constant
FStator = sin(BladeMetalAngle − FlowAngleStator − offsetstator) * (svelo
    ^2) / h * constant
FlowAngleRotor = atan2((AngularVelocity + Radiusx*RotationSpeed),
    Velocity u)
FlowAngleRotorDeg = FlowAngleRotor *180[deg] / pi[rad]
FlowAngleRotorDesired = FlowAngle(x,Radiusx,0[m])
FlowAngleStator = atan2(AngularVelocity,Velocity u)
FlowAngleStatorDeg = FlowAngleStator *180[deg] / pi[rad]
FlowAngleStatorDesired = FlowAngle(x,Radiusx,0[m])
FpRotor = if(rMachRel > rMachRef2,Kp1Rotor / h * (rMachRel^2 + Kp2Rotor
    *(rMachRel−rMachRef)^2) *...
                        (rvelo^2)*(1+(rMachRef2−rMachRel)^2* Kp3Rotor) *
                            Density,Kp1Rotor / h * (rMachRel^2 +...
                    Kp2Rotor*(rMachRel−rMachRef)^2)* (rvelo^2) * Density)
```

```
FpStator = Kp1Stator / h * (sMachRel^2 + Kp2Stator*(sMachRel−sMachRef)
    ^2)* (svelo^2) * Density
FrRp = −1 * FpRotor * RadialVelocity/rvelo
FrSp = −1 * FpStator * RadialVelocity/svelo
FthetaR = Density*FRotor*cos(FlowAngleRotor)
FthetaRp = FpRotor * (AngularVelocity + Radiusx*RotationSpeed) / rvelo
FthetaS = −1*Density*FStator*cos(FlowAngleStator)
FthetaSp = FpStator * AngularVelocity / svelo
FxR = Density*FRotor*sin(FlowAngleRotor)
FxRp = −1 * FpRotor * Velocity u / rvelo
FxS = −1*Density*FStator*sin(FlowAngleStator)
FxSp = −1 * FpStator * Velocity u / svelo
Kp1Rotor = 0.0145
Kp1Stator = 0.052
Kp2Rotor = 650
Kp2Stator = 5
Kp3Rotor = 1125
RadialVelocity = −1*Velocity v * cos(AngularCoordinate) + Velocity w *
    sin(AngularCoordinate)
Radiusx = sqrt(y^2 + z^2)
RotationScaling = 0.9
RotationSpeed = RotationScaling * 1680.02[s−1 rad]
anglechange = AngleChangeFunction(Radiusx)
constant = pi * sqrt(solidity)
decamber = 0.27 * (x−rotormin)/(rotormax−rotormin) * −anglechange * pi[
    rad]/180[deg]
h = hFunction(x,Radiusx,0[m])
offsetrotor = OffsetRotorFunction(x,Radiusx,0[m])
offsetstator = OffsetStatorFunction(x,Radiusx,0[m])
rMachRef = 1.0007
rMachRef2 = 0.987
rMachRel = massFlowAve(rvelovar)@REGION:RotorInlet B / ...
                    massFlowAve(Local Speed of Sound)@REGION:RotorInlet
rotormax = RotorMaxFunction(Radiusx)
rotormin = RotorMinFunction(Radiusx)
rvelo = sqrt(Velocity u ^2 + (AngularVelocity+Radiusx*RotationSpeed) ^2
    + RadialVelocity^2)
sMachRef = 0.61996
sMachRel = massFlowAve(Mach Number)@REGION:StatorInlet
solidity = SolidityFunction(x,Radiusx,0[m])
svelo = sqrt(Velocity u ^2 + AngularVelocity ^2 + RadialVelocity^2)
```

Vita Auctoris

Name: David Jarrod Hill

Place of Birth: Snellville, Georgia, USA

Year of Birth: 1991

Education: M.A.Sc, Mechanical Engineering

                                    University of Windsor, 2015-2017

                                    B.Eng, Aerospace Engineering

                                    Carleton University, 2009-2013